Optimisation based parameter identification using optical field measurements

von der Fakultät Maschinenbau
der Technischen Universität Dortmund
zur Erlangung des akademischen Grades

Doktor-Ingenieur (Dr.-Ing.)

genehmigte Dissertation

von

Lars Rose

aus Haan

Referent:	Prof. Dr.-Ing. A. Menzel
Korreferenten:	Prof. Dr.-Ing. S. Diebels
	Prof. Dr. U. A. Handge
Tag der Einreichung:	27.10.2021
Tag der mündlichen Prüfung:	11.02.2022

Bibliografische Information Der Deutschen Bibliothek
Die Deutsche Bibliothek verzeichnet diese Publikation in der Deutschen Nationalbibliografie; detaillierte bibliografische Daten sind im Internet über **http://dnb.ddb.de** abrufbar.

Bibliographic information published by Die Deutsche Bibliothek
Die Deutsche Bibliothek lists this publication in the Deutsche Nationalbibliografie; detailed bibliographic data is available in the Internet at **http://dnb.ddb.de**.

Schriftenreihe des Instituts für Mechanik

Herausgeber: Institut für Mechanik
Fakultät Maschinenbau
Technische Universität Dortmund
Leonhard-Euler-Str. 5
D-44227 Dortmund

Druck: Koffler DruckManagement GmbH

Als Manuskript gedruckt. Printed in Germany.

ISSN 2191-0022
ISBN 978-3-947323-31-9

Zusammenfassung

Ein Rahmen für Parameteridentifikationen von vollständig thermo-mechanisch gekoppelten, konstitutiven Modellen wird vorgestellt, welcher das Einbinden von Experimentaldaten aus vollflächigen Digital-Image-Correlation- (DIC) und Thermographie-Aufnahmen erlaubt. Die Theorie des inversen Problems der Parameteridentifikation wird ausführlich erläutert, wobei der Fokus auf der algorithmischen Behandlung der intrinsisch unterschiedlichen Daten von Verschiebung (Lagrange Typ) und Temperatur (Euler Typ), der Definition einer Zielfunktion welche Starrkörperbewegungen kompensiert und auf der notwendigen Analyse der erzielten Ergebnisse liegt. Der letzte Aspekt beinhaltet dabei insbesondere Theorie bezüglich Identifizierbarkeit, Modellabhängigkeit, Verifizier- und Validierbarkeit. Des Weiteren wird die allgemeine Anwendbarkeit des vorgeschlagenen Rahmens anhand eines einfachen Zugversuches mit einer Aluminium-Legierung empirisch gezeigt. Genauer gesagt werden Daten von zwei unterschiedlichen Arten von Experimenten genutzt, einmal mit einer Abkühlphase auf Grund der Umgebungstemperatur und einmal ohne. Auf Grundlage des beobachteten Materialverhaltens werden zwei thermo-mechanisch gekoppelte konstitutive Modelle ausgewählt, die konstitutiven Gleichungen zusammengefasst und die Modellparameter interpretiert. Die Identifizierbarkeit der thermischen Modellparameter wird in einer Reihe von Identifikationen mittels Raster-Suchverfahren untersucht, indem sowohl beide Modelle, als auch Daten aus beiden Experimenten genutzt werden. Dabei wird die Anzahl der als unbekannt angenommen, thermischen Modellparametern stetig erhöht. Zusätzlich wird die Modellabhängigkeit und die Sensitivität bezüglich der thermischen Randbedingungen des Ergebnisses analysiert.

Abstract

A material parameter identification framework is proposed, suitable for fully thermo-mechanically coupled constitutive models and based on full field Digital-Image-Correlation (DIC) and thermography measurements. A broad theoretical background of the inverse problem of parameter identification is provided, focusing on the algorithmic treatment of the intrinsically different data sets of displacement (Lagrangian type) and temperature (Eulerian type), the definition of an objective function which compensates rigid body motions and the necessary analysis of the obtained identification results. The latter aspect especially includes theory regarding identifiability, model dependency, verification and validation. Furthermore, the general applicability of the proposed framework is empirically tested on the basis of a simple tension test using an aluminium alloy. More precisely speaking, the data of two different types of experiments is used. One experiment including a cooling stage of the specimen, due to ambient temperature, and one without cooling stage. Based on the experimental observations, two thermo-mechanically coupled constitutive models are chosen, the required constitutive relations summarised and the model parameters interpreted. Using both models and data of both experiments, the identifiability of thermal model parameters is investigated in several identifications by means of a grid search approach, gradually increasing the set of unknowns. Moreover, model dependency and sensitivity of results to thermal boundary conditions are analysed.

Publications

Key parts of this thesis were pre-released as peer-reviewed journal articles, which were either published or submitted during the progress of this work. Modifications regarding the article versions were applied if considered beneficial to the reading flow of this more comprehensive document.

1. L. Rose, A. Menzel: *Optimisation based material parameter identification using full field displacement and temperature measurements*, Mechanics of Materials 145:103292, 2020 [62].
2. L. Rose, A. Menzel: *Identification of thermal material parameters for thermo-mechanically coupled material models*, Meccanica, 65:393–416, 2021 [61].
3. L. Rose, A. Menzel: *On the determination of thermal boundary conditions for parameter identifications of thermo-mechanically coupled material models*, submitted for publication, 2021.

The author of this thesis contributed essential aspects to the articles mentioned above, including the outline of theory and framework, experimental investigations, all of the numerical implementations and simulations, analysis of results, as well as the preparation of the articles themselves. It is worth mentioning that the work at hand is a direct continuation of the author's project- and master thesis, both of which dealt with the parameter identification of purely mechanical constitutive models, based on numerical and real experimental displacement data, respectively.

Contents

1 Introduction

This thesis provides information on the treatment of inverse problems concerning thermo-mechanically coupled material models which are based on real full field measurements. At first, the necessity of an identification scheme for such models is motivated within this chapter, already indicating which of the associated aspects are of interest. Afterwards, the current state of the art is presented in order to finally derive issues and questions so far unaddressed in literature. The main focus of this work lies on providing a general framework for the identification of thermo-mechanically coupled constitutive models on the basis of experiments with a mechanical load as well as on the identifiability of thermal parameters, model dependency and influence of thermal boundary conditions.

1.1 Motivation

In order to perform predictive simulations, e.g. for the optimisation of already existing components, the efficient development of new prototypes or any other kind of mechanics-driven design, the choice of the model parameters is of utmost importance. Inaccurate model parameters lead to non-representative results necessitating the use of suitably high safety factors usually leading to higher production costs. Hence, it seems worthwhile to use constitutive models which represent the material behaviour as accurately as possible and to identify reasonable and valid values for the associated model parameters. More precisely speaking, during some processes the effect of temperature on the material response may not be neglected, necessitating the use of thermo-mechanically coupled constitutive models. For such models the set of required optimal model parameters includes the caloric or thermal as well as mechanical model parameters, so that a general framework is required which enables the identification of suitable model parameters for thermo-mechanically coupled models.

However, even optimal parameters are not useful if the chosen constitutive model itself is not able to represent important key features of the material behaviour under consideration. If, for example, an isotropic yield surface is used to predict the material response of a strongly anisotropic material undergoing inhomogeneous stress states, the computed results will not reflect the real material behaviour, regardless of whether the parameters are optimal or not. Likewise, insufficient experimental data may allow a good fit of a model, but the fitted parameters may not represent any other type of boundary value problem due to overfitting. Although it may be obvious as to what kind of models should be avoided, it is not always clear how certain aspects of a model must be chosen exactly. Regarding the example from before, it is not intuitively clear what kind of anisotropic yield surface fits best to what kind of material, seeing that there are various different formulations established. This knowledge has to be acquired by trial and error, comparing model predictions and experiments. One modelling aspect that has been subject to scientific discussion for almost a century is the question of how to model dissipation within thermo-plastic material models, which can lead to significant temperature raises during forming processes. No final answer exists, so that the impact and requirements of different constitutive model formulations are worth analysing.

Apart from the model formulation, the thermal boundary values can have a notable influence on the predicted material response for a process. Hence, the identification of suitable thermal boundary conditions is vital for any temperature related analysis, be it either a direct or inverse problem which is considered. In common engineering applications boundary conditions of Robin-type often best describe the heat exchange between the body under consideration and its environment. This special kind of thermal boundary condition usually postulates a heat exchange along Newton's law of cooling which requires the temperature of the surrounding medium and a film or heat transfer coefficient. Obtaining the first parameter, i.e. the temperature of the surrounding medium, is usually done by a simple measurement (assuming that this temperature is indeed constant over time). The definition of a suitable heat transfer coefficient, on the other hand, is usually not as simple since its value may depend on material pairing, contact pressure or fluid velocity, general geometry as well as on surface roughness. Precise values for the heat exchange coefficients are therefore difficult to obtain from literature and must in general be identified for each type of boundary value problem. Thus, the possibilities and limits regarding the identification of thermal boundary coefficients alongside thermal model parameters are of interest.

It is therefore worth looking at the current state of the art to find out which aspects - required for a precise identification of valid model parameters for thermo-mechanically coupled constitutive models - have already been established. Afterwards, the precise aim of this thesis is formulated.

1.2 State of the art

The identification of model parameters for thermo-mechanically coupled constitutive models covers several areas of experimental and theoretical solid mechanics. Hence, the overview of the state of the art is split into three parts, i.e. parameter identification in general, modelling and fit of dissipation, and identification of heat transfer coefficients.

Parameter identification Quite some research has already been completed to develop methods for the identification of material parameters for purely mechanical material models. The basic principle of a Finite-Element (FE) based parameter identification, the so called Finite Element Model Updating (FEMU) method is presented and explained in considerable detail in [43] and [46]. The framework is first tested and verified on the basis of numerical experiments, followed by an application to real data. In these works, experimental values were obtained from a standard tensile test by means of gratings on the surface of the specimen and fitted to an isotropic elasto-plastic material model. The determination of parameters for a non-isotropic Hill-type yield surface can be found in [51]. In later years, the concept did not change much but was applied to different kinds of material models, ranging from large strain models [33], to gradient enhanced damage formulations, [45]. At some point, the concept of Digital-Image-Correlation became available as a full field measurement technique for displacement fields and was adapted to easily obtain experimental data for parameter identification. Interpolation and general treatment of such data is addressed in, e.g., [64], [57] and [35]. Further publications mostly focus on different material models, applications or objective functions, whereas the latter usually differ from the one proposed in [43] only in terms of the defined weighting factors. Regarding the shape of the specimens, many different geometries have been used to obtain different stress states, e.g. a notched plate in [16] or different kinds of cruciform specimens in [39], [68], [66] and [76]. A more detailed overview of the state of the art can be found in either [3] or [48].

A slightly different community has concentrated on the identification of thermal properties and parameters by means of different approaches. The first is the use of calorimetry, necessitating special experimental devices which can be used almost exclusively for that purpose. An alternative is the identification on the basis of measured temperature fields, e.g. using the so-called flash method as introduced in [55]. The main idea is to subject a specimen to a short, impulse-like laser beam and to measure temperature changes that occur afterwards. No mechanical loads are applied to the specimen and observation time is kept very short to assume adiabatic boundary conditions for all boundaries that were not subject to the laser beam. Though the original method is based on an analytical solution, the method has been enhanced and extended, c.f. [38] and [2], especially by replacing the analytical solution with a numerical FE simulation. Thus, the identification method itself is remarkably similar to the Finite-Element-Model-Updating (FEMU) method which is now well established for mechanical parameter identifications, as it involves a least square fit of a simulated and measured temperature field. Further use of thermography has been made to analyse heat sources, e.g. in [18] and [17], to identify the temperature dependency of mechanical parameters, e.g. in [50] and [53], or to validate a simulation, e.g. in [63].

Regarding the coupling of temperature and displacement fields, a possibility to combine DIC and thermography data is presented in [41] and is used for the estimation of heat sources during a tensile test. An actual adjustment of thermo-mechanically coupled material models, based on displacement and temperature full field data, is shown in [44] by means of numerical experiments only. Although the conclusion of that paper already suggests the application to real experiments in order to determine caloric quantities, such a comprehensive work has, to the author's knowledge, not yet been published in the context of parameter identification.

Modelling and fit of dissipation One of the first reports regarding the correlation of cold work and heat was published in 1925 by Farren and Taylor, see [22]. Their measurements during dynamic tension tests suggested that a near constant fraction of the cold work was transformed to heat and that the remainder was stored as latent energy in the material. Some time later, Taylor and Quinney reasoned that this finding could not be true for larger strain states, since the latent energy of a material should saturate, see [73]. Within that work, experiments with a twisted rod underlined this line of thought, showing that the dissipated energy depends on the current load state. This led to the introduction of the so-called Taylor-Quinney factor which describes the ratio of cold work to dissipated energy. In later years, a similar factor was introduced to describe the ratio between the rate of cold work, i.e. the stress power, and the rate of dissipated energy, see e.g. [49] and [59]. The latter work also clearly differs between the two aforementioned factors which were usually denoted by the same symbol, albeit describing fundamentally different ratios. At that point, the idea of a strain and strain rate dependent ratio between cold work and dissipated energy was well established, and many further scientific contributions can be found with the focus on the determination of this dependency. Whereas some researchers mainly seek to determine the Taylor-Quinney coefficient experimentally, e.g. in [28], [42] by using a Kolsky (Split-Hopkinson) pressure bar, or in [36] under uniaxial tension, others more strongly emphasise thermodynamical consistency. It has often been stated that the simple replacement of the predicted dissipation of a model with a fraction of the plastic stress power does not necessarily fulfil the first law of thermodynamics, so that a thermodynamically consistent model which accurately predicts the dissipated energy should be used instead. Hence, several modelling approaches have been proposed and their predictions have usually been compared to experimental data of a dynamic Kolsky (Split-Hopkinson) bar test assuming adiabatic conditions, see e.g. [60], [75], [71] and [6]. In the latter work, an additional material parameter is introduced by making an extension to the postulated Helmholtz free energy function. This parameter determines how much energy is stored in the material and how much is dissipated during plastic deformations. Thus, it allows a better adaptation of the model to real material behaviour while still satisfying the laws of thermodynamics.

Although the overview above is just a brief excerpt and many more publications could be mentioned, attention is drawn to only two more approaches to the identification of plasticity induced dissipation. In [58] a slightly different concept is presented which tries to avoid the test of all kind of possible energy formulations and rather aims at deducing an appropriate Helmholtz free energy function directly from experimental data. The approach is tested on data of a tensile test assumed to be adiabatic and compares two fundamentally different plasticity model approaches, i.e. associated and non-associated plasticity. The results show that the associated format is not able to correctly predict the dissipation obtained from the experiment. The second approach can be found in [56] where an inverse analysis with full field displacement and temperature measurements of an inhomogeneous boundary value problem (BVP) is used to fit the mechanical parameters and the evolution of a Taylor-Quinney factor of a simple, not necessarily thermodynamically consistent model to an observed temperature field. However, all other thermal model parameters, i.e. heat capacity, thermal conductivity and thermal expansion were taken from literature and are not part of the optimisation.

Identification of heat transfer coefficients Methods for an inverse analysis in order to determine heat transfer coefficients date back as far as the 1970s, see e.g. [9]. The method presented in that work minimises the difference between experimental and computed data along certain grid points by using finite differences. Thereafter, and with improved computational capability, methods for two-dimensional problems were derived. In [8] the identification of a time and space dependent heat transfer coefficient is demonstrated by means of a spherical body with a symmetric temperature field. Moreover, [15] analyses the heat exchange of an insulated, two-dimensional plate by using the boundary element method. At some point the terms ‘inverse heat transfer coefficient problem’ (IHTCP) and ‘inverse heat conduction problem’ (IHCP) were introduced and associated with the determination of film or heat transfer coefficients by means of inverse problems. Nowadays, the identification of heat transfer coefficients for three-dimensional boundary value problems poses no further computational problem and makes use of common solution methods for the underlying differential equations such as the Finite Volume Method, see e.g. [19], or the Finite Element Method, see e.g. [20]. However, all methods mentioned above require at least a subset of the classic thermal material parameters to be known, which especially includes the thermal conductivity of the body under consideration. As was already mentioned above, these material parameters are usually identified through highly specialised experiments, e.g. by using a guarded hot plate, see e.g. [23], or laser flashes, see e.g. [55] or [2]. For the inverse analysis of these experiments either isothermal or adiabatic boundary conditions are applied, so that a heat transfer coefficient is not required and therefore neither needs to be estimated nor identified.

1.3 Outline and aim

The current state of the art shows that identifying the parameters of a thermo-mechanically coupled constitutive model is usually done in two parts, fitting the mechanical and thermal model parameters independently from each other on the basis of different experiments. Thus, the classic identification of thermal model parameters requires highly specialised experiments and equally specialised equipment, the former of which are performed without applying mechanical load to the specimen. A potential alternative was already proposed, i.e. the identification of both sets of parameters on the basis of experiments under mechanical load leading to dissipation induced self heating of the specimen. This alternative approach requires almost no additional equipment, apart from what is already necessary for the fit of mechanical model parameters anyway. However, this approach was so far only shown on the basis of numerical experiments and was not pursued any further. Consequently, the fundamental questions related to that identification approach also still require further research.

Hence, it is the aim of this thesis to provide a framework for the identification of mechanical and thermal material parameters on the basis of real experimental displacement and temperature field data as well as answering questions related to the identifiability of thermal parameters, model dependency and influence of thermal boundary conditions. More precisely speaking, it is explicitly not the aim of this work to perform an identification, the results of which can be used for predictive simulations of different geometries and stress states, but rather to establish the underlying framework for parameter identification based on (potentially) inhomogeneously distributed displacement and temperature fields. To that end, this thesis is structured as follows.

In Chapter 2, a theoretical background is provided with respect to the definition of the inverse problem of parameter identification, possible solution strategies in general, as well as detailed information especially on the FEMU method. Commonly used optical measurement methods for displacement and temperature field are briefly explained in order to motivate the specific treatment of temperature data in the proposed framework. In that context, sources of errors that should be avoided during measurements are mentioned. The algorithmic framework for the necessary pre-processing of temperature and displacement data is then presented, followed by possible definitions of the objective function. Different options are briefly discussed, introducing a newly proposed definition of relative displacements as a measure which intrinsically compensates rigid body motions. The commonly encountered sources of errors related to the parameter identification scheme are summarised, including errors related to the model formulation, necessitating the definition of identifiability criteria to determine whether or not an optimisation result is (locally) unique. Finally, the concepts of verification and validation, as well as the difference between model and material parameters are briefly discussed, once again focusing on the effect which different model formulations may have on an identification process.

After providing the required framework, the aspect of identifiability is empirically investigated. This is done by means of several proofs of concept using real experimental data as well as constitutive models.

In Chapter 3, the experimental data required for the specific identifiability analysis is shown, starting with the introduction of the measurement equipment, the geometry of the specimens and the general experimental setup. A simple tension test with specimens made of the aluminium alloy AW6016 is chosen as the basis for the proofs of concept at hand and the obtained experimental data is analysed with respect to the required features of a constitutive model.

In Chapter 4, two constitutive models are presented which are based on commonly used standard model formulations for associated and non-associated plasticity. More precisely speaking, a term is added to the assumed free energy expression, introducing an additional model parameter which does not influence the mechanical material response but allows a scaling of the predicted dissipation while maintaining a thermo-dynamically sound framework. The two models themselves feature an almost identical mechanical material response and mainly differ in the expression for the predicted dissipation. For each model, the dissipation follows directly from the postulated potentials and is a function of the current load state, requiring no further assumptions, e.g. regarding the relation towards cold work. The chapter closes with an analysis of the constitutive equations in order to determine which model parameters can and which can not be identified on the basis of a simple tension test. While doing so, it is shown that a simple assumption on the influence of the low, experimentally detected temperature rise allows the decomposition of the identification process into three stages, whereby only subsets of the total material parameter set are optimised within the respective stage.

In Chapter 5, the actual analysis of identifiability regarding the thermal model parameters is performed, combining the framework, the experimental data and the constitutive models from the previous chapters in a successive identification scheme, concentrating on the questions

- Does the proposed framework allow an identification in general?
- Does the use of relative displacements compensate rigid body motion as is expected?
- Is a (locally) unique fit of the three classic thermal model parameters possible on the basis of simple tension test?

At first, however, the underlying boundary value problem as well as details of the identification scheme are specified. With this information at hand, the identifiability of the three classic thermal material parameters of a simple standard model is shown by means of a grid search approach. While doing so, it is also shown that the proposed framework is sound and that the newly proposed error measure of relative displacements does indeed intrinsically compensate rigid body motions. In a second step, the two extended, non-standard models are compared in the context of parameter identification, focusing on the identifiability of the enlarged set of unknown thermal model parameters by answering the questions

- How do the different model formulations presented in Chapter 4 affect the optimal values of the model parameters?
- Is a (locally) unique fit of the thermal model parameters possible, if the dissipation related parameter β is included as an additional unknown?

- What kind of experimental data is required to ensure identifiability of all four thermal model parameters?

The parameters of both models are fitted to the experimental data of either of the two experiments presented before to see what kind of data is necessary for a (locally) unique fit. The obtained results are presented and analysed with respect to the remaining error, possible correlations and validity. In a last set of identifications, the identifiability of thermal boundary coefficients (required for Newton's law of cooling) alongside the thermal model parameters is shown by again using the grid search approach. Related questions are

- Is a (locally) unique fit of thermal model parameters and boundary coefficients possible on the basis of full field temperature measurements?
- How sensitive are the resulting parameter values with respect to the (measured) boundary temperatures required for Newton's law of cooling?

Before the identifiability of thermal material parameters alongside thermal boundary coefficients is analysed, however, the objective function, the mechanical material parameters used for the simulation as well as a reference solution obtained with prescribed boundary coefficients are introduced. With this information at hand, a grid search optimisation is performed to study the identifiability and uniqueness of the obtained solution within a certain area in parameter space. The resulting parameter values as well as the material response of the simulation based thereon are compared against the reference solution. Thus, the improvement in precision using optimised boundary conditions is shown in terms of both relative and absolute error improvement. The sensitivity of the optimum with respect to the prescribed temperature values of the external media required for Newton's law of cooling is analysed thereafter by rerunning the identification several times with different, prescribed external temperatures. Finally, the possibility of identifying only a subset of thermal material parameters and boundary coefficients is explored, prescribing the values of those thermal material parameters which can be identified by means of specialised experiments and which are usually available in literature, i.e. thermal expansion, heat capacity and thermal conduction. The obtained result is again compared against the fully optimised material response.

In Chapter 6, the answer to the questions above are explicitly given and the main results are summarised. Although not the focus of this thesis, the possibility to obtain valid parameter sets is furthermore commented on. The chapter closes with a short outlook on possible extensions and future research directions.

2 Theory of parameter identification

The theoretical background of a full field measurement based parameter identification for thermo-mechanically coupled material models is provided in this chapter, focusing on the Finite-Element-Model-Updating (FEMU) method, as well as on the handling of experimental data. More precisely speaking, information necessary for the implementation of a FEMU scheme suitable for thermo-mechanically coupled material models are given. Furthermore, the operating principle of commonly used measurement devices are briefly explained in order to devise suitable and reasonable experimental setups and enable an appropriate (pre-)processing of the obtained data.

To do so, the chapter is structured as follows. The definition of the direct and inverse problem is given first, underlining the dependencies of the solution for a parameter identification. A possible solution technique for the inverse problem is shown next, introducing the general structure of the FEMU method and briefly distinguishing this scheme from other established solution techniques. The chosen solution technique requires experimental data and a pre-processing of said data, which is addressed in the subsequent section. Thus, the general framework is followed by information on full field measurements of displacements and temperatures using Digital-Image-Correlation (DIC) and thermography, highlighting aspects which have a direct influence on the experimental setup and the treatment of measured data. The necessary pre-processing steps of experimental data, i.e. the interpolation, are explained thereafter. As a vital part of the FEMU method, the choice of an objective function is discussed, introducing a formulation which intrinsically compensates rigid body motions of the testing machine. Afterwards, more general sources of errors are outlined including errors related to the choice of a model formulation. From that, the definition of identifiability criteria is motivated, in order to determine whether or not an optimisation result is (locally) unique. Finally, the necessity of verification and validation, as well as the difference between model and material parameters are briefly discussed, focusing on the effect which different model formulations may have on an identification process.

2.1 The direct problem

The solution of the direct problem is usually of interest for predictive simulations. It is defined as the solution of a boundary value problem with given geometry, boundary values $\boldsymbol{\beta}$, material parameters $\boldsymbol{k}$ and constitutive material model represented by a set of constitutive equations $\boldsymbol{\mu}$. The sought for quantities are usually displacements, temperatures or derived quantities such as stress, strain or heat flux, see Figure 2.1a. According to [43] the direct problem can mathematically be defined as the search for a valid output quantity $\mathbf{d}$ which satisfies a set of residual functions $\mathbf{b}$

$$\mathbf{d}\left(\boldsymbol{k};\, \boldsymbol{\beta},\, \boldsymbol{\mu}\right) = \operatorname{Arg}\{\mathbf{b}\left(\mathbf{d};\, \boldsymbol{\beta},\, \boldsymbol{k},\, \boldsymbol{\mu}\right) = \mathbf{0}\}\ , \tag{2.1}$$

with $\mathbf{g}$ being, for example, the weak forms of the balance equations for linear momentum and energy. As visualised in Figure 2.1, one of the so-called inverse problems is obtained by switching one of the input parameters with the output quantity of the direct problem.

2.2 The inverse problem of parameter identification

The main intention of a parameter identification is to fit the predicted material behaviour of a simulation to the real material response by solving the associated inverse problem which is graphically depicted in Figure 2.1b. The inverse problem of parameter identification requires a given geometry, boundary values $\boldsymbol{\beta}$, a set of constitutive equations $\boldsymbol{\mu}$ and an experimental material response $\mathbf{d}^{\text{exp}}$ as input data and solves for a set of model parameters

$$\boldsymbol{k}\left(\mathbf{d}^{\text{exp}};\, \boldsymbol{\beta},\, \boldsymbol{\mu}\right) = \operatorname{Arg}\{f\left(\mathbf{d}^{\text{exp}},\, \boldsymbol{k};\, \boldsymbol{\beta},\, \boldsymbol{\mu}\right) = 0\}\ , \tag{2.2}$$

so that an objective function f is satisfied. Keeping the aim of a parameter identification in mind, the objective function is usually chosen to represent the gap between the predicted material behaviour and some observed material response. A basic example for such a formulation reads

$$f\left(\mathbf{d}\left(\boldsymbol{k};\, \boldsymbol{\beta},\, \boldsymbol{\mu}\right),\, \mathbf{d}^{\text{exp}}\right) = \left[\mathbf{d}^{\text{exp}} - \mathbf{d}\left(\boldsymbol{k};\, \boldsymbol{\beta},\, \boldsymbol{\mu}\right)\right]^2\ , \tag{2.3}$$

and is simply the error squared between the observed and computed material response. It is worth noting that the experimental data set $\mathbf{d}^{\text{exp}}$, the boundary conditions $\boldsymbol{\beta}$ and the constitutive model $\boldsymbol{\mu}$ are treated as constants (as indicated by the separation through a semicolon in the list of arguments) within one parameter identification process, so that the formal dependency in Equation (2.3) is usually omitted. The definition of the objective function is not unique and more elaborate formulations can be found in Section 2.6. However the specific choice of an objective function may be, the number of experimental data in general exceeds the number of unknown model parameters, rendering this problem ill-posed, c.f. [43]. Therefore, a solution as defined in Equation

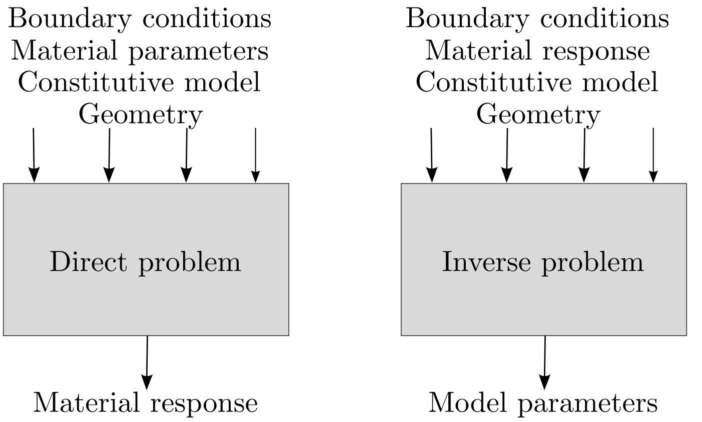

(a) The direct problem.

(b) Inverse problem of parameter identification.

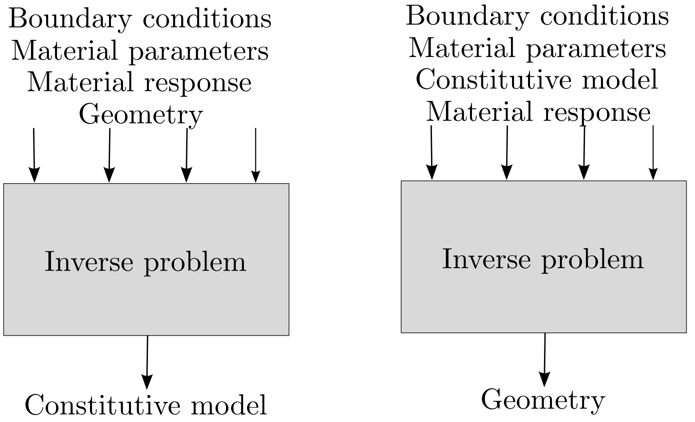

(c) Inverse problem of material modelling.

(d) Inverse problem of structural optimisation.

Figure 2.1: Comparison of direct and inverse problem.

(2.2) which satisfies the objective function exactly does not exist and the problem is reformulated as a minimisation problem

$$\min_{\boldsymbol{k}} f\left(\mathbf{d}\left(\boldsymbol{k}\right)\right) \ , \text{ s.t. } \mathbf{h}\left(\boldsymbol{k}\right) = \mathbf{0}, \, \mathbf{g}\left(\boldsymbol{k}\right) \leq \mathbf{0} \tag{2.4}$$

which can be subjected to equality and inequality constraints **h** and **g** respectively.

Remark 2.1. Although the formal dependency of the inverse problem on the chosen constitutive model is omitted in Equation (2.4), it is nevertheless important to keep especially this dependency in mind. Different constitutive models might lead to significantly different model parameters, since the solution of a parameter identification are not necessarily the true material parameters but rather the optimal parameters for the provided input, as is discussed in greater detail in Section 2.9.3 and exemplarily shown in Section 5.4.

2.2.1 Solution techniques

An analytical solution to the inverse problem of parameter identification exists only for very simple constitutive models, e.g. linear elasticity. In general, an optimisation based parameter identification scheme is required to solve the minimisation problem defined in Equation (2.4) and a couple of different methods have been proposed to do so, see [3] and [48]. Most prominent are the Constitutive Equation Gap Method (CEGM), the Virtual Fields Method (VFM) and the Finite Element Model Updating (FEMU) method. In contrast to other methods available, the FEMU method can handle a wide variety of experimental data, is applicable to almost all kinds of boundary value problems and has no restrictions regarding the position of available experimental data on or within the body considered. Furthermore, the intrinsically modular structure is easy to implement and allows the incorporation of already existing toolboxes, for either the optimisation or FEM routine. For these reasons the FEMU method is used within the thesis at hand. Since the underlying idea of this scheme is to compare the solution of a Finite-Element-Method (FEM) to the experimental data and iteratively update the model parameters until some convergence criterion is met, an algorithmic structure as is presented in Figure 2.2 naturally arises. This structure allows the use of almost every optimisation scheme and the optimisation with respect to any physical quantity as long

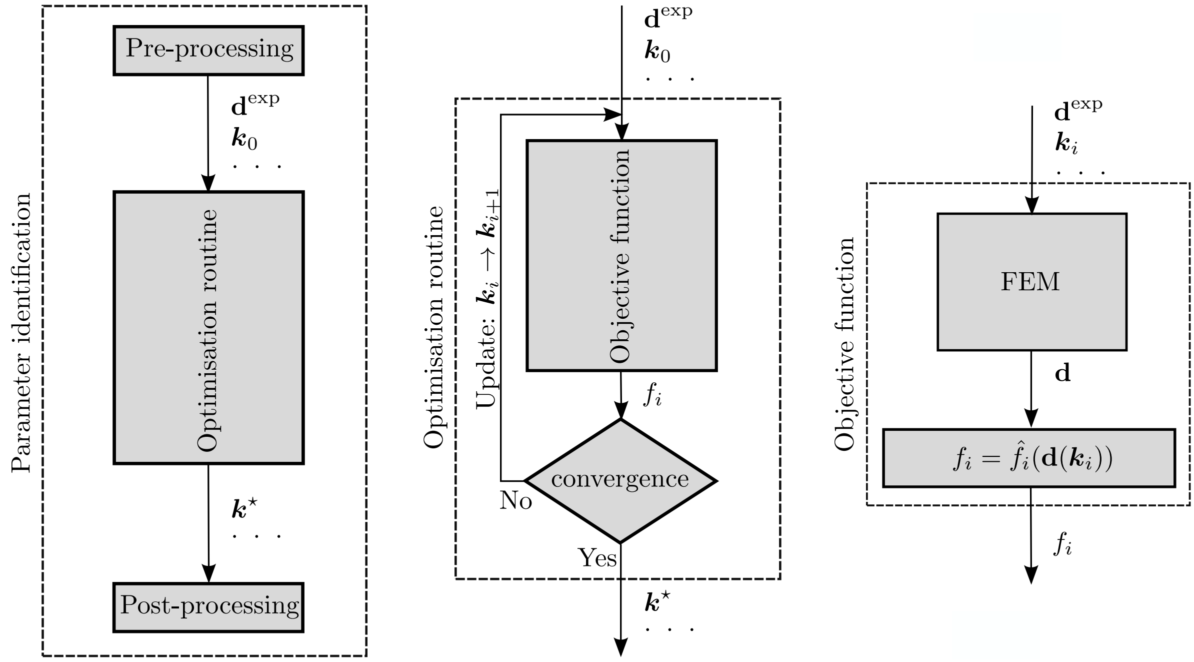

(a) Parameter identification routine.

(b) Optimisation routine.

(c) Assembly of objective function.

Figure 2.2: Flow diagram of parameter identification routine.

as it is observable or at least derived from observable quantities. Commonly used are the reaction force F, the temperature field θ, the displacement field $\mathbf{u}$, the strain field $\boldsymbol{\varepsilon}$ derived from $\mathbf{u}$, or a combination of those measurands. Usually, reaction forces are obtained using conventional load cells. Concerning the measurement of temperature and displacement field however, more advanced methods are required.

2.3 Optical displacement measurement

One possibility to measure the displacement field of a specimen lies in the principle of digital image correlation (DIC). It allows the capturing of the three dimensional displacement field of a specimen surface throughout an experiment. A detailed description and derivation of this technique can be found in [74] and an extensive analysis of the method is provided in [25], Chapter 5, so that only a brief overview is given within this section.

The setup for this kind of displacement measurement is fairly simple. One or more charge-coupled device cameras (CCD cameras) take pictures of the initial and every subsequent loading stage. By comparing each picture either with the reference or the preceding stage, movement of individual areas can be tracked. To do so, the picture is divided into rectangles, called facets, with a side length of some pixels, see Figure 2.3. Each facet is represented by its grey value distribution which is assumed to be unique within a certain neighbourhood. To fulfil this assumption the surface of the specimen must either feature a natural pattern, or a stochastic pattern has to be applied manually. Figure 2.4 shows an example for both cases. It is worth noting that the size of the facets needs to fit to the observed pattern. Large speckles, for example, require larger facets. If too small, some facets may be completely filled by speckles so that the grey value distribution is not unique. Practically, the applied pattern is usually chosen to match the desired facet size, since the facet size also defines the smallest observable material effect, e.g. some shear band moving through the specimen. However, if the grey value

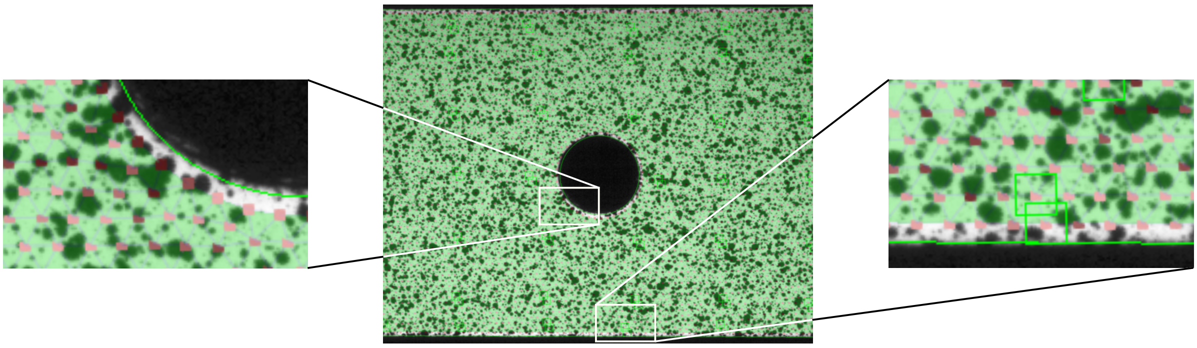

Figure 2.3: Field of facets for optical displacement measurement. Red dots indicate centre of each facet where displacement data is available. Only some facets are exemplarily shown.

(a) Natural pattern. (b) Unsuitable surface. (c) Manually applied pattern.

Figure 2.4: Example for suitable patterns which allow a displacement measurement via DIC.

distribution of a facet is indeed unique, this distribution is traced throughout each frame that was made during the experiment. The resulting displacement is then assigned to the midpoint of the respective facet. A closer look at Figure 2.3 reveals that displacement data may be unavailable exactly at the edge of a specimen, since some software packages do not consider facets which protrude over the edge of the specimen for the sake of precision. For such cases, the midpoint of a traceable facet can never lie on the edge of the observed surface. This is important to keep in mind if data is required directly on the edge, because it would mean to extrapolate data onto this position, which is a potential source of error if not treated carefully, see Section 2.7. Another source of error to be aware of is the choice of a reference stage for the computation of experimental displacements. Some systems provide the option to trace changes from image to image which might allow a matching of related facets under large distortions, but can also lead to a substantial build-up of systematic and random errors. Comparing images against the initial stage will intrinsically avoid this problem, see Figure 2.5.

Structure of DIC data A DIC system intrinsically uses a Lagrangian approach of recording data, due to the fact that it traces the movement of certain material points (represented by a facet). Thus, for each observed point of the reference configuration, a set of displacements is available describing the path of the associated point through space, evaluated at discrete time steps, see Figure 2.6. This structure of DIC data has a direct influence on the way it must be treated during pre-processing.

2.4 Optical temperature measurement

Regarding the measurement of temperature fields, infra-red thermography presents a non-contact method with a high availability of corresponding devices. The key component of such a thermography system is a sensor array which detects electromagnetic

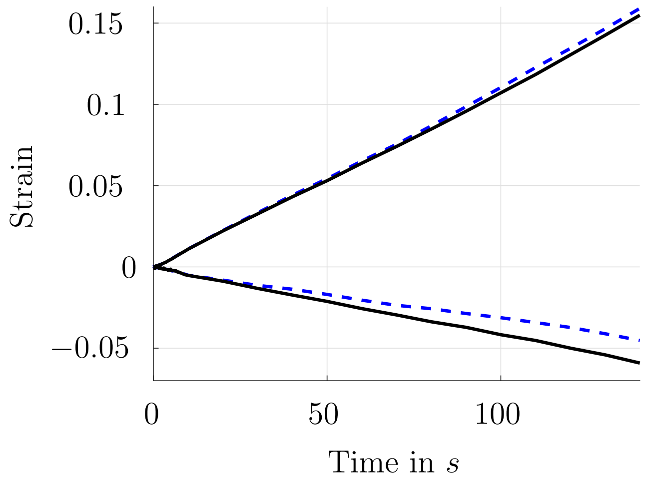

Figure 2.5: Example of strain in tension and lateral direction using the initial stage (–) and the preceding stage (--) as reference for the computation. Difference of up to 2% in tension direction and 25% in lateral direction.

waves with certain wavelengths. The temperature which corresponds to the registered radiation is then computed using well known laws of thermodynamics, e.g. Kirchhoff's law of thermal radiation and Planck's radiation law, see [10] Section 13.2. The temperature associated with each sensor is furthermore visualised in a thermogram by assigning a certain colour to each temperature value. Hence, each pixel of a thermogram represents the temperature obtained from one sensor. Regarding these sensors, different types can be used within thermography systems, which differ in the underlying measurement principle (e.g. thermal- vs. photon detector), thermal resolution as well as in the required integration time of each sensor, cf. [10] Section 13.9. Furthermore, thermography systems usually do not read all sensor values simultaneously, which can lead to a temporally distorted thermogram, the significance of which depends on the underlying method (reading data row-wise or snap-shot method) as well as on the characteristic time scale, i.e. speed, of the process observed.

It is worth emphasising that thermography systems do not detect the whole infra-red spectrum but only a certain range of wave lengths. Usually, this range lies within one of the so-called atmospheric windows. Figure 2.7 shows the transmission coefficient of air τ as a function of the observed wavelength, and the atmospheric windows are those areas where the air absorbs as little of the infra-red radiation as possible ($\tau \approx 1$). Most systems either make use of the medium-wavelength (3 - 5 μm) or the long-wavelength window (> 8 μm). The detected wavelength is of importance especially if different coatings are applied to the specimen, since the emission coefficient of most paints differ significantly from each other for medium-wavelengths, but tend to coincide for longer wavelengths, see Figure 2.8. Hence, a speckle pattern should only be observed using a thermography system if the emission coefficients of both coatings coincide for the detected wavelengths. Otherwise, it is not possible to compute the correct temperature of

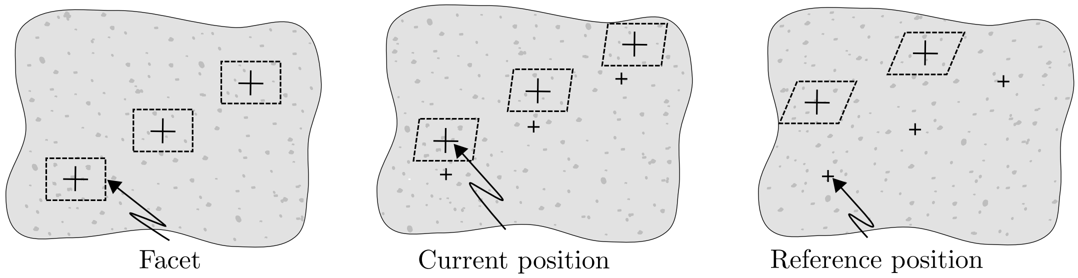

(a) Reference configuration at time t_0.

(b) Deformed configuration at time $t_1 > t_0$.

(c) Deformed configuration at time $t_2 > t_1$.

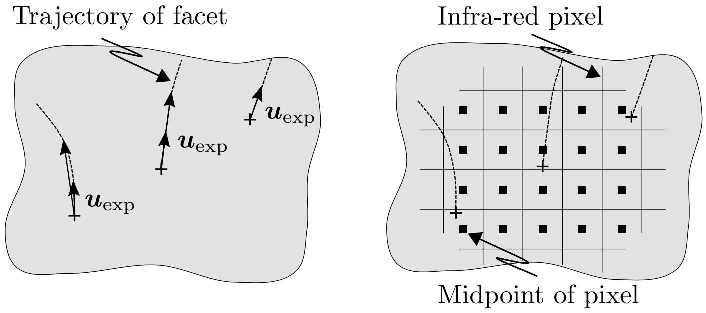

(d) Trajectory of facets.

(e) Position of infra-red pixel is fixed for all time steps.

Figure 2.6: Measured displacements of each facet are assigned to reference coordinates of the facet. Measured temperature of one infra-red pixel is assigned to the stationary midpoint of the pixel and may correspond to different facets at different time steps.

the speckled surface since the appropriate emission coefficient for each pixel is unknown. That is if one pixel happens to contain part of a white and part of a black area, the detected temperature will be smeared and averaged. Apart from the emission coefficient, the temperature of the surrounding area is also of importance. Every body with a temperature greater than zero Kelvin emits radiation that is reflected from each surface with an emission coefficient $\varepsilon < 1$ as exhibited by almost every common material and coating. Most thermography systems can compensate the homogeneous and constant reflection of a body in the observed surface if the temperature of the reflected body is known. Thus, it is crucial to avoid a time dependent or inhomogeneously distributed irradiation, e.g. due to nearby machines heating up or to moving people reflecting on the surface, especially if only small changes in temperature are expected. One simple way to avoid the influence of external radiation is the use of cardboard screens to cover the observed body. Alternatively, glass plates can be used in case a transparent screen is required, see for example Section 3.3, since glass has a high transmission coefficient for electromagnetic waves in the visible, but a rather low transmission for waves in the infra-red spectrum. Thus, it may not block all of the external radiation but it leads to a significant reduction. Although the glass screen may heat up and emit infra-red

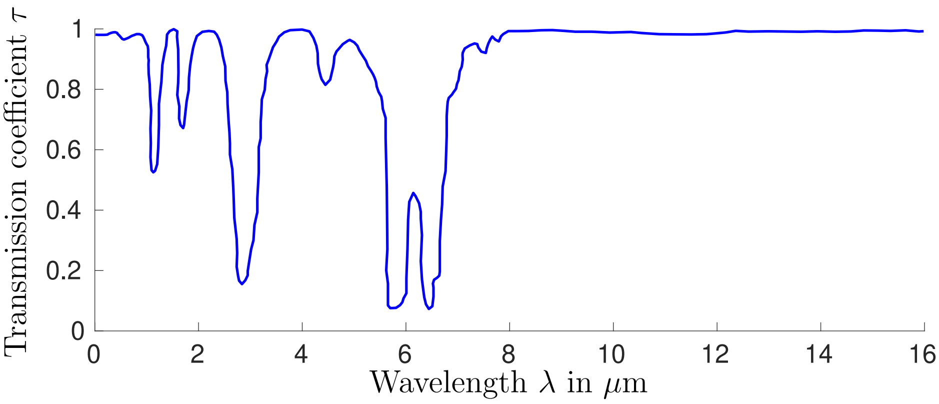

Figure 2.7: Transmission coefficient of air. Pathlength $l = 1$ m, relative humidity $u = 75$ %, temperature $T = 32\ ^{\circ}C$. Courtesy of Optris GmbH.

radiation itself, it does so in a more homogeneous way due to its own conductivity. Regarding the different types of detectors used for thermography systems, it must be chosen according to the measurement requirements, see [10] Chapter 14. Thermal detectors, e.g. microbolometer or pyrometer, are usually inexpensive and do not require additional cooling. Compared to photon-detectors, however, they have a lower thermal resolution and higher reaction time. Photon-detectors are to be preferred for high accuracy and dynamic measurements, but require a cooling of the detector (around 100 K or even less), rendering them more complex and expensive. Furthermore, an actively cooled system should not be used for measurements immediately after powering up but needs some time (around $1 - 2$ hours) to reach a steady state. Independent of the detector type chosen, thermography systems often use an at regular intervals reoccurring offset-correction to compensate thermal drift of measurement data, cf. [10] Section 14.5.6. The time between these corrections is usually significantly larger for the actively cooled photon-detector systems if compared to e.g. a system with microbolometer. This automated adjustment may be suppressed during measurements, but at the cost of the afore mentioned thermal drift over time.

Structure of thermography data In contrast to DIC systems a thermography system uses an Eulerian approach of recording data. It does not track points, but detects the temperature of points moving through a position fixed in space, i.e. the infra-red pixel, see Figure 2.6. For each of these infra-red pixel, a discrete set of temperatures is available which describes the temperature history of the associated position fixed in space. It is worth noting that the thermography system has no information about the length scale of the observed surface, so that the exact position of each pixel in a coordinate system is not available. All that is known is the order of pixels within the thermogram. Thus, a fundamentally different treatment of thermography and DIC data is required.

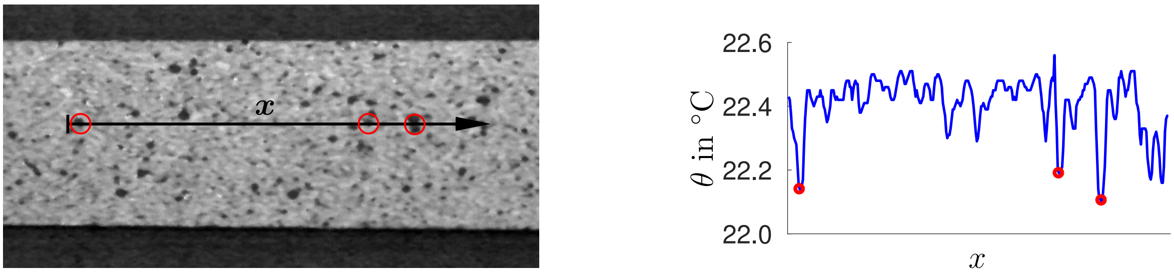

(a) Thermogram of the specimen at room temperature, using medium wavelengths. Single speckles are distinguishable.

(b) Different emission coefficients of the coatings at medium wavelength result in seemingly inhomogeneous temperature distribution.

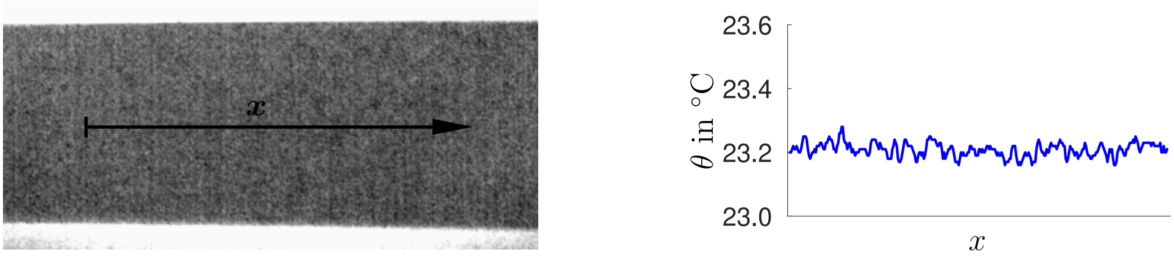

(c) Thermogram of the specimen at room temperature, using long wavelengths.

(d) Homogeneous temperature distribution is detected at long wavelengths.

Figure 2.8: Temperature measurement of a speckled specimen using different wave lengths. The emission coefficient ε of the coatings is different for medium-wavelengths and coincides for longer-wavelengths. Since the true emission coefficient is unknown, $\varepsilon = 1$ was used in both cases for the computation of temperature values, hence the deviation between the levels of temperature in (b) and (d).

2.5 Interpolation of experimental data

Usually, an error-squared like objective function representing the difference between experiment and simulation is used within the FEMU method, see Section 2.2. A meaningful error measure, however, is only obtained if the experimental and simulated data points subtracted within the objective function are somehow related to one another. This relation is not uniquely defined and different approaches can be found, several of which are used within literature. Compared data must certainly refer to the same point in time, but whether it is some time step of the experiment, of the simulation or some other time point is a matter of personal choice. Regarding the position in space, experimental and simulated data could refer to the same point in the current configuration, or it could refer to the same material point, i.e. the same position in the reference configuration. Following the first approach, different material points of simulation and experiment are compared at every iteration and may even change from time step to time step, see Figures 2.9a-2.9b. Thus, data must be interpolated at every iteration of the identification routine since the position at which simulated data is available (the FE nodes) at a certain time step changes with the model parameter set and therefore with

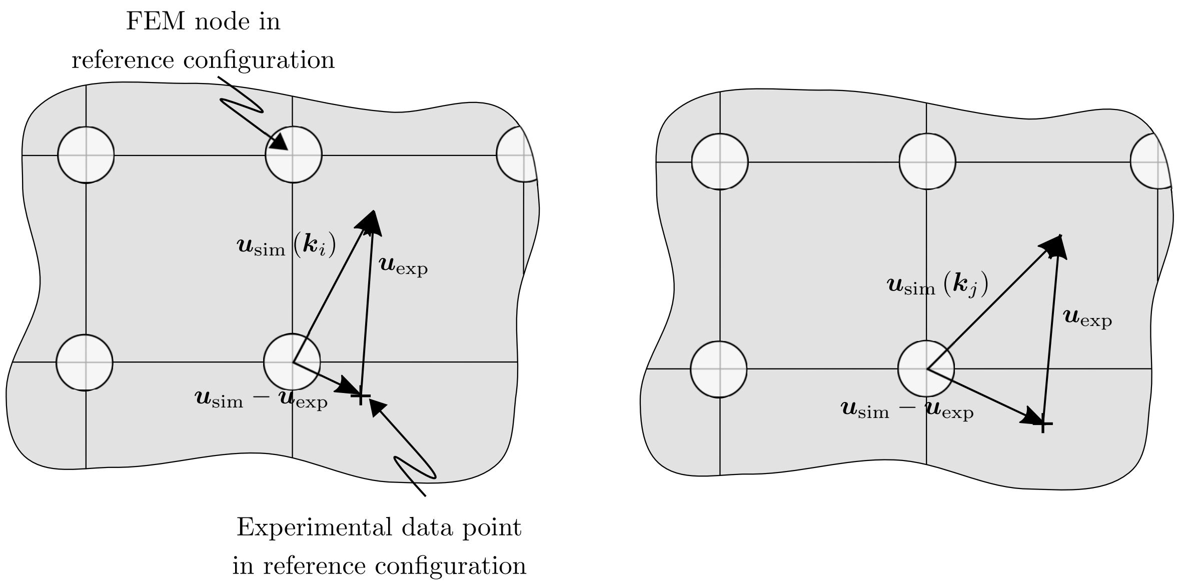

(a) Comparing data at the same point in current configuration, iteration i.

(b) Comparing data at the same point in current configuration, iteration j.

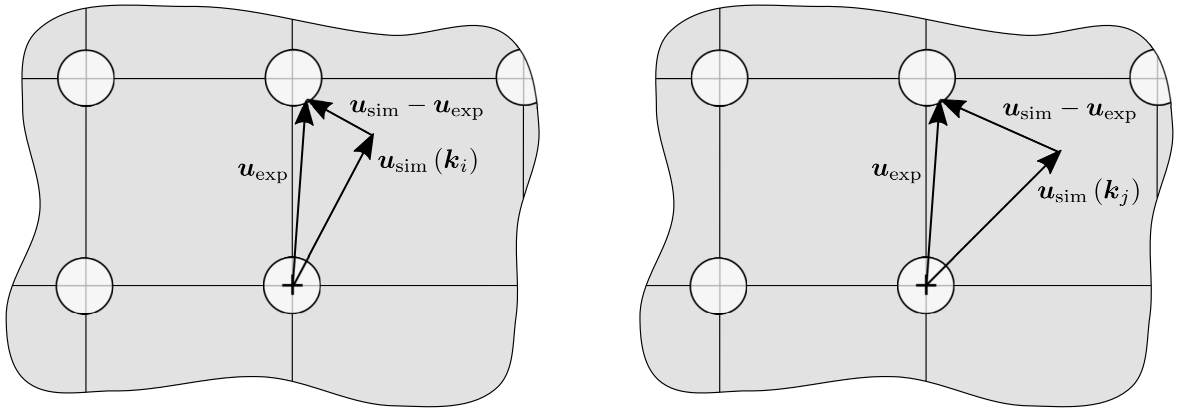

(c) Comparing data at the same point in reference configuration, iteration i.

(d) Comparing data at the same point in reference configuration, iteration j.

Figure 2.9: Different material points are compared at every iteration step, if displacements at the same point in the current configuration are used, necessitating repeated interpolations. Comparing data of the same point in the reference configuration can be done with one interpolation during the pre-processing step.

each iteration. If, however, data of the same material point is compared, an interpolation of experimental data is only required once since the position of the FE nodes in the reference configuration does not change, see Figures 2.9c-2.9d. Apart from the fact that the choice should make no difference if close enough to the solution of the inverse problem, the latter approach is usually preferable in terms of efficiency. Within this thesis, the second approach is therefore chosen, comparing data of the same material points, whereas experimental data is interpolated to match the position in time and space of computed data as follows.

2.5.1 Displacements

The interpolation of displacements is rather straight forward and has already been described in several publications such as [64], [57] and [34]. It takes advantage of the fact that a DIC system intrinsically uses a Lagrangian approach of recording data, tracing the movement of certain material points as is explained in Section 2.3. A list of experimental displacements is associated with each observed point of the reference configuration, describing its path through space. Hence, it is possible to use the coordinates of the points in the reference configuration to interpolate the sets of experimental displacements onto the position of the FE nodes in the reference configuration, see Figure 2.10a. Due to the high density of data points, a linear interpolation as shown in Algorithm 2 is usually sufficient and can be performed once during pre-processing of the parameter identification routine.

2.5.2 Temperature

The required interpolation scheme for temperatures differs fundamentally from the one used for the displacements, since a thermography system does not track material points, but detects the temperature of different material points moving through a position fixed in space, see Section 2.4. More precisely speaking, the position of each FE node in the deformed configuration is required in order to map the experimental temperatures onto these coordinates. This can be done either in every iteration step of the identification procedure using the computed displacements of the simulation, or once during pre-processing if the experimental displacement field is utilised, see Algorithm 3. Following the latter approach, the experimental displacements of a material point associated with the reference position of an FE node is computed as described in Section 2.5.1, yielding its (experimental) position in the current configuration. The experimental temperatures of the corresponding time step can then be interpolated onto the current position which the material point had in the experiment as is shown in Figure 2.10b. Thus, for each material point considered a set of experimental displacements and temperatures is known and the reference positions of all material points coincides with the reference positions of the FE nodes.

2.5.3 Time

So far, experimental data has been mapped onto the same position in space. In order to enable a comparison of experimental data with simulated data, however, the position in

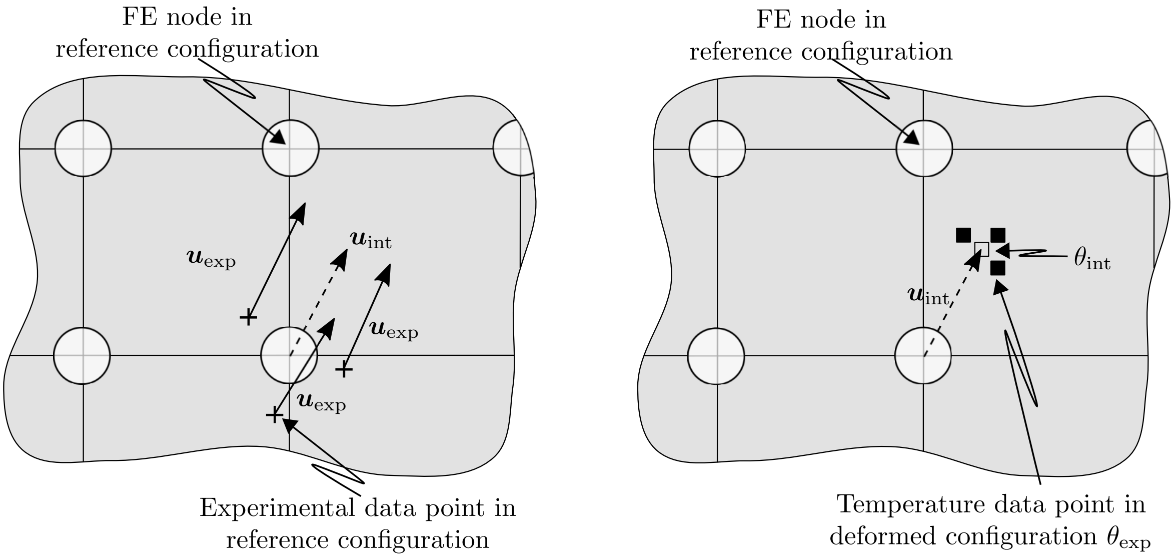

(a) Linear interpolation $\boldsymbol{u}_{\mathrm{int}}$ of experimental displacements $\boldsymbol{u}_{\mathrm{exp}}$ onto the reference position of a FE mesh node.

(b) Linear interpolation θ_{int} of experimental temperatures θ_{exp} onto the current experimental position of a FE mesh node.

Figure 2.10: Linear interpolation of measurement data to obtain a set of experimental displacements and temperatures associated with a certain point of the reference configuration.

time has to be identical as well. If the frequency of the thermography and DIC system is chosen to be sufficiently high, a linear interpolation in time between the two closest experimental time points is an appropriate choice.

2.5.4 Coordinate systems

Since coordinates of the reference and deformed configuration are used, any interpolation scheme can only be performed if all coordinate systems are identical in position and orientation. Concerning the FE mesh, the coordinate system is chosen by the user, and common DIC systems usually have an option to shift the coordinate system as well. This leaves only the data of the thermography system which needs a suitable coordinate system. Since infra-red cameras are usually not used or designed to measure the dimension, elongation or point positions of a specimen, the thermography system has, unlike the DIC system, no information regarding the length scale. Temperatures are assigned to each pixel so that an algorithm has to be applied which converts the position of each pixel within the picture into a position in a chosen coordinate system. To do so, some points must be selected manually on the infra-red image at characteristic locations of the specimen, see Figure 2.11a. The blue points (■) could theoretically also coincide with the green ones (○) and were only chosen in the form shown in Figure 2.11a for the sake of visibility. In the example displayed in Figure 2.11a the coordinate system of the displacement data was aligned with the specimen and positioned at its centre. For other cases, different points may be used, but the approach depicted in Algorithm 1

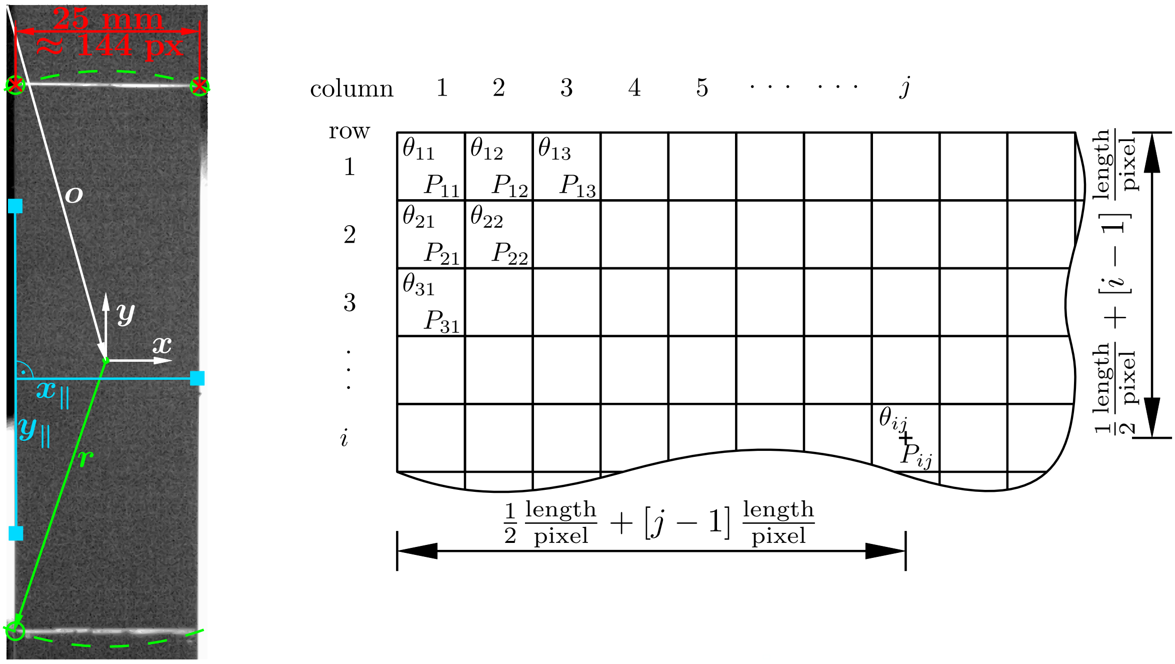

(a) Example of characteristic points.

(b) Position of pixel P_{ij} in ith row and jth column in initial coordinate system using the known length scale.

Figure 2.11: Definition of coordinate system by means of characteristic point using an infra-red image.

and explained hereafter remains the same. At first, the red points (+) are used to define a line with a known length so that the length scale can be computed. Thus, each pixel midpoint can be assigned to a coordinate in a coordinate system which is positioned at the top left corner of the image with its axes parallel to the image borders, see Figure 2.11b. The basis of this initial coordinate system is henceforth represented by $\bar{\boldsymbol{e}}_i$. Afterwards, a circle is specified by means of three points on its circumference (○). These points are chosen in such a way that the centre of the circle $\boldsymbol{o} = o_i\,\bar{\boldsymbol{e}}_i$ is identical to the position of the coordinate system used for the displacement data. Thus, the coordinates of the pixels must simply be shifted to match the new origin. Finally, the orientation of the axis can be adjusted by using the blue points (■). They define a vector parallel to the specimen edge, as well as the orientation of the desired coordinate systems basis $\boldsymbol{e}_i = R_{ij}\,\bar{\boldsymbol{e}}_j$. Hence, the coefficients of the rotation tensor $\boldsymbol{R} = \boldsymbol{e}_k \otimes \bar{\boldsymbol{e}}_k$ can be computed and applied to further transform and align the coordinate system with the edge of the specimen. A similar procedure can be found in [41].

```
Load picture
  → Save order of all pixels.

Define length scale
→ Get row and column of two pixels $P_{ij}$, $P_{kl}$ defining a line (+).
→ Insert length of line $l_\mathrm{m}$ in mm.
→ Compute length of line in pixel (px)
      $l_\mathrm{p} = \sqrt{[k-i]^2 + [l-j]^2}\,.$
→ Compute length scale in mm per px
      $s = \frac{l_\mathrm{m}}{l_\mathrm{p}}\,.$

Define initial coordinate system
→ Set origin at top left pixel.
→ Define axes parallel to picture borders.

Define new coordinate system
→ Get row and column of two pixels on one side of specimen (■).
→ Define vector $\boldsymbol{y}_{\|}$ along side of specimen.
→ Get row and column of a third pixel on other side of specimen(■).
→ Define vector $\boldsymbol{x}_{\|}$ perpendicular to $\boldsymbol{y}_{\|}$ through third point.
→ Get row and column of three pixels on circle around centre of specimen (○).
→ Compute position of centre point.
→ Compute rotation tensor $\boldsymbol{R}$ transforming initial into new coordinate system.
→ Compute offset vector $\boldsymbol{o}$ between origins.

Assign Coordinates
for $file = 1, \ldots, n_f$ do
    → Read file with pixel values $\theta_{ij}$.
    → Save values in matrix, according to pixel position in picture.
    → Assign coordinates to all pixels $P_{ij}$ in initial coordinate system
          $\bar{x}_{ij} = [j-1]\; s + \frac{1}{2}\, s\,,$
          $\bar{y}_{ij} = [i-1]\; s + \frac{1}{2}\, s\,.$
    → Transform into new coordinate system
          $\begin{bmatrix} x_{ij} \\ y_{ij} \end{bmatrix} = \boldsymbol{R} \left[ \begin{bmatrix} \bar{x}_{ij} \\ \bar{y}_{ij} \end{bmatrix} - \boldsymbol{o} \right]\,.$
    → Assign pixel values to points and save in file.
end
```

Algorithm 1: Definition of coordinate system for temperature data.

```
Import experimental data
  → Read all $n_\mathrm{f}$ data files.
  → Save displacements of each point.
  → Save reference coordinates of each point.
  → Save time stamp of each file.
Import mesh
→ Read input file for FEM.
→ Save number of nodes $n_\mathrm{np}$.
→ Save reference coordinates of each node.

Interpolate displacements in space
for $file = 1, \dots, n_f$ do
    → Save current time stamp $t_\mathrm{file}$.
    for $node = 1, \dots, n_{np}$ do
        → Find three closest points for current mesh node in reference configuration.
        → Save reference coordinates $\mathbf{X}$, $\mathbf{Y}$ and displacement at current time $\boldsymbol{u}_1^{t_\mathrm{file}}$, $\boldsymbol{u}_2^{t_\mathrm{file}}$, $\boldsymbol{u}_3^{t_\mathrm{file}}$ of particles.
        → Interpolate displacements linearly onto node position using

            $s = \dfrac{[Y_3 - Y_1]\,[X - X_1] - [X_3 - X_1]\,[Y - Y_1]}{[Y_3 - Y_1]\,[X_2 - X_1] - [X_3 - X_1]\,[Y_2 - Y_1]}$

            $t = \dfrac{[Y_1 - Y_2]\,[X - X_1] + [X_2 - X_1]\,[Y - Y_1]}{[Y_3 - Y_1]\,[X_2 - X_1] - [X_3 - X_1]\,[Y_2 - Y_1]}$

            $\boldsymbol{u}_\mathrm{int}^{t_\mathrm{file}} = [1 - s - t]\ \boldsymbol{u}_1^{t_\mathrm{file}} + s\,\boldsymbol{u}_2^{t_\mathrm{file}} + t\,\boldsymbol{u}_3^{t_\mathrm{file}}\,.$

        → Save experimental displacement for current node.
    end
end

Interpolate displacements in time
for $timestep = 1, \dots, n_{ts}$ do
    → Save current time step $t_\mathrm{sim}$.
    → Find two closest experimental time stamps to current time step.
    → Save time stamps $t_1$, $t_2$ and interpolated displacements $\mathbf{u}_\mathrm{int}^{t_1}$, $\mathbf{u}_\mathrm{int}^{t_2}$.
    → Interpolate displacements linearly onto time step using

        $\mathbf{u}_\mathrm{int}^{t_\mathrm{sim}} = \dfrac{t_2 - t_\mathrm{sim}}{t_2 - t_1}\,\mathbf{u}_\mathrm{int}^{t_1} + \dfrac{t_\mathrm{sim} - t_1}{t_2 - t_1}\,\mathbf{u}_\mathrm{int}^{t_2}$

    → Save experimental displacements for current time step.
end
```

Algorithm 2: Linear interpolation of displacements.

```
Import experimental data
  → Read all $n_\mathrm{f}$ data files.
  → Save temperature of each pixel.
  → Save reference coordinates of each pixel.
  → Save time stamp of each file.
Import mesh
→ Read input file for FEM.
→ Save number of nodes $n_\mathrm{np}$.
→ Save reference coordinates of each node.

Interpolate temperatures
for $timestep = 1, \dots, n_{ts}$ do
    → Save current time stamp $t_\mathrm{sim}$.
    → Find two closest experimental time stamps to current time step.
    → Save time stamps $t_1$, $t_2$ and temperatures $\theta^{t_1}$, $\theta^{t_2}$.
    → Compute temperatures at current time step using
        $\theta^{t_\mathrm{sim}} = \frac{t_2 - t_\mathrm{sim}}{t_2 - t_1}\,\theta^{t_1} + \frac{t_\mathrm{sim} - t_1}{t_2 - t_1}\,\theta^{t_2}$
    → Save experimental temperatures for current time step.
    for $node = 1, \dots, n_{np}$ do
        → Compute expected position of node in current configuration by
            $x^{t_\mathrm{sim}} = X + u^{t_\mathrm{sim}}_\text{int, x}$
            $y^{t_\mathrm{sim}} = Y + u^{t_\mathrm{sim}}_\text{int, y}\,.$
        → Find three closest pixel for node in current configuration.
        → Save spatial coordinates $\mathbf{x}$, $\mathbf{y}$ and temperatures at current time $\theta^{t_\mathrm{sim}}_1$, $\theta^{t_\mathrm{sim}}_2$, $\theta^{t_\mathrm{sim}}_3$ of pixels.
        → Interpolate temperatures linearly onto node position using
            $s = \frac{[y_3 - y_1]\left[x^{t_\mathrm{sim}} - x_1\right] - [x_3 - x_1]\left[y^{t_\mathrm{sim}} - y_1\right]}{[y_3 - y_1][x_2 - x_1] - [x_3 - x_1][y_2 - y_1]}$
            $t = \frac{[y_1 - y_2]\left[x^{t_\mathrm{sim}} - x_1\right] + [x_2 - x_1]\left[y^{t_\mathrm{sim}} - y_1\right]}{[y_3 - y_1][x_2 - x_1] - [x_3 - x_1][y_2 - y_1]}$
            $\theta^{t_\mathrm{sim}}_\mathrm{int} = [1 - s - t]\,\theta^{t_\mathrm{sim}}_1 + s\,\theta^{t_\mathrm{sim}}_2 + t\,\theta^{t_\mathrm{sim}}_3\,.$
        → Save experimental temperature for current node.
    end
end
```

Algorithm 3: Linear interpolation of temperatures.

2.6 Choice of objective function

The FEMU method compares data of simulation and experiment, aiming at a minimisation of differences by minimising the objective function value, as is explained in Section 2.2.1. Thus, the objective function is usually chosen to represent some error measure of the observed physical quantity, e.g. displacements. The exact formulation of an objective function, however, is not unique and can differ with respect to the following characteristics

- error measure,
- considered physical quantities,
- weighting factors,

which are defined subsequently.

2.6.1 Error measure

Although several other suitable error measures may be defined, it is usually the error squared

$$f = \mathbf{r}\left(\boldsymbol{k}\right) \cdot \underline{\underline{W}} \cdot \mathbf{r}\left(\boldsymbol{k}\right) \tag{2.5}$$

which is favoured in literature and which is also chosen as error measure for the objective function within this thesis. Alternatively, for example some norm of the residuum could be used. The residual function $\mathbf{r}$ itself as well as the weighting matrix $\underline{\underline{W}}$ can be specified as follows.

2.6.2 Physical quantities

In principle, all observable as well as derivable quantities can be used to define the residual

$$\mathbf{r}^{(\bullet)} = (\bullet)\left(\boldsymbol{k}\right) - (\bullet)^{\mathrm{exp}} \ , \tag{2.6}$$

which, for the sake of simplicity, is represented as a list holding values of all nodes and all time steps under consideration. Common examples are displacements (observable) or strains (derived from displacements). It was already proposed in [43], that the objective function might be expanded to account for further quantities such as force (or stress), or temperature by simply adding the respective error measures, i.e.

$$f = f^{\mathrm{u}} + f^{\mathrm{F}} + f^{\Theta} + ... = \mathbf{r}^{\mathrm{u}} \cdot \underline{\underline{W}}^{\mathrm{u}} \cdot \mathbf{r}^{\mathrm{u}} + \mathbf{r}^{\mathrm{F}} \cdot \underline{\underline{W}}^{\mathrm{F}} \cdot \mathbf{r}^{\mathrm{F}} + \mathbf{r}^{\Theta} \cdot \underline{\underline{W}}^{\Theta} \cdot \mathbf{r}^{\Theta} + ... \ . \tag{2.7}$$

Displacements - u Displacements can usually be used for the definition of the residual function

$$\mathbf{r}^{\mathrm{u}} = \mathbf{u}\left(\boldsymbol{k}\right) - \mathbf{u}^{\mathrm{exp}} \tag{2.8}$$

without restrictions to the kind of boundary value problem. The experimental set may, however, include rigid body motion of the specimen which can not always be adequately represented in the simulation leading to severely erroneous results, see sections 2.7.2 and 5.3.1.

Strains - ε Strains are intrinsically not affected by rigid body displacements or rigid body rotations, i.e. small rotations for small strain measures and arbitrary rotations for large strain measures. Most DIC systems are able to compute the (technical) strain field on the observed surface, using displacement data of several facets in a certain environment. It is not always clear as to how exactly experimental strains are computed, so that it may be impossible to recreate the procedure with simulated data. Thus, if strains are used within the residual function

$$\mathbf{r}^{\varepsilon} = \boldsymbol{\varepsilon}\left(\boldsymbol{k}\right) - \boldsymbol{\varepsilon}^{\mathrm{exp}} \tag{2.9}$$

to compare experiment and simulation, those strain measures are usually not equivalent. Those who wish to ensure the use of identical strain measures must therefore compute strains for both DIC and simulation data using the same displacement based scheme, as is done e.g. in [27].

Relative displacements - $\Delta\mathbf{u}$ A similar possibility to circumvent the problem of rigid body motions while still ensuring that equal measures are compared within the objective function is the use of relative displacements, i.e.

$$\mathbf{r}^{\Delta\mathrm{u}} = \Delta\mathbf{u}\left(\boldsymbol{k}\right) - \Delta\mathbf{u}^{\mathrm{exp}} \,. \tag{2.10}$$

The underlying idea is the approximation of the same strain-like measure in simulation and experiment. All strain-like quantities are based on the displacement gradient which can be approximated by using the difference in displacements of points. Hence one possibility is to use the difference in displacements $\Delta\mathbf{u}$ of neighbouring FE nodes. This formulation ensures that translational rigid body motions as well as small rotations are completely compensated. One way of specifying these differences $\Delta\mathbf{u}$ is to subtract the displacement component of neighbouring data points from the displacement component of the node under consideration, as is exemplarily shown in Figure 2.12a with

$$\Delta u_{1,\,xx} = u_{1,\,x} - u_{2,\,x} \,, \tag{2.11}$$

$$\Delta u_{1,\,yy} = u_{1,\,y} - u_{3,\,y} \,, \tag{2.12}$$

$$\Delta u_{1,\,xy} = u_{1,\,x} - u_{3,\,x} \,, \tag{2.13}$$

$$\Delta u_{1,\,yx} = u_{1,\,y} - u_{2,\,y} \,. \tag{2.14}$$

This difference can further be divided by the initial distance of the nodes to obtain an approximation of the afore mentioned displacement gradient, while simultaneously reducing the influence of the mesh density on the contribution single nodes make to the overall objective function value. Further manipulations can be used to approximate other, strain-like quantities, e.g. technical strain

$$\Delta u_{1,\,xx} = \frac{u_{1,\,x} - u_{2,\,x}}{\Delta X}\,, \tag{2.15}$$

$$\Delta u_{1,\,yy} = \frac{u_{1,\,y} - u_{3,\,y}}{\Delta Y}\,, \tag{2.16}$$

$$\Delta u_{1,\,xy} = \frac{1}{2}\left[\frac{u_{1,\,x} - u_{3,\,x}}{\Delta Y} + \frac{u_{1,\,y} - u_{2,\,y}}{\Delta X}\right]. \tag{2.17}$$

The significance of the relative displacement component related to the off-diagonal element of the displacement gradient (2.17) greatly depends on the experiment under consideration. It can either be neglected in case no shear strain is expected or must be considered in particular if shear strains are dominant. The effect of choosing relative displacements instead of (unmodified) displacements within the objective function is also examined in Section 5.3.1, Table 5.2 where the different results of both, $\mathbf{u}$ and $\Delta\mathbf{u}$ based, objective function formulations can be seen. It is interesting to note that the observed rigid body motion of a specimen during an experiment may differ significantly for different types of testing machines. Hence, depending on the construction of the used device, the impact of this choice for an objective function may either be pronounced or negligible.

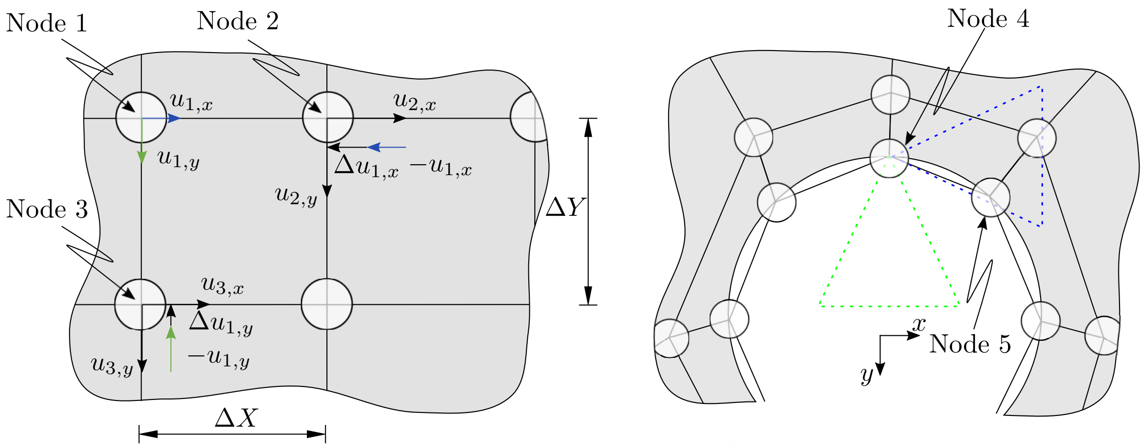

(a) Illustration of a possible definition of $\Delta\mathbf{u}$.

(b) Possible constraints for the definition of a neighbouring node in an unstructured mesh. Neighbouring nodes have to lie within a triangle with predefined dimensions.

Figure 2.12: Neighbouring nodes may be used to generate a relative displacement measure which intrinsically compensates rigid body motions.

Force - F Reaction forces of an experiment are usually integral measures and therefore only have a limited capability if used alone within an objective function. Depending on the applied boundary conditions within the simulation, however, adding the error in reaction forces

$$\mathbf{r}^{\mathrm{F}} = \mathbf{F}\left(\boldsymbol{k}\right) - \mathbf{F}^{\mathrm{exp}} \tag{2.18}$$

to the error of some displacement based measure may speed up the identification process significantly. Prescribing the measured reaction forces as Neumann Boundary Conditions results in a high sensitivity of the displacement related error measures with respect to the model parameter set and, intrinsically, fulfils $\mathbf{r}^{\mathrm{F}} = \mathbf{0}$ rendering the use of forces in the objective function redundant. If only Dirichlet Boundary Conditions are applied, the sensitivity of the displacement field with respect to the model parameter set can be expected to be rather low, since the resulting displacement field can only vary within the applied bounds. For such a case, the value of the reaction force will greatly depend on the current model parameter set and will therefore accelerate the convergence of a parameter identification scheme if considered in the objective function, as was proposed in [43].

Stress - $\boldsymbol{\sigma}$ Stress can never be measured and must be derived from a reaction force by using certain assumptions regarding the homogeneity of stresses. Thus, stress has the same limited capability as forces if used alone within an objective function. A common application for stress-based residual functions

$$\mathbf{r}^{\sigma} = \boldsymbol{\sigma}\left(\boldsymbol{k}\right) - \boldsymbol{\sigma}^{\mathrm{exp}} \tag{2.19}$$

in the objective function is for simple experiments which can be simulated on material point level using a constitutive driver algorithm instead of an FE analysis.

Absolute temperature - $\boldsymbol{\Theta}$ The error in temperature

$$\mathbf{r}^{\Theta} = \boldsymbol{\Theta}\left(\boldsymbol{k}\right) - \boldsymbol{\Theta}^{\mathrm{exp}} \tag{2.20}$$

can be used for the identification of caloric model parameters. It is a suitable measure if the initial temperature distribution of the body under consideration can be applied to the simulation as well. Otherwise, the inhomogeneity must be small in comparison to the overall rise in temperature during the experiment in order to be neglected.

Relative temperature - $\Delta\boldsymbol{\Theta}$ If only small temperature changes are observed and the initial (inhomogeneous) temperature field cannot simply be applied to the simulation, the error of relative temperatures

$$\mathbf{r}^{\Delta\Theta} = \Delta\boldsymbol{\Theta}\left(\boldsymbol{k}\right) - \Delta\boldsymbol{\Theta}^{\mathrm{exp}} \tag{2.21}$$

is still a suitable measure for the identification of caloric model parameters. Each entry of the list $\Delta\boldsymbol{\Theta}$ holds the difference of a material point to the temperature of the same material point at some reference time

$$\Delta\theta = \theta\,(t) - \theta\,(t = t_0)\ , \tag{2.22}$$

$$\Delta\theta^{\mathrm{exp}} = \theta^{\mathrm{exp}}\,(t) - \theta^{\mathrm{exp}}\,(t = t_0)\ , \tag{2.23}$$

which is usually the start of the experiment.

Remark 2.2. The residual function is defined as a vector in this section for purely pragmatical reasons. The alternative representation of the objective function

$$\begin{aligned} f &= f^{\mathrm{u}} + f^{\theta} \\ &= \sum_{i\,\in\,\{x,\,y\}} W_i^{\mathrm{u}} \sum_{t=1}^{n_{\mathrm{ts}}} \sum_{n=1}^{n_{\mathrm{np}}} \left[\Delta u_{ni}^{\mathrm{exp}} - \Delta u_{ni}\,(\boldsymbol{k})\right]_t^2 + W^{\theta} \sum_{t=1}^{n_{\mathrm{ts}}} \sum_{n=1}^{n_{\mathrm{np}}} \left[\Delta\theta_n^{\mathrm{exp}} - \Delta\theta_n(\boldsymbol{k})\right]_t^2 \\ &= \sum_{i\,\in\,\{x,\,y\}} W_i^{\mathrm{u}} \sum_{t=1}^{n_{\mathrm{ts}}} \sum_{n=1}^{n_{\mathrm{np}}} \left[r_{ni}^{\mathrm{u}}(\boldsymbol{k})\right]_t^2 + W^{\theta} \sum_{t=1}^{n_{\mathrm{ts}}} \sum_{n=1}^{n_{\mathrm{np}}} \left[r_n^{\theta}(\boldsymbol{k})\right]_t^2 \end{aligned} \tag{2.24}$$

is closer to the actual implementation, with the number of evaluated time steps n_{ts}, the number of contributing node points n_{np} and the weighting factors W.

2.6.3 Weighting factors

The purpose of the weighting factors is twofold. A clash of units must be prevented, as soon as the errors of different physical quantities are added within the objective function. This is formally done by assigning a suitable unit to each weight, e.g. the inverse unit of the quantity it is paired with, rendering the overall objective function to be consistent or dimensionless. Furthermore, the weighting factors ensure that all addends of the objective function have the desired influence on the objective function value, since error values might range in different orders of magnitude. This should be of little concern for a, theoretically, perfect material model, which precisely represents all characteristics of the real material. For such a model, the global optimum of all error functions should coincide, whether referring to temperature, displacements or any other quantity. For a non-perfect model, however, this is usually not the case. Thus, different model parameter sets may be required to reach, for example, either the global optimum of the error in temperature or the global optimum of the error in displacements. The result of the overall optimisation will, in that example, depend on the choice of the weighting factors, shifting the overall optimum between the two optima of the single error functions along a pareto front also known from multi-objective optimisation. Common choices for weighting factors are a manual selection based on experience as is done in this thesis, or one of the following naturally occurring weighting methods. In [48] the residual is divided by the current experimental value

$$W^{(\bullet)}\ \left[r^{(\bullet)}\right]^2 = \left[\frac{(\bullet)(\boldsymbol{k}) - (\bullet)^{\mathrm{exp}}}{(\bullet)^{\mathrm{exp}}}\right]^2 \qquad \Rightarrow \qquad W^{(\bullet)} = \frac{1}{\left[(\bullet)^{\mathrm{exp}}\right]^2}, \tag{2.25}$$

whereas the maximal experimental value is chosen as a weight in [27] leading to

$$W^{(\bullet)}\ \left[r^{(\bullet)}\right]^2 = \left[\frac{(\bullet)(\boldsymbol{k}) - (\bullet)^{\mathrm{exp}}}{(\bullet)^{\mathrm{exp}}_{\mathrm{max}}}\right]^2 \qquad \Rightarrow \qquad W^{(\bullet)} = \frac{1}{\left[(\bullet)^{\mathrm{exp}}_{\mathrm{max}}\right]^2}\,. \tag{2.26}$$

It is noteworthy that indices relating to the degree of freedom or time step are omitted in the two equations above. A different approach can be found in [70], using available parameters to transform two addends of the objective function to an identical measure (e.g. stress or energy like). In the case of the publication mentioned above, strain and force contribution to the objective function were weighted with Young's modulus and the initial cross section of the utilised dogbone specimen to yield stress-like quantities. Although this specific approach may only work for special cases, it can still be adopted to other pairings within the objective function.

2.6.4 Derivatives

Independent of the precise formulation chosen for the objective function, the Jacobian and the Hessian of this function are required not only for gradient based optimisation schemes, but also for the analysis of common identifiability criteria, see Section 2.8. Since the objective function was defined above with respect to to different quantities, weighting factors and notations, the following, more general expression

$$f = \sum_{t=1}^{n_{\mathrm{ts}}} \sum_{n=1}^{n_{\mathrm{d}}} W_n \left[r_n\right]_t^2 = \sum_{t=1}^{n_{\mathrm{ts}}} \sum_{n=1}^{n_{\mathrm{d}}} \left[r_n^{\mathrm{W}}\right]_t^2 \qquad \text{with} \ \ r_n^{\mathrm{W}}\big|_t = \sqrt{W_n}\ r_n\big|_t \tag{2.27}$$

is used for the introduction of the derivatives. In Equation (2.27), different kind of physical quantities (e.g. temperature, displacement in x- and displacements in y-direction of all n_{np} nodes considered) are incorporated in the number of all data points n_{d}, the weighted squared error r^{W} of which is summed over all time steps n_{ts}. The first derivative with respect to the model parameters yields the gradient or the Jacobian of the objective function

$$\boldsymbol{J}^{\mathrm{f}} = 2 \sum_{t=1}^{n_{\mathrm{ts}}} \sum_{n=1}^{n_{\mathrm{d}}} W_n \left[r_n\, \boldsymbol{J}^{\mathrm{r}}_n\right]_t\,, \tag{2.28}$$

making use of the Jacobian of the residual function r evaluated for the current time step and data point

$$\boldsymbol{J}^{\mathrm{r}}_n\big|_t = \left.\frac{\mathrm{d}r_n}{\mathrm{d}\boldsymbol{k}}\right|_t = \left.\frac{\mathrm{d}\left[(\bullet)_n(\boldsymbol{k}) - (\bullet)_n^{\mathrm{exp}}\right]}{\mathrm{d}\boldsymbol{k}}\right|_t = \left.\frac{\mathrm{d}\left[(\bullet)_n(\boldsymbol{k})\right]}{\mathrm{d}\boldsymbol{k}}\right|_t\,. \tag{2.29}$$

Regarding the Hessian of the objective function

$$\boldsymbol{H}^{\mathrm{f}} = 2 \sum_{t=1}^{n_{\mathrm{ts}}} \sum_{n=1}^{n_{\mathrm{d}}} W_n \, [\boldsymbol{J}^{\mathrm{r}}_n \otimes \boldsymbol{J}^{\mathrm{r}}_n + r_n \, \boldsymbol{H}^{\mathrm{r}}_n \,]_t \qquad \text{with} \;\; \boldsymbol{H}^{\mathrm{r}}_n|_t = \left. \frac{\mathrm{d}^2(\bullet)_n}{\mathrm{d}\boldsymbol{k}^2} \right|_t , \tag{2.30}$$

the second addend holding the Hessian of the residual function $\boldsymbol{H}^{\mathrm{r}}_n|_t$ is usually neglected, leading to

$$\boldsymbol{H}^{\mathrm{f}}_{\mathrm{lin}} = 2 \sum_{t=1}^{n_{\mathrm{ts}}} \sum_{n=1}^{n_{\mathrm{d}}} W_n \, [\boldsymbol{J}^{\mathrm{r}}_n \otimes \boldsymbol{J}^{\mathrm{r}}_n \,]_t \; . \tag{2.31}$$

This approximation is only valid if the omitted addend is significantly smaller than the first one, which is certainly true if the residual function r is linear in the model parameters $\boldsymbol{k}$, but cannot be guaranteed in general. It is worth mentioning that the approximated Hessian $\boldsymbol{H}^{\mathrm{f}}_{\mathrm{lin}}$ does not depend on experimental data, as long as the weighting factors W are independent of experimental data, cf. Equations (2.29) and (2.26). It can furthermore be rewritten in index notation as

$$\begin{aligned} \left[H^{\mathrm{f}}_{\mathrm{lin}}\right]_{ij} = \; 2 \sum_{t=1}^{n_{\mathrm{ts}}} \sum_{n=1}^{n_{\mathrm{d}}} W_n \; [J^{\mathrm{r}}_n|_t]_i \; [J^{\mathrm{r}}_n|_t]_j \; &= 2 \, \mathbf{J}^{\mathrm{Wr}}_i \cdot \mathbf{J}^{\mathrm{Wr}}_j \\ &\overset{(W_n = W)}{=} 2 \, W \, \mathbf{J}^{\mathrm{r}}_i \cdot \mathbf{J}^{\mathrm{r}}_j \, , \end{aligned} \tag{2.32}$$

with the vector of weighted residual sensitivities

$$\mathbf{J}^{\mathrm{Wr}}_i = \begin{bmatrix} \sqrt{W_{n=1}} \; \left.\frac{\mathrm{d}[(\bullet)_{n=1}]}{\mathrm{d}k_i}\right|_{t=1} \\ \sqrt{W_{n=2}} \; \left.\frac{\mathrm{d}[(\bullet)_{n=2}]}{\mathrm{d}k_i}\right|_{t=1} \\ \dots \\ \sqrt{W_{n=n_{\mathrm{d}}}} \; \left.\frac{\mathrm{d}\big[(\bullet)_{n=n_{\mathrm{d}}}\big]}{\mathrm{d}k_i}\right|_{t=1} \\ \sqrt{W_{n=1}} \; \left.\frac{\mathrm{d}[(\bullet)_{n=1}]}{\mathrm{d}k_i}\right|_{t=2} \\ \dots \\ \sqrt{W_{n=n_{\mathrm{d}}}} \; \left.\frac{\mathrm{d}\big[(\bullet)_{n=n_{\mathrm{d}}}\big]}{\mathrm{d}k_i}\right|_{t=n_{\mathrm{ts}}} \end{bmatrix} \overset{(W_n = W)}{=} \sqrt{W} \, \mathbf{J}^{\mathrm{r}}_i = \sqrt{W} \begin{bmatrix} \left.\frac{\mathrm{d}[(\bullet)_{n=1}]}{\mathrm{d}k_i}\right|_{t=1} \\ \left.\frac{\mathrm{d}[(\bullet)_{n=2}]}{\mathrm{d}k_i}\right|_{t=1} \\ \dots \\ \left.\frac{\mathrm{d}\big[(\bullet)_{n=n_{\mathrm{d}}}\big]}{\mathrm{d}k_i}\right|_{t=1} \\ \left.\frac{\mathrm{d}[(\bullet)_{n=1}]}{\mathrm{d}k_i}\right|_{t=2} \\ \dots \\ \left.\frac{\mathrm{d}\big[(\bullet)_{n=n_{\mathrm{d}}}\big]}{\mathrm{d}k_i}\right|_{t=n_{\mathrm{ts}}} \end{bmatrix} , \tag{2.33}$$

which will be used for the definition of correlation measures in Section 2.8. The weighted residual sensitivity in Equations (2.32) and (2.33) can only be reduced to the vector of (unweighted) residual sensitivities $\mathbf{J}^{\mathrm{r}}$ if the weighting factors are identical for all entries.

Remark 2.3. The definition of the actual response sensitivities $\frac{\mathrm{d}(\bullet)}{\mathrm{d}\boldsymbol{k}}$ depends on the chosen constitutive model and on the framework used (e.g. FE-Method or constitutive driver algorithm). Such an extensive derivation is out of scope for the thesis at hand, but can for example be found in [46] and [47].

Remark 2.4. It was already mentioned that the use of the approximated Hessian of the objective function $\boldsymbol{H}^{\mathrm{f}}_{\mathrm{lin}}$ is usually associated with the assumption that the second addend in Equation (2.30) is significantly smaller than the first part. This assumption can, unfortunately, not be examined without computing the neglected addend, generating a conflict between making the assumption in order to avoid derivational and implementational effort and the necessity to prove the validity of the assumption. Alternatively, the absolute value of the residuum $r \ll 1$ close to the optimum is typically considered in order to discard the second addend. The value of the residuum, however, can simply be scaled, e.g. by changing the underlying system of units, and is therefore difficult (maybe even impossible) to interpret.

2.7 Sources of errors

Like all other numerical and experimental schemes, the parameter identification is prone to several kinds of errors. A careful handling of the respective sources of each error can minimise the impact on the solution. Hence, several of the most commonly encountered errors are listed below.

2.7.1 Measurement errors

According to [1], measurement errors can be divided into two groups, i.e. random errors and systematic errors. Random errors can, per definition, not be controlled and include e.g. the so-called uncertainties such as noises and scattering. Both are usually treated by considering a statistically relevant amount of data, rather than just the set of a single experiment. Systematic errors, on the other hand, refer to reproducible effects like the wrong calibration or ignoring the warm-up phase of a measuring device. Those errors can either or not be correctable by means of a post measurement calculation. The specific random and systematic errors that can occur during the experiments considered in this thesis are commented on in Sections 2.3 and 2.4.

2.7.2 Experimental errors

Some experimental errors are inevitable but most of the severe ones can be avoided or compensated. One source is the clamping of the specimen. An unaligned specimen can lead to bending during the experiment, falsifying the results if the effect becomes too pronounced. Furthermore, the specimen is usually subject to rigid body motion since no machine is perfectly stiff. In some cases the superimposed displacement can be corrected if the machine stiffness is known. Depending on the structure of the employed machine, however, the stiffness may not be a constant function of the force due to settling and slipping of some components. This requires a more sophisticated handling, for example

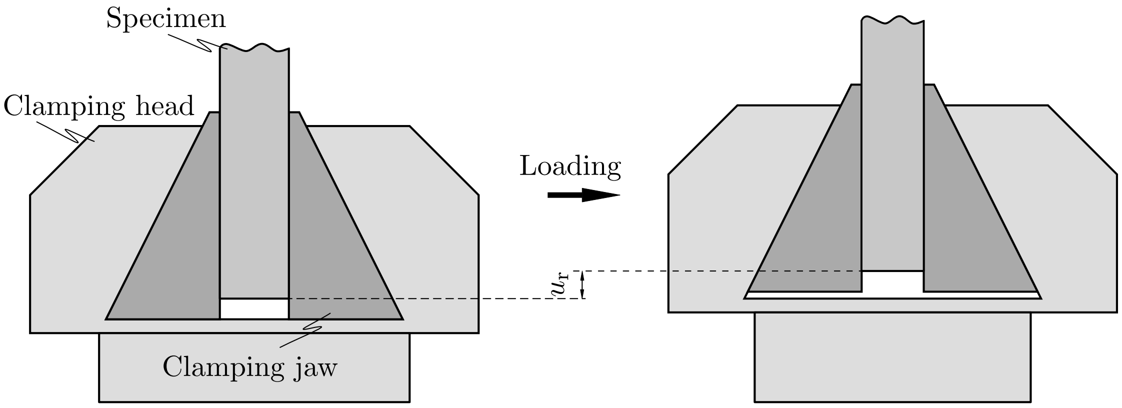

Figure 2.13: Superimposed rigid body motion u_r of the specimen due to elongation of the testing machine and slip of some components.

by a carefully chosen objective function which intrinsically compensates rigid body motions, c.f. Section 2.6.

Another source of experimental errors lies in the so-called incompleteness of data. It refers to information which is unavailable either because it was not part of the time and space-discrete measurement or because some material effect is not even featured in the experiments, see for example Figure 2.14. Applying an appropriately high sampling rate and facet density, the first aspect can usually be avoided by means of appropriate measuring devices, i.e. with a suitable resolution and frame rate. Regarding the second aspect of incompleteness, information which is not represented by the experiments at hand, the effect of all model parameters must be well understood in order to chose experiments which actually allow an identification. Unfortunately, a unique interpretation of model parameters may not always be possible, at least not in a straightforward manner. For such cases several alternative possibilities to check the identifiability of model parameters exist, as is explained in Section 2.8.

2.7.3 Modelling errors

Apart from experimental data, the inverse problem requires further input (boundary conditions, constitutive model and geometry, see Figure 2.1b) to define a suitable Boundary Value Problem (BVP). All of these modelling aspects can be subject to more or less obvious modelling errors which, in turn, affect the result of the inverse problem.

Assuming that the geometry is approximated with Finite Elements, elements (cubic or tetrahedral elements, linear or higher order shape functions, etc.), as well as the mesh density should be chosen accordingly to ensure mesh independence, i.e. further refinement should not alter the outcome of the direct, nor of the inverse problem (if the exact same points contribute to the objective function).

Boundary conditions must represent the experiment considered and often rely on measured data (e.g. force or displacement). The experiment is matched as precisely as

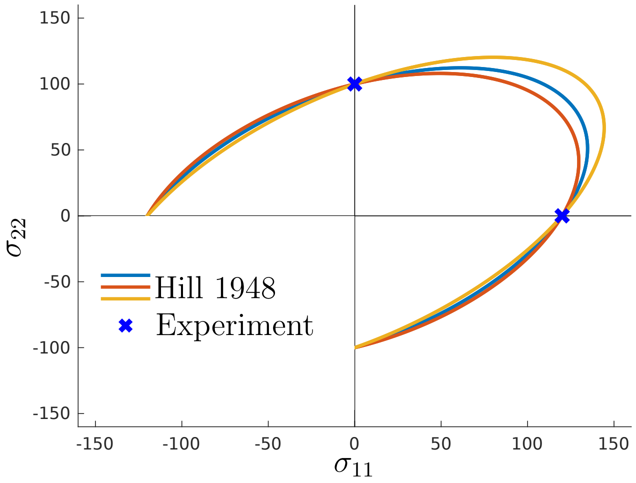

Figure 2.14: Visualisation of incompleteness. Too little information is available to fit the orthotropic yield surface (Hill48) to the experimental data.

possible if measured or otherwise known data can be prescribed at all bounds of the body under consideration. If this is not possible (e.g. with respect to temperature or heat flux), further assumptions must be made, and the solution of the inverse problem depends on the quality of these assumptions as can exemplarily be seen in Section 5.5. One further source of modelling errors lies in the constitutive model which introduces the actual model parameters. Most constitutive models rely, at some point, on a phenomenological description of physical processes and may therefore not be able to represent all aspects of a material equally well. Even in a theoretical scenario without measurement and experimental errors, a certain model may not fit the experimental data points perfectly, as is exemplarily illustrated by fitting two different orthotropic yield surfaces to a specific dataset in Figure 2.15. The constitutive model should therefore be chosen carefully and usually requires experience or trial and error testing of different formulations until remaining model errors are within acceptable bounds. It is worth keeping in mind that the existence of a perfect phenomenological model which reduces the modelling error to zero for an arbitrary set of experimental data is not guaranteed.

2.8 Identifiability and correlation

It was already mentioned in Section 2.7 that an interpretation of all model parameters may not always be possible, especially for complex constitutive models with many model parameters. For those models, two effects which lead to infinitely many solutions of the inverse problems may not be noticed by means of the constitutive equations alone. Those effects are incompleteness of data and dependency of model parameters. Identifiability can therefore be related to the model specific property of overparametrisation as well as to the experiment specific property of addressing all

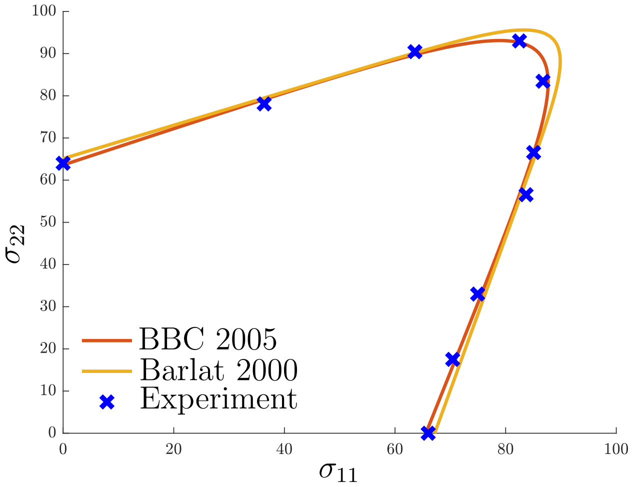

Figure 2.15: Illustration of modelling error which can depend on specific model formulation. None of the formulations fit perfectly. Although it could be said that the remaining error between the exemplary experimental data and the BBC model is merely due to experimental and measurement errors, the Barlat model clearly inhibits some model-specific remaining error.

model parameters (sufficiently strong). Thus, some sort of measure for the identifiability of model parameters on the basis of a given set of experimental data is required. In fact, several measures and schemes exist which can detect whether or not the experimental data holds sufficient information for the identification of the targeted model parameters and whether the model holds only independent model parameters.

Before presenting the most commonly used methods, three more aspects are worth mentioning. Firstly, the measures shown in this section can, at best, guarantee local uniqueness in the sense of a local optimum at one (isolated) point, as opposed to a valley of solutions. The existence of further local minima outside a certain trust area is still possible. Secondly, the difference between correlation and dependency of parameters as used within this thesis should be defined, since some authors tend to use these expressions as synonyms. Here, the dependency of parameters implies an overparametrisation of the model, so that two or more parameters are connected by means of some function which can be linear or non-linear. In contrast thereto, correlation describes the tendency of a random variable (e.g. a model parameter) to increase or decrease with some further random variable, c.f. [13] Section 3.5. Two correlated parameters are therefore not necessarily dependent. Only perfect correlation, as defined later within this section, implies a dependency of parameters, see [67] Section 4.4. Thirdly, the correlation measures below provide no information as to whether two parameters are dependent due to incomplete experimental data (e.g. isotropic and kinematic hardening applied to monotonous loading), or as to whether the model holds some intrinsically dependant parameters.

2.8.1 Correlation based on residual sensitivity

The question of identifiability for a certain model parameter can be related to the question whether this parameter has sufficient impact on the model solution (i.e. the response) for a specific experiment. Thus, the analysis of response sensitivities was proposed in [69] and [24] as a means to choose experiments which activate, i.e. are sensitive enough with respect to all parameters sought for. This (graphical) concept, however, tends to increase in complexity with the number of model parameters. A simplified measure lies in the analysis of the collinearity of the vector of response sensitivities via the correlation measure

$$C^{\mathrm{S}}_{ij} = \frac{\mathbf{J}^{\mathrm{Wr}}_i \cdot \mathbf{J}^{\mathrm{Wr}}_j}{\|\mathbf{J}^{\mathrm{Wr}}_i\| \, \|\mathbf{J}^{\mathrm{Wr}}_j\|} \overset{(W_n = W)}{=} \frac{\mathbf{J}^{\mathrm{r}}_i \cdot \mathbf{J}^{\mathrm{r}}_j}{\|\mathbf{J}^{\mathrm{r}}_i\| \, \|\mathbf{J}^{\mathrm{r}}_j\|} \,, \tag{2.34}$$

as proposed in [21] and applied in [35]. It is worth noting, that the correlation matrix is introduced in [21] by using the response sensitivities (equal to residual sensitivities $\mathbf{J}^{\mathrm{r}}$ as defined in Equation (2.29)) and constant weights W. The definition in Equation (2.34) using the weighted residual sensitivities $\mathbf{J}^{\mathrm{Wr}}$ is more general, taking into account different weights, see Appendix A for a short example on the importance of weights within this measure. Entries of this correlation matrix take values between $-1 < C^{\mathrm{S}}_{ij} < 1$, whereas $\|C^{\mathrm{S}}_{ij}\| = 1$ indicates perfect collinearity, i.e. perfect correlation and therefore dependency of the parameters k_i and k_j. Should one parameter not contribute to the considered material response, the norm of the associated weighted residual sensitivity vanishes rendering the entries related to such a parameter not defined. Comparing Equations (2.34) and (2.32), the correlation matrix can be computed by using the approximated Hessian of the objective function

$$C^{\mathrm{S}}_{ij} = \frac{\left[\boldsymbol{H}^{\mathrm{f}}_{\mathrm{lin}}\right]_{ij}}{\sqrt{\left[\boldsymbol{H}^{\mathrm{f}}_{\mathrm{lin}}\right]_{ii} \left[\boldsymbol{H}^{\mathrm{f}}_{\mathrm{lin}}\right]_{jj}}} \,. \tag{2.35}$$

Although the entries of the correlation matrix $\boldsymbol{C}^{\mathrm{S}}$ are simple to compute once the approximated Hessian is available, entries other than zero, one (or not defined) are difficult to interpret. Furthermore, the matrix holds no information regarding the extend of influence which a parameter has on a certain experiment, i.e. the predicted response.

2.8.2 Correlation based on covariance

Another correlation measure widely used is based on the so-called covariance matrix which stems from the field of statistical analysis, see e.g. [14], [4], [26] and [27]. Whereas the previous correlation measure indicates the tendency of the material response to change with the model parameters, the covariance matrix indicates the (statistical) tendency of the model parameters themselves to change in dependency of each other, see [13] Section 3.5. The entries of the covariance matrix for the model parameters

$$P^{\boldsymbol{k}}_{ij} = \sigma^2 \left[{\boldsymbol{H}^{\mathrm{f}}_{\mathrm{lin}}}^{-1} \right]_{ij} . \tag{2.36}$$

can be computed using the variance σ^2 of the weighted residuals and the (pseudo-) inverse of the approximated Hessian $\boldsymbol{H}^{\mathrm{f}}_{\mathrm{lin}}$. The associated correlation measure is defined as

$$C^{\mathrm{P}}_{ij} = \frac{P^{\boldsymbol{k}}_{ij}}{\sqrt{P^{\boldsymbol{k}}_{ii}\, P^{\boldsymbol{k}}_{jj}}} = \frac{\left[{\boldsymbol{H}^{\mathrm{f}}_{\mathrm{lin}}}^{-1} \right]_{ij}}{\sqrt{\left[{\boldsymbol{H}^{\mathrm{f}}_{\mathrm{lin}}}^{-1} \right]_{ii} \left[{\boldsymbol{H}^{\mathrm{f}}_{\mathrm{lin}}}^{-1} \right]_{jj}}} . \tag{2.37}$$

Although the variance of the weighted residuals is not required for the computation of the model parameter correlation, using the empirical variance

$$\begin{aligned} s^2 &= \frac{1}{n_{\mathrm{dof}}} \sum_{i=1}^{n_{\mathrm{tot}}} r^{\mathrm{W}}_i \, r^{\mathrm{W}}_i = \frac{1}{n_{\mathrm{dof}}} \sum_{t=1}^{n_{\mathrm{ts}}} \sum_{n=1}^{n_{\mathrm{d}}} r^{\mathrm{W}}_n\big|_t \, r^{\mathrm{W}}_n\big|_t \\ &= \frac{\mathbf{r}^{\mathrm{W}} \cdot \mathbf{r}^{\mathrm{W}}}{n_{\mathrm{dof}}} \\ &\approx \sigma^2 \end{aligned} \tag{2.38}$$

with the total amount of data points $n_{\mathrm{tot}} = n_{\mathrm{ts}}\, n_{\mathrm{d}}$, the statistical degrees of freedom $n_{\mathrm{dof}} = n_{\mathrm{tot}} - n_{\mathrm{p}}$ and the number of model parameters n_{p} allows the specification of the confidence interval for each model parameter

$$\mathrm{konv}\,(k_i) = \left[k^*_i - \sqrt{P_{ii}},\, k^*_i + \sqrt{P_{ii}} \right] \tag{2.39}$$

around the identified optimal values $\boldsymbol{k}^*$ since the covariance matrix intrinsically holds the variance, and therefore also the standard deviation of each parameter on its main diagonal, cf. [13] and [37].

Analogous to the last correlation measure, the coefficients of this correlation matrix take values between $-1 < C^{\mathrm{P}}_{ij} < 1$, whereas $\|C^{\mathrm{P}}_{ij}\| = 1$ indicates perfect correlation and therefore dependency of the parameters k_i and k_j.

It is worth noting that Equations (2.36) and (2.38) are subject to several assumptions which can be found in Appendix B.

2.8.3 Identifiability based on Hessian

One further method to check the identifiability of model parameters lies in the direct analysis of the Hessian $\boldsymbol{H}^{\mathrm{f}}$ or its approximation $\boldsymbol{H}^{\mathrm{f}}_{\mathrm{lin}}$ at the solution point $\boldsymbol{k}^*$. It is well known that a positive definite Hessian with only positive eigenvalues $\lambda_i^{\mathrm{Hf}} > 0$ indicates an isolated minimum at $\boldsymbol{k}^*$, see Figure 2.16a. If one or more eigenvalues are equal to zero, i.e. $\lambda_i^{\mathrm{Hf}} \geq 0$, the Hessian is positive semi-definite which, according to [7], can indicate a dependency between one or more parameters. In such a case multiple solutions lie next to each other, thereby forming a valley of possible solutions to the inverse problem as is shown in Figures 2.16b and 2.16c. The reasoning behind this method is, that the gradient does not change along the direction of the eigenvector $\boldsymbol{\Phi}_i^{\mathrm{Hf}}$ associated with the zero eigenvalue which is obviously true along the valley of solutions where the gradient is zero at all points independent of the type of parameter relation (i.e. linear or non-linear). It is interesting to note that the approximated Hessian $\boldsymbol{H}^{\mathrm{f}}_{\mathrm{lin}}$ may detect linear and non-linear dependencies at arbitrary points in parameter space as is further elaborated in Appendix C. Thus, checking the approximated Hessian can reveal parameter dependencies a priori. Furthermore, the associated eigenvector points in the direction of the iso-line, therefore revealing the linearised relation of the two parameters at the evaluated point, see Appendix C for an example. It should be mentioned that this method is similar to checking the sufficient condition by using the second derivative test which is considered inconclusive in the case of a semi-definite Hessian. Thus, a point along a valley of solutions will always have a singular Hessian, but not all singular Hessians are due to intrinsic parameter dependencies which is an important issue to keep in mind.

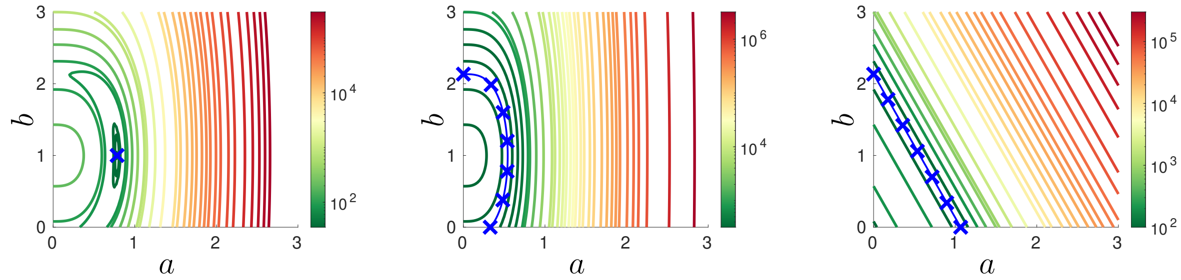

(a) Function with isolated minimum.

(b) Function with valley of solutions. Parameters have a non-linear dependency.

(c) Function with valley of solutions. Parameters have a linear dependency.

Figure 2.16: Contour plots of exemplary functions with model parameters a and b. Minima are marked by X.

2.8.4 Identifiability based on grid search

So far, the measures and methods above all rely on the availability of the response sensitivity. A grid search may therefore be a suitable alternative in case an analytical expression for the response sensitivity is not at hand. Starting from sufficiently many initial guesses which are scattered evenly across parameter space, three cases can usually be distinguished

- Different starting points reach different optima $\boldsymbol{k}^*_A$, $\boldsymbol{k}^*_B$,..., with different objective function values f^*_A, f^*_B, ...
  This case indicates different, but isolated minima within the area in parameter space considered.

- Different starting points reach different optima $\boldsymbol{k}^*_A$, $\boldsymbol{k}^*_B$,..., with numerically identical objective function values $f^*_A = f^*_B = ...$
  A dependency of some model parameters is likely, since the objective function values at different optima coincide. If the obtained material response is also identical, it further underlines the possibility of a parameter dependency.

- All starting points converge towards the same optimal parameter set.
  This case suggests that no further minima are present within a certain area in parameter space. The problem therefore appears to have an isolated minimum, whereas further minima could still exist outside the area in parameter space considered.

Although this method may not be equivalent to a mathematical proof, it can nevertheless give a sufficiently good impression of the situation at hand, depending on the number of initial guesses used. From the methods presented within this section this one is furthermore the only one to detect further local minima, which comes, however, at the drawback of high computational costs for the evaluation of several inverse problems.

Remark 2.5. Additional measures for the correlation of parameters exist and can be found in literature, see e.g. [14], [4], [72].

2.9 Verification and validation

A vital part of every identification process, the result of which is to be used for predictive simulations, is the verification and validation of the obtained parameter set. Accordingly, these two concepts are explained at first, underlining especially the importance of a validation. Finally, the case of model dependent results is discussed.

2.9.1 Verification

To verify the solution of the inverse problem, the material response of the chosen model with the obtained model parameters is compared against the experimental data which was used for the identification process. The solution is verified if the model prediction fits the experimental data well. A failed verification can e.g. be due to local minima of the objective function, see Figure 2.17a, or to the model's general inability to fit the observed material behaviour, see Figures 2.17b and 2.17c.

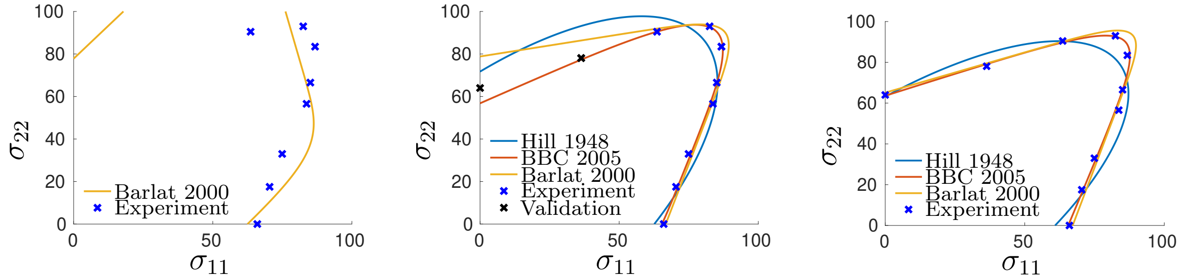

(a) Local minimum in objective function leads to solution which fails the verification.

(b) The Barlat and the BBC model both pass the verification, but only the solution of the BBC model also passes the validation attempt. The Hill model fails both the verification and the validation.

(c) Using all available data for the identification process may lead to better (i.e. verifiable) results for some models, but no further statements about the validity of the model can be made.

Figure 2.17: Fit of three yield surface formulation to exemplary experimental data. All plotted states represent the converged solution and therefore a (local) minimiser to the associated inverse problem.

2.9.2 Validation

Whereas verification checks the ability of the model at the solution point to represent the data which was used for the fit in the first place, validation aims at the general capability of the model to predict the response of the material under consideration. This is done by comparing experimental data which was not part of the identification process to the predicted material response using the obtained, optimal parameter set, see Figure 2.17b. Depending on the number and type of additional experiments, the significance of the validation can be more or less pronounced. For example, Figure 2.17b shows a successful validation of the BBC model. This does, however, not imply how well the model predicts states with compressive stresses and does therefore not guarantee a general applicability of the obtained parameter set to arbitrary boundary value problems. It is worth noting that a failed validation does not necessarily render the whole model inadequate. Adding further data to the identification process may sometimes significantly improve the validity of the obtained parameter set, compare for example the fit of the Barlat model in Figures 2.17b and 2.17c.

2.9.3 Model dependency

With the difference between verification and validation being defined, let only models which adequately predict all possible material responses of a certain material for a specific range of strain, temperature and strain rate be called *material* model of this material and let the associated parameter set be the *material* parameters for this couple of model and material. Thus, only parameter sets which pass both, verification and validation, can be considered true material parameters of a specific model for a certain material (in a defined range of strain, temperature and strain rate). In contrast thereto, the optimal parameter set of a model which does not represent a certain material adequately will usually differ for different boundary value problems. Those parameter sets, albeit optimal, can therefore not be considered material parameters since they do not only depend on the material but also on the boundary value problem under consideration. For the same reason, the model should not be called a material model for this material. In summation, a tuple of material, model and parameter set should always be considered and thoroughly validated before deciding whether or not model and parameter set can be called *material* model and *material* parameters respectively. A parameter identification does therefore not necessarily compute the, say, true material parameters but rather determines the optimal parameters for the provided input, as was already implied in Section 2.2.

3 Experimental setup

This chapter provides information on the experiments which are used during the parameter identification, starting with the description of the testing and measurement devices utilised. Afterwards, the employed specimens are presented as well as the experimental setup. Finally, a graphical representation of the obtained experimental data is shown and analysed with regards to the requirements of a suitable constitutive model.

3.1 Testing equipment and measurement devices

The identification of a model parameter set for a thermo-mechanically coupled constitutive model requires information about the mechanical and the thermal field. Hence, a DIC system is used along with a thermography system to capture the displacement field as well as the temperature field during the experiments. The load is applied by means of an electro-mechanical tension machine which can be seen in Figure 3.1 together with the measurement systems.

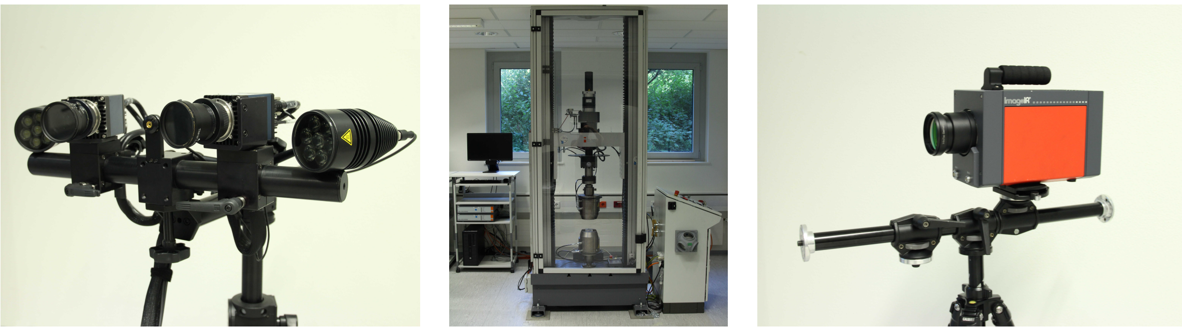

(a) Aramis system from GOM.

(b) Electro-mechanical tension and torsion machine from Walter&Bai.

(c) Thermography system ImageIR 8320hp from InfraTec.

Figure 3.1: Experimental equipment.

Electro magnetic tension and torsion machine All experiments are performed on a LFM 100-T200 from Walter&Bai with a nominal load of 100 kN tension and 200 Nm torsion respectively. This system is equipped with a high resolution, two channel digital control and regulation unit of type PCS 8000-T2. Due to the spindle drive, only quasi static experiments with low accelerations can be realised. It is worth noting that the clamping jaws tend to slip within the grip heads, so that the overall machine stiffness cannot be expressed by a function of the force alone.

Digital image correlation system In order to gain information about the experimental displacement field, an Aramis-System from GOM was used, see Figure 3.1a. Each of the two cameras has a resolution of 2358x1728 pixels and is equipped with a 50 mm lens. The system can be connected to the tension and torsion testing machine allowing for a synchronisation, as well as the transmission of data.

Thermography system The temperature field is observed by means of the high speed thermography system ImageIR 8320hp from InfraTEC. It captures electromagnetic waves with a length of between 2.0 and 5.7 μm and is equipped with a 50 mm high-precision telephoto lens. The spatial resolution of the camera is 640x512 pixels with an accuracy of +/-1 °C or +/- 1 %. Analogous to the Aramis system, the ImageIR can also be coupled to the tension and torsion testing machine in order to synchronise the start of the devices.

3.2 Specimens

All tests are carried out by using the same type of specimen made from the aluminium alloy AW6016. The chosen geometry is based on recommendations found in DIN 50125 and can be seen in Figure 3.2. The specimens are water-cut from sheet metal plates with an angle of 0, 45 and 90 degrees with respect to the rolling direction. Within this thesis, however, only those specimens aligned with the rolling direction (angle of zero degrees) are used for the identification process.

3.3 Experimental setup

The general setup of the different devices is depicted in Figure 3.3. Each experiment is displacement controlled by the regulation unit of the tension system and synchronised by means of a trigger signal sent to the measurement units, indicating the start of an experiment. Since the force signal is also sent to the DIC system, all mechanical data is available on the Aramis system, whereas all temperature data is saved on the thermography system. A glass plate is positioned between the specimen and DIC system to reduce the thermal influence of the heated DIC lights, see Section 2.4. The thermography system, however, is placed on the opposite sides of the specimen, due to the wavelength spectrum detected by the system at hand. The emission coefficient is usually a function of the wavelength and significantly differs for most paints in the range between 2.0 and

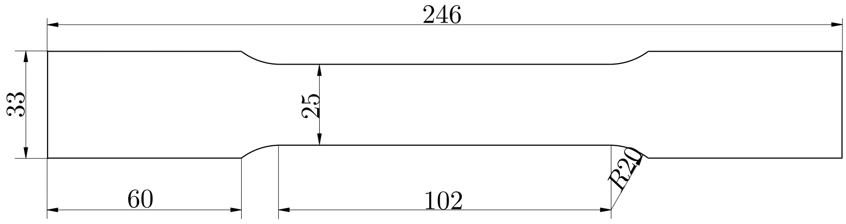

(a) Technical drawing — top view.

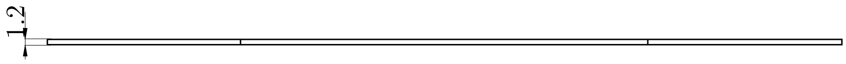

(b) Technical drawing — front view.

(c) Stochastic pattern for DIC system on topside of specimen.

(d) Black paint for thermography system on backside of specimen.

Figure 3.2: Dogbone specimen for tensile testing.

5.7 μm. Hence, it is not possible to compute the correct temperature of the speckled surface since the appropriate emission coefficient for each pixel is unknown, see Section 2.4. For this reason the thermography system is positioned to observe a different side of the specimen onto which paint with a known emission coefficient is applied, see Figure 3.2. The thermography system is started roughly two hours before the first measurement is performed to allow the camera, which is actively and internally cooled, to reach a steady temperature state for the sake of higher accuracy. The interested reader can find further useful instructions on the handling of thermography systems in [65].

3.4 Experimental data

With this setup, several specimens are tested with a constant crosshead speed of 0.14 mm/s. At first, some specimens are used to analyse the material response with respect to anisotropy and breaking strain. Although full field measurements are made and used for the identification later on, local quantities (stress, strain and temperature of a single point) are shown in the following, since the evolution of a local quantity can be visualised and interpreted straightforwardly.
Regarding the experimental stress strain relation, it can be computed on the basis of the obtained displacement field and force signal. Assuming a homogeneous distribution of

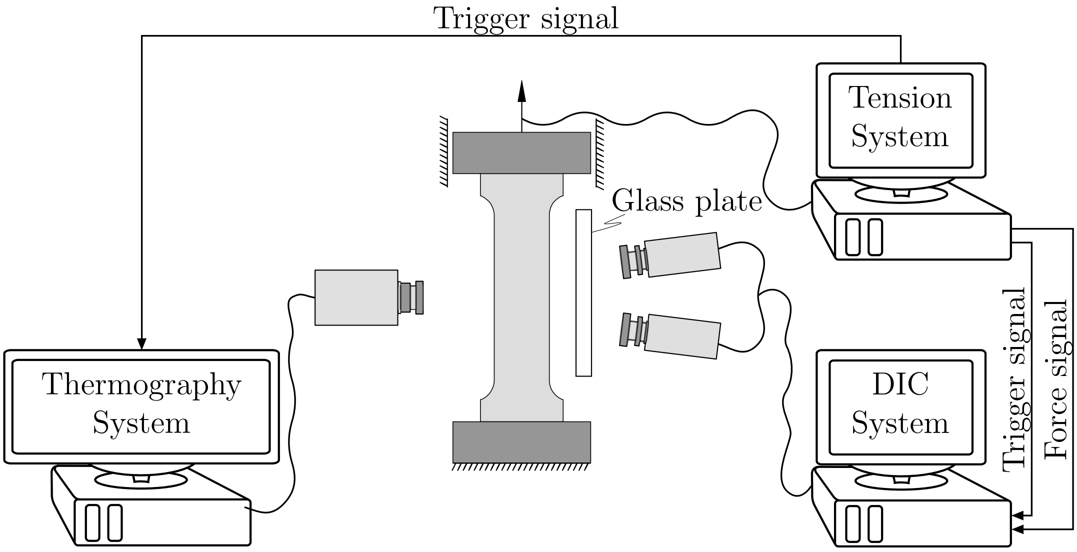

Figure 3.3: Setup of the tension test.

stress and strain within the area of interest, the associated component of the Piola stress tensor and of the deformation gradient in tensile direction, $P_{\|}$ and $F_{\|}$ respectively, allow a direct visualisation and interpretation of the experimental data. Figure 3.4a shows the obtained relation of both quantities until rupture and for different rolling directions. The tensile strength of the material is reached at a stretch of approximately 1.23 and the specimens rupture after reaching a stretch greater than 1.3.

As already mentioned in the introduction, this thesis mainly deals with proofs of concept and less with the precise identification of model parameters for predictive simulations. Thus only three further experiments are performed and Table 3.1 shows which experiment is used for which identification in Chapter 5. It is worth noting that these experiments feature a maximal stretch of $F_{\|} \approx 1.16$, see Figure 3.4b, thereby avoiding the onset of rupture and hence a strong influence of damage and material failure. The temperature of the centre point of the specimens (marked by $+$ in Figure 3.6) over time is given in Figure 3.5, together with the components in tensile direction of stress and

Table 3.1: Experiments and constitutive models used within this thesis.

Exp. No.	Description	Proof of concept	Mat. Mod.	Sec.
1	Monotonous loading Without cooling down	Identifiability of thermal model parameters	1	5.3
2	Loading and unloading With cooling down	Model dependency	1 & 2	5.4
3	Loading and unloading With cooling down	Identifiability of thermal boundary coefficients	2	5.5

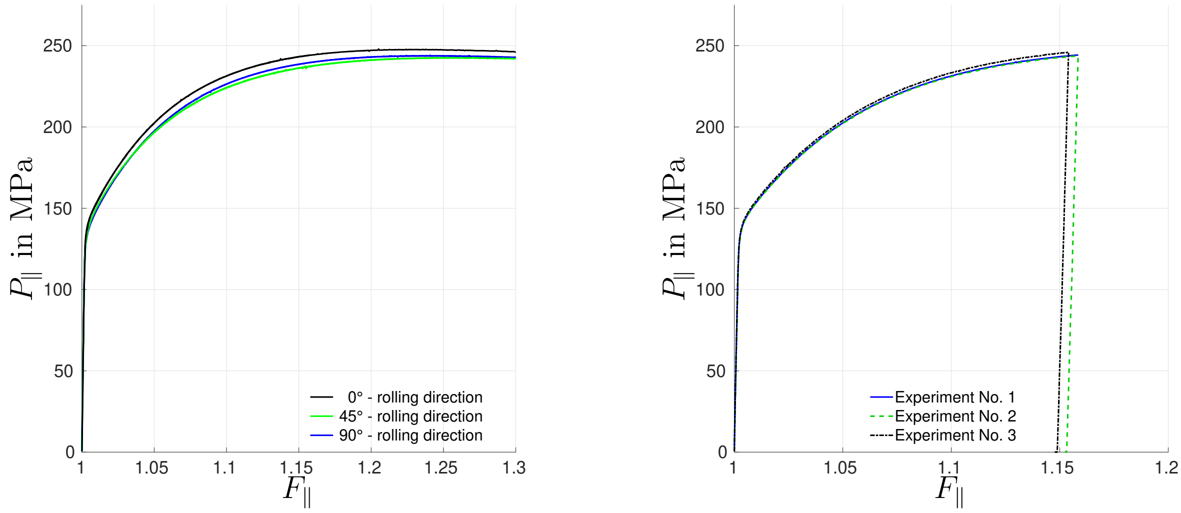

(a) Stress-strain relation for different rolling directions. Data of two experiments per considered rolling direction are shown.

(b) Stress-strain relation of the experiments used for the identification.

Figure 3.4: Experimental stress-strain relation using the Piola stress tensor $\boldsymbol{P}$ and the deformation gradient $\boldsymbol{F}$ ($(\bullet)_{||}$ denotes projection in tensile direction).

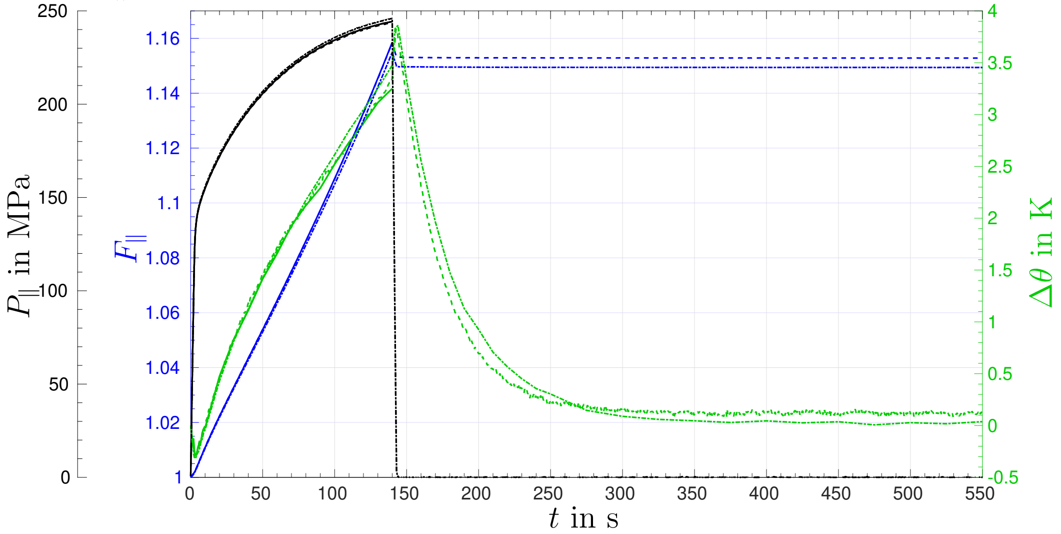

Figure 3.5: Stress, strain and temperature evolution of the centre point of the specimen over time for the experiment without cooling, No. 1 (–), as well as for the two experiments with cooling, No. 2 (- -) and No. 3 (-·-).

stretch in the area of interest. Analysing the data given in both Figures, 3.4b and 3.5, the experiments feature an almost identical stress strain relation starting with linear elastic material behaviour followed by plasticity with a saturation type of hardening. The temperature data indicates that each experiment considered here undergoes some elastic cooling before plastic heating leads to a temperature rise of approximately 3 K.

The experiments with cooling (no. 2 and 3) furthermore show a rise in temperature during elastic unloading, followed by the expected cooling down of the specimen.

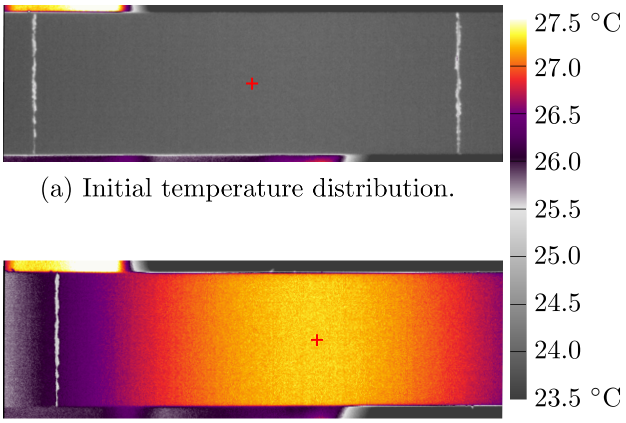

(a) Initial temperature distribution.

(b) Temperature field at 140 s.

Figure 3.6: Temperature field of specimen during the experiment.

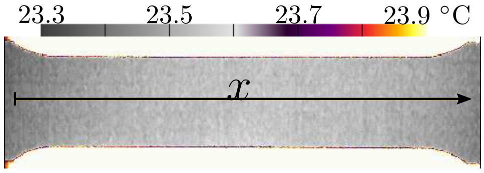

(a) Temperature distribution of a specimen.

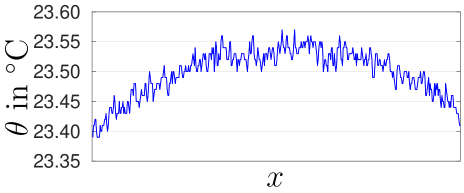

(b) Temperature distribution along $x-$axis.

Figure 3.7: Initial steady state temperature distribution.

Although the strain field is quasi homogeneous up to the point of localisation, the temperature is distributed inhomogeneously almost right from the start of the experiment. This is mainly due to the thermal boundary conditions at either end of the specimen, where heat is absorbed by the clamping jaws resulting in an extremum of temperature in the middle of the specimen, as can be seen in Figure 3.6. Moreover, it may appear at first glance that at least the initial temperature distribution of the specimen is homogeneous, but a closer look reveals a rise of temperature towards the middle of the specimen, see Figures 3.7a and 3.7b. An explanation is found in the temperature of the clamping jaws and the surrounding air which was measured using thermocouples at the beginning of each experiment. The clamping jaws are approximately 0.70 - 1.15 K colder than the surrounding air, see Table 3.2. Hence, thermal equilibrium enforces the temperature drop at either end of the specimen, even if the specimen is left in the clamping jaws for up to ninety minutes to reach a steady temperature state. It is worth mentioning that the temperature evolution of the clamping jaws is measured during (some of) the experiments using thermocouples. No significant change in temperature is detected.

Table 3.2: Measured temperatures at the boundaries of the specimen for each experiment.

No.	Clamping jaws in °C	Air in °C
1	23.10	24.25
2	23.80	24.50
3	23.55	24.25

4 Constitutive models for test cases

Two different constitutive models are introduced within this chapter to be used for different proofs of concept as this work proceeds, see Table 3.1. The underlying model parameters are briefly analysed with respect to identifiability on the basis of the experimental data at hand. In doing so, a successive scheme for the identification is motivated. The basics of material modelling - i.e. the derivation of constitutive relations from first and second law of thermodynamics, the procedure of Coleman and Noll, as well as the classic kinematic setting for large deformations - are assumed to be state of the art. These aspects are therefore not addressed in detail within this thesis. Readers unfamiliar with these topics are kindly referred to, for example [29], [54] or [40], where further details and more background are provided.

4.1 Model formulation

It was already mentioned that the choice of a particular constitutive model has a large impact on the result and quality of the identification. Although the routine will fit the parameters of any model to the experimental data in the sense of the objective function, the remaining errors can of course vary significantly for different models. However, two rather simple models which only cover some of the key aspects of the previously observed material behaviour are chosen for the proofs of concept in Chapter 5. More precisely speaking, both models are fully thermo-mechanically coupled, especially including the Gough-Joule effect as well as plastic heating. They feature isotropic elasticity, a Hill-type yield surface and saturating, isotropic hardening. Furthermore, a factor β scaling single dissipation contributions is included which has no influence on the thermodynamic consistency of either model as is proposed in [6]. In addition, surface elements are used to incorporate heat exchange with the environment, see e.g. [11]. The main difference between the models is the choice of evolution equations which are associated for one and non-associated for the other. Model 1 furthermore features linear hardening in addition to the exponentially saturating hardening.

It is worth mentioning at this point that both models will show a similar mechanical behaviour (if the linear hardening part of model 1 is deactivated), yet differ in the prediction of dissipated energy. Furthermore, the aforementioned factor β can be used to scale the amount of dissipated energy which would otherwise solely depend on mechanical model parameters. It is worth noting that β, as introduced in [6] and as used within this work, is not a Taylor-Quinney factor. In general, it describes neither the ratio of plastic work to dissipated energy nor the ratio of plastic power to dissipated energy rate. It is merely an additional model parameter, describing the amount of energy which is for example necessary for the creation and upholding of dislocations, the so-called stored or latent energy of cold work.

Remark 4.1. Before a model is chosen, some thought should be given to the question as to which kind of parameters can actually be identified with the experimental data at hand, or, if a model has already been chosen, what kind of experiments are required. It was mentioned in Section 3.2 that only data from a simple tension test in rolling direction is used for the identifications within this thesis as a proof of concept, so that no information about anisotropy is available for the identification process. Nevertheless, a model with an anisotropic yield surface is chosen due to the slightly higher flexibility of the model in comparison to a von Mises yield surface for example, even for the single, simple tensile test. Further reasons for the specific choice of the Hill-type yield surface is the interpretability of the associated model parameters. Based on this interpretation, Section 4.2 shows which parameters of the chosen model can be identified with the data at hand.

Both constitutive models are set up in a finite deformation setting with the deformation gradient $\boldsymbol{F} = \nabla_{\boldsymbol{X}}\, \boldsymbol{\varphi}$ of the deformation mapping $\boldsymbol{x} = \boldsymbol{\varphi}\,(\boldsymbol{X}, t)$. We shall assume a multiplicative split into an elastic contribution and a plastic part, i.e. $\boldsymbol{F} = \boldsymbol{F}^{\mathrm{el}} \cdot \boldsymbol{F}^{\mathrm{pl}}$. The free energy function

$$\begin{aligned}
\psi &= \psi^{\mathrm{el}} + \psi^{\mathrm{pl}} + \psi^{\mathrm{ther}} + \psi^{\mathrm{coup}} + \psi^{\mathrm{ns}} \quad \text{with} && (4.1)\\
\psi^{\mathrm{el}} &= \frac{\lambda}{2}\ln^2(J^{\mathrm{el}}) + \frac{\mu}{2}\left[\mathrm{tr}(\boldsymbol{C}^{\mathrm{el}}) - 3\right] - \mu\ln(J^{\mathrm{el}})\,, && (4.2)\\
\psi^{\mathrm{ther}} &= c_0\left[\theta - \theta_0 - \theta\,\ln\left(\frac{\theta}{\theta_0}\right)\right]\,, && (4.3)\\
\psi^{\mathrm{coup}} &= -\,3\,\alpha_{\exp}\,K_{\mathrm{bulk}}\,[\theta - \theta_0]\,\frac{\ln(J^{\mathrm{el}})}{J^{\mathrm{el}}}\,, && (4.4)\\
\psi^{\mathrm{ns}} &= [1-\beta]\,M_{y_0}\,\alpha, && (4.5)
\end{aligned}$$

is postulated for both models, using the determinant of the elastic deformation gradient $J^{\mathrm{el}} = \det\left(\boldsymbol{F}^{\mathrm{el}}\right)$, the right, elastic Cauchy-Green tensor $\boldsymbol{C}^{\mathrm{el}} = \left[\boldsymbol{F}^{\mathrm{el}}\right]^{\mathrm{t}} \cdot \boldsymbol{F}^{\mathrm{el}}$, as well as the internal hardening variable α and the absolute temperature field $\theta\,(\boldsymbol{X}, t)$. A non-standard contribution is added, as is proposed in [6], which will turn out to control the amount of energy which is either dissipated or latent during plasticity evolution. The only difference in the two free energy formulations lies within the chosen plastic part,

$$\text{Model 1} \quad \psi^{\text{pl}} = \frac{1}{2}\, H_{\text{lin}}\, \alpha^2 + \left[M_{y_\infty} - M_{y_0}\right] \left[\alpha + \frac{\exp(-H_{\exp}\, \alpha)}{H_{\exp}}\right] \tag{4.6}$$

$$\text{Model 2} \quad \psi^{\text{pl}} = \frac{1}{2} h\, \alpha^2 \,. \tag{4.7}$$

Regarding the derivation of the required constitutive equations, the local form of the Clausius-Duhem inequality can be used to obtain the constitutive equations for the Piola stress tensor $\boldsymbol{P}$, driving force K for the internal hardening variable and, based on $\boldsymbol{P}$, for the Mandel stress tensor $\boldsymbol{M}$, i.e.

$$\boldsymbol{P} = \frac{\partial \psi}{\partial \boldsymbol{F}^{\text{el}}} \cdot \left[\boldsymbol{F}^{\text{pl}}\right]^{-\text{t}} \,, \tag{4.8}$$

$$K = -\, \frac{\partial \psi}{\partial \alpha} \,, \tag{4.9}$$

$$\boldsymbol{M} = \left[\boldsymbol{F}^{\text{el}}\right]^{\text{t}} \cdot \boldsymbol{P} \cdot \left[\boldsymbol{F}^{\text{pl}}\right]^{\text{t}} = \left[\boldsymbol{F}^{\text{el}}\right]^{\text{t}} \cdot \frac{\partial \psi}{\partial \boldsymbol{F}^{\text{el}}} \tag{4.10}$$

by following the steps of the Coleman-Noll procedure. The driving force of the internal hardening variable is reduced to

$$\bar{K} = -\frac{\partial \psi^{\text{pl}}}{\partial \alpha} \tag{4.11}$$

for standard models without the non-standard energy contribution, which can also be retrieved by choosing $\beta = 1$. Fourier's law

$$\boldsymbol{q} = -\kappa_{\text{therm}}\, \nabla_{\boldsymbol{x}} \theta \tag{4.12}$$

is assumed to govern the heat flux in the spatial configuration, so that the Fourier part of the Clausius-Duhem inequality is always fulfilled. Regarding heat exchange with the environment, the heat flux normal to the current surface of the body is incorporated by using the equation

$$q_0 = \boldsymbol{n} \cdot \boldsymbol{q} = -\alpha_{\text{con}} \left[\theta^{\text{M}} - \theta\right] \,, \tag{4.13}$$

depending on the convection or conduction coefficient α_{con} and on the temperature of the surrounding medium θ^{M}, see e.g. [11] for more details.

The approach for a standard model formulation is used to define the evolution equations for the plastic velocity gradient $\boldsymbol{L}^{\text{pl}} = \dot{\boldsymbol{F}}^{\text{pl}} \cdot \left[\boldsymbol{F}^{\text{pl}}\right]^{-1}$ and the internal hardening variable α, i.e.

$$\boldsymbol{L}^{\text{pl}} = \lambda_{\text{pm}} \frac{\partial g}{\partial \boldsymbol{M}} \,, \tag{4.14}$$

$$\dot{\alpha} = \lambda_{\text{pm}} \frac{\partial g}{\partial \bar{K}} \,, \tag{4.15}$$

with the Lagrange or plastic multiplier λ_{pm} and the plastic potential g. The plastic potential is chosen differently for each model,

$$\text{Model 1} \qquad g = \Phi \tag{4.16}$$

$$\text{Model 2} \qquad g = \Phi + \frac{1}{2}\frac{b}{h}\,\bar{K}^2\,. \tag{4.17}$$

Both potentials make use of the yield function

$$\Phi = \sqrt{\boldsymbol{M} : \mathbf{G} : \boldsymbol{M}} - \beta\, M_{y_0} + K \tag{4.18}$$

with the fourth order tensor $\mathbf{G}$ representing Hill-type plastic anisotropy, see Appendix D. A comment on the reason for the specific formulation of the plastic potential for the non-associated model can be found in Remark 4.3 at the end of this section. If the definition of the driving force K is inserted into the chosen form of the yield function, the standard formulation of a Hill type yield surface

$$\begin{aligned} \Phi &= \sqrt{\boldsymbol{M} : \mathbf{G} : \boldsymbol{M}} - M_{y_0} + \bar{K}\,, \\ &= \Big[F\,[M_{11} - M_{22}]^2 + G\,[M_{33} - M_{11}]^2 \\ &\quad + H\,[M_{22} - M_{33}]^2 + 2\,L\;M_{12}^2 + 2\,M\;M_{23}^2 \\ &\quad + 2\,N\;M_{13}^2\Big]^{\frac{1}{2}} - M_{y_0} + \bar{K} \end{aligned} \tag{4.19}$$

is retrieved, introducing the six Hill parameters F, G, H, L, M, N with the coefficients of the Mandel stress tensor referring to the underlying (aligned) orthonormal frame. Time integration is done by means of a simple backward Euler scheme.

For the sake of interpretation in later sections, the balance of energy is given as

$$c_0\,\dot{\theta} = \rho_0\, r - \nabla_{\boldsymbol{X}} \cdot \boldsymbol{Q} + \mathcal{D}^{\mathrm{mech}} + \theta\,\frac{\partial^2\psi}{\partial \boldsymbol{F}^{\mathrm{el}}\,\partial\theta} : \dot{\boldsymbol{F}}^{\mathrm{el}} \tag{4.20}$$

with $\boldsymbol{Q} = \det(\boldsymbol{F})\;\boldsymbol{q} \cdot \boldsymbol{F}^{\text{-t}}$ and with the referential heat capacity $c_0 = -\,\theta\,\frac{\partial^2\psi}{\partial\theta\,\partial\theta}$ being constant due to the chosen form of the thermal free energy contribution as introduced in Equation (4.3). Furthermore, the particular models at hand yield fundamentally different equations for the mechanical dissipation,

$$\text{Model 1} \qquad \mathcal{D}^{\mathrm{mech}} = \beta\,\lambda_{\mathrm{pm}}\,M_{y_0} \tag{4.21}$$

$$\text{Model 2} \qquad \mathcal{D}^{\mathrm{mech}} = \lambda_{\mathrm{pm}}\left[b\,h\,\alpha^2 + [1-\beta]\,b\,M_{y_0}\alpha + \beta\,M_{y_0}\right]. \tag{4.22}$$

Equations (4.21) and (4.22) show that the dissipation of both models is always larger or equal to zero as long as β lies within the model specific boundaries

$$\text{Model 1} \qquad \beta \geq 0\,, \tag{4.23}$$

$$\text{Model 2} \qquad 0 \leq \beta \leq 1 \quad \vee \quad \beta_{\mathrm{l}} \leq \beta \leq \beta_{\mathrm{u}}\,, \text{ with} \tag{4.24}$$

$$\beta_{\mathrm{u,l}} = \frac{M_{y_0}\, b + 2h \left[1 \pm \sqrt{\frac{M_{y_0}\, b}{h} + 1} \right]}{M_{y_0}\, b}\,. \tag{4.25}$$

A detailed derivation of the limit values of β for model 2 can be found in Appendix E.

Remark 4.2. Regarding model 1, the constitutive equation for stresses, the evolution equation for the plastic contribution to the deformation gradient and internal hardening variables as well as the yield surface are independent of the non-standard addend to the free energy and therefore independent of parameter β which only influences the amount of dissipated energy. The mechanical response of model 1 is therefore identical to the associated standard model formulation, if coupling effects due to the rise of 3 K for the case at hand are neglected. Furthermore, the chosen evolution equations for model 1 can also be obtained through the postulate of maximum dissipation.

Remark 4.3. There are general, well-established frameworks, such as the one of generalised standard materials (GSM), which guarantee a non-negative dissipation if the plastic potential of a model with non-associated evolution equations is defined accordingly. The commonly used formulation

$$\tilde{g} = \Phi + \frac{1}{2}\frac{b}{h}\, K^2 \tag{4.26}$$

meets all requirements of the GSM approach and therefore also guarantees a non-negative dissipation. However, this choice for a plastic potential leads to evolution equations that depend on parameter β. Thus, the evolution equations are no longer comparable to the ones of a standard model formulation, i.e. without the non-standard energy contribution. This, in our case, undesired effect can be remedied by the simple modification in Equation (4.18). The alternative formulation may violate some of the conditions of the GSM approach, so that its line of reasoning can not be applied to the second model. It is therefore shown in Appendix E that this specific choice nonetheless fulfils the dissipation inequality. The mechanical response of model 2 is therefore identical to the standard model formulation if coupling effects due to the experimentally observed rise of 3 K are neglected so that parameter β only influences the amount of dissipated energy.

Remark 4.4. As was mentioned above, the mechanical response of both models is identical to the one of their standard model counterpart, i.e. without the non-standard addend ψ^{ns} of the free energy, since this addend only influences the amount of dissipated energy. It is furthermore shown in Appendix F that the mechanical response of these two standard models is identical in the range of small strains if

$$b = H_{\text{exp}} \qquad \text{and} \tag{4.27}$$

$$\frac{h}{b} = [M_{y\infty} - M_{y0}] \ , \tag{4.28}$$

assuming a neglectable influence of the low rise in temperature and dismissing the linear hardening part of model 1. The mechanical response of the two models at hand is therefore also identical under the assumptions mentioned before and can be assumed to be at least comparable for large deformations. Thus, the hardening parameters H_{exp} and $M_{y\infty}$ will be used for both models in the following.

Remark 4.5. It is worth noting that Young's modulus E and Poisson's ratio ν are used within the identification process instead of the two Lamé parameters λ, μ and the bulk modulus K_{bulk} which were used for the definition of the energy contributions above.

4.2 Model parameters

It is important to know which kind of influence each model parameter has on the material response in order to obtain meaningful results through a parameter identification scheme. More precisely speaking, the question of identifiability must be raised and answered with respect to the kind of experiments which are required for the model at hand. This can be done either by means of the approximated Hessian of the objective function, by an analysis of the underlying constitutive equations, or by using a grid search method in order to receive information towards the uniqueness of the solution within a certain area in parameter space, see Section 2.8. The last two options are considered in this thesis, starting with an analysis of the constitutive equations to see which of the 16 model parameters from Table 4.1 are identifiable and which are not. More precisely speaking, this analysis provides information as to which parameters of the models can and which can not be identified on the basis of the experiments at hand, information on the dependency of model parameters and information on the possibility to identify subsets independently. Mechanical parameters which are found to have no influence on the boundary value problem at hand are directly excluded from the identification process. Different and suitable experiments should generally be used for such cases, but it is not the aim of this work to obtain mechanical material parameters which can be used for predictive simulations of different boundary value problems.

Regarding the identification process itself, it should theoretically be possible to identify all model parameters at once, but such a procedure is usually not advisable. Furthermore, computation time can in some cases be reduced if it is possible to identify subsets of the model parameters separately. This, however, can only be done if the effect of certain model parameters on the material response can be separated, which is possible for common mechanical models but requires certain assumptions for the thermo-mechanically coupled models presented above. More precisely speaking, the low change in temperature of approximately 3 K for the experiments at hand is assumed to have no significant influence on the displacement field, allowing a separate and stepwise identification of elastic, plastic and finally the thermal model parameters. To further understand which parameters can be identified with the experiments presented in Section 3.4, the exact influence on the material response is analysed in the following.

Table 4.1: Model parameters of the models.

E	Young's modulus
ν	Poisson's ratio
M_{y_0}	Initial yield limit
F, G, H, L, M, N	Hill parameters
H_{lin}	Linear hardening modulus (only model 1)
M_{y_∞}	Exponential hardening limit
H_{exp}	Exponential saturation speed
α_{exp}	Thermal expansion coefficient
κ_{therm}	Thermal conduction coefficient
c_0	Heat capacity
β	Dissipation factor

Step 1 - Elastic model parameters No significant correlation between the two elastic model parameters E and ν is expected, allowing a unique identification of both parameters on the basis of displacement data in tension and lateral direction. Although the elastic strains of a simulation are generally influenced by the aforementioned elastic model parameters and the thermal expansion coefficient α_{exp}, it can be assumed that the latter has no influence on the mechanical field in the elastic regime due to the low change in temperature. This allows the separate identification of E and ν in a first step for both models, based solely on the measured displacement field. Thus, only data up to the point of yielding must be used, which can be found either by considering the force-time curve in the case of homogeneous strains or by detecting the first rise of temperature due to a plastic loading state.

Step 2 - Plastic model parameters The evolution of plasticity is controlled by the yield function which is assumed to have the form

$$\begin{aligned}\Phi = &\Big[F\,[M_{11}-M_{22}]^2 + G\,[M_{33}-M_{11}]^2 + H\,[M_{22}-M_{33}]^2 \\ &+2\,L\;M_{12}^2 + 2\,M\;M_{23}^2 + 2\,N\;M_{13}^2\Big]^{\frac{1}{2}} \\ &-[M_{y0} + H_{\text{lin}}\;\alpha + [M_{y\infty} - M_{y0}]\,[1-\exp(-H_{\text{exp}}\,\alpha)]]\;,\end{aligned} \tag{4.29}$$

for model 1 with the six Hill parameters F, G, H, L, M and N, cf. Equations (4.19) and (4.11). Each of these parameters are assigned to one or two stress coefficients of $\boldsymbol{M}$ and thus only have an influence on the flow surface if the associated stress components are non-zero. For the present case of simple tension, only one principal value of $\boldsymbol{P}$ is non-zero in the area of interest, i.e. the area which is sufficiently far away from the clamps and which is observed by the DIC system. Due to the relation between the two stress measures in Equation (4.10), $\boldsymbol{M}$ and $\boldsymbol{P}$ possess the same pattern of non-zero and zero components for the specific loading case considered. Hence, the Hill parameters governing the influence of shear stresses on the flow surface, i.e. L, M and N, cannot be identified with the data at hand. Concerning the Hill parameters associated with normal stresses, only two of the three parameters F, G and H have a direct influence on the simulated displacement field, since one of these parameters will always be multiplied with zero coefficients of the uniaxial stress tensor. Furthermore, only the ratio of the remaining Hill parameters is of importance. If, for instance, a uniaxial load in 2-direction is assumed, the flow surface takes the form

$$\begin{aligned}\Phi = &\;\big[[F+H]\;[M_{22}]^2\big]^{\frac{1}{2}} - [M_{y0} + H_{\text{lin}}\;\alpha + [M_{y\infty} - M_{y0}]\,[1-\exp(-H_{\text{exp}}\,\alpha)]] \\ = &\;\Big[\sqrt{H}\Big]\Bigg[\bigg[\frac{F}{H}+1\bigg]^{\frac{1}{2}}\;[M_{22}] - \bigg[\frac{M_{y0}}{\sqrt{H}} + \frac{H_{\text{lin}}}{H}\;\sqrt{H}\alpha \\ &\qquad + \bigg[\frac{M_{y\infty}}{\sqrt{H}} - \frac{M_{y0}}{\sqrt{H}}\bigg]\bigg[1-\exp\Big(-\frac{H_{\text{exp}}}{\sqrt{H}}\;\sqrt{H}\alpha\Big)\bigg]\bigg]\Bigg] \\ \leq &\;0\,,\end{aligned} \tag{4.30}$$

where F/H determines when the yield limit is reached for a fixed stress state. Regarding the evolution of the yield surface, all plastic model parameters are in one way or another scaled by H which is explained in detail in Appendix G. Hence, an infinite number of possible solutions exists, all representing the same yielding and hardening behaviour for such a uniaxial case. This means that only one of the two remaining Hill parameters can be pre-identified with data from a simple tension test with fixed loading direction, while the value of the other parameter must be chosen and fixed throughout the optimisation. Regarding the remaining plastic parameters of the material, the hardening modulus H_{lin}, as well as the parameters for the exponential hardening $M_{y\infty}$ and H_{exp} have a unique influence on the evolution of plastic hardening, so that some correlation but not a dependency in the sense of Section 2.8 is expected. Although the above analysis is made with respect to model 1, it can also directly be applied to model 2, since both models are identical in their mechanical response and feature similar model parameters as was already mentioned in Remark 4.4.

Step 3 - Thermal model parameters Assuming that the mechanical field has an influence on the thermal field but not vice versa allows the separate identification of the mechanical model parameters on the basis of the displacement field data, as described above. This means that these parameters as well as their influence on the mechanical and thermal field are already fixed, leaving only the four thermal parameters α_{exp}, c_0, κ_{therm} and β open to fit the computed temperatures to the experimental data.

For a standard model formulation, i.e. setting $\beta = 1$, the amount of dissipated energy and therefore the amount of heat which can be used for a change in temperature is fixed along with the choice of the mechanical model parameters, see Equations (4.20), (4.21) and (4.22). Hence, the thermal conduction coefficient κ_{therm} and heat capacity c_0 determine quality and quantity of the temperature distribution during plastic heating. These two parameters can possibly be fitted by means of the measured part of the temperature field. Assuming that this information is sufficient to determine the aforementioned two thermal model parameters, the thermal expansion coefficient α_{exp} is the only remaining parameter to control the quantity of the elastic cooling effect, see Equations (4.20) and (4.4).

In the case of the non-standard model formulation, however, parameter β can have a high correlation to the aforementioned thermal model parameters, depending on the chosen BVP. The parameter is not redundant, i.e. there is no model intrinsic dependency, but its unique identification greatly depends on the thermal boundary conditions as well as on the precise influence of β on the dissipation. A general statement about correlation, dependency and required data regarding the four thermal parameters of the models at hand therefore proves to be difficult. Instead, an interpretation for the precise cases at hand is given in Section 5.4, where the thermal boundary conditions for the BVP considered in this work are defined.

It is worth mentioning that, in contrast to the mechanical field, the thermal boundary conditions are usually unknown, at least a part of them. Although the temperature of the surrounding air and of the clamping jaws might be measurable, the convection or conduction coefficients are generally unknown. A value for these parameters must either be assumed or identified.

Remark 4.6. Some effects are deliberately not considered within the models, such as rate-dependency of the material or a precise representation of the anisotropy, e.g. the Hill surface is considered to generally represent aluminium alloys rather poorly, cf. [5]. The model is deliberately chosen to be as complex as necessary, yet as simple as possible for the sake of the proofs of concept that are the main focus of this thesis. If truly valid material parameters are required which can be used for predictive simulations of more complex boundary value problems, i.e. with an inhomogeneous strain distribution, the aforementioned issues should of course be addressed and incorporated in the constitutive model first.

4.2.1 Model dependency

If different models yield truly valid parameter sets, all parameters with a physical interpretation must intrinsically coincide, e.g. point of yielding in a specific direction, heat capacity, etc., at least up to an acceptable limit which marks the difference between pass and fail in the validation process. On the other hand, two models which can be verified but are non-valid will usually yield different optimal model parameters, even for parameters which have the same physical interpretation. Consider for example thermo-mechanically coupled models. The main reason for a rise in temperature usually is the mechanical dissipation $\mathcal{D}^{\text{mech}}$ which is transformed to heat. However, the amount of dissipated energy differs significantly for the models presented in this chapter whereas it can be shown that both models yield an identical stress-strain relation (for small strains at least), as is shown in Appendix F. Hence, it is only to be expected that the optimal thermal model parameters will also differ for each of these models. This example underlines that a parameter identification does not necessarily compute the true material parameters but rather determines the optimal parameters for the provided input, as was explained in Section 2.9.

5 Parameter identification

This chapter provides information on and results of the performed identifications using the general framework proposed in Chapter 2 and drawing on the experimental data and constitutive models presented in Chapter 3 and 4. Each identification itself follows the scheme already indicated in Section 4.2, identifying elastic and plastic parameters separately before the thermal model parameters are optimised. Several questions related to applicability of the proposed framework are answered. More precisely speaking, the identifiability of thermal model parameters is investigated by gradually increasing the number of unknown parameters, thereby also increasing the complexity of the optimisation process.

In Section 5.3, the general applicability of the proposed identification scheme for thermo-mechanically coupled constitutive models using full field displacement and temperature data is shown, proving that the classic thermal model parameters of a standard model are identifiable on the basis of a simple tension test under monotonous loading. The result is subjected to verification and validation.
In Section 5.4, the extended, non-standard model formulations are compared, adding an additional thermal model parameter. Focus of that section is again the identifiability of the model parameters, showing what kind of data is required for a (locally) unique fit of the enhanced models and underlining how small changes in the model formulation influence the result of the optimisation. Obtained results are again verified and validated.
In Section 5.5, the boundary coefficients are considered as additional unknowns during the optimisation. Identifiability and sensitivity of the extended set of thermal model parameters is analysed, closing with an attempt to obtain not only verifiable but also valid model parameters.
It is worth mentioning that, although verification and validation are performed for all identifications at hand, it is not the aim of this thesis to provide material parameters which can be used for predictive simulations of arbitrary boundary value problems (which is highly model dependent). Instead, the central theme is the general identifiability of thermal parameters as is also indicated by the research questions formulated at the start of each of the sections mentioned above. Before the identifications are performed, however, the boundary value problem as well as details of the identification scheme used within this thesis are specified.

5.1 Identification scheme

The FEMU method is applied to the inverse problems considered within this thesis, following the framework and the algorithmic structure presented in Chapter 2. Remaining details which were not specified in the general description, e.g. the segmentation of the identification process and the choice of weights within the objective function, are given below. Regarding the optimisation algorithm, a gradient-free scheme from the open source toolbox NLopt, see [32], is applied. More precisely speaking, an implementation of the Nelder-Mead Simplex method with bound constraints is used, as documented in [52] and [12].

5.1.1 Successive parameter identification approach

Following the successive scheme motivated in Section 4.2, the identification is split into three stages:

1. Identification of elastic parameters.
   All other parameters are fixed and are not part of the optimisation. Only the elastic loading range of the displacement field data is considered.

2. Identification of plastic parameters.
   The elastic parameters are fixed at the values known from step 1. Apart from the plastic parameters, all other parameters are fixed as well and are not part of the optimisation. Only displacement field data is considered.

3. Identification of thermal parameters.
   The mechanical parameters are fixed at the values obtained from the first two stages. Only temperature data is considered.

5.1.2 Objective function

If not mentioned otherwise, the objective function from Equation (2.24) is used, comparing relative displacements and temperatures. Only those nodes on the xy-plane which are inside the black rectangle ($|y| > 20$ mm) in Figure 5.1 are considered and contribute to the objective function value. Nodes too close to the edge of the specimen ($x > 11$ mm) are neglected as well. The weights W^{u} for x- and y-components of the remaining nodes are chosen so that an almost equal influence on the overall objective function value is ensured. Values vary for different identifications and are specified within the respective sections. Displacement data in z-direction is not used and the related weights are set to zero for every node considered. All identifications that involve temperature data are performed with a value of $W^{\theta} = 1$. The load steps at which the objective function is evaluated are indicated by markers in the stress-strain and temperature-time curves in the respective Section of each identification. It is worth mentioning that the time step

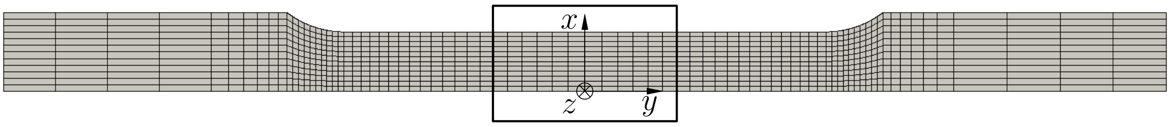

Figure 5.1: Only nodes within the black window which do not lie on the edge of the specimen are considered within the objective function.

density can also be seen as some kind of weighting. Evaluation points are chosen to cluster around points, respectively loading states of significance, such as temperature maxima and minima or the onset of plasticity.

Remark 5.1. If working with Robin-type boundary conditions, time steps must be chosen to be small enough to account for the temperature dependency and hence time dependency of such conditions. Otherwise, at least the accuracy of the time integration scheme should be considered.

5.2 Boundary value problem

In order to perform a parameter identification using the FEMU method, an FE model is required. Main parts are the mesh and the boundary conditions, both of which should represent the experiment as accurately as possible to avoid physics- and mathematics-related errors.

5.2.1 Finite element discretisation

The body under consideration is modelled according to the dimensions of the specimen from Figure 3.2. Thickness and width of each specimen is measured prior to the experiments in order to take into account possible deviations during the manufacturing process of the respective specimen. By assuming symmetric deformation throughout the experiment the model can be reduced to a fourth of the original specimen. Hence, only half the width and half the thickness are considered. Regarding the discretisation of the body, the mesh shown in Figure 5.2 is chosen to be rather coarse in areas where only homogeneous stresses are expected, and to be comparatively fine in areas of inhomogeneous stress states. The mesh should generally be chosen to be fine enough so that further mesh refinement has no significant influence on the simulation results.

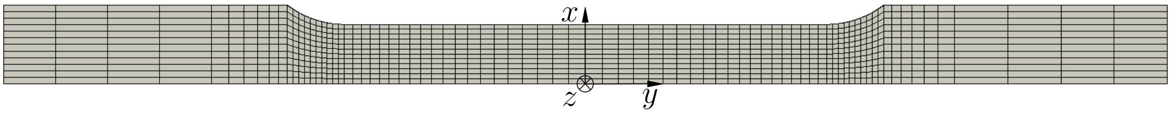

(a) Top view.

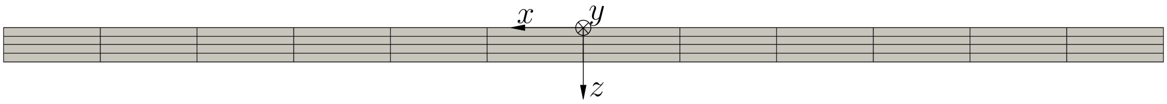

(b) Side view from left.

Figure 5.2: Discretised FE model of the specimen.

The mesh at hand consists of a total of 3840 brick elements with linear shape functions for the approximation of the displacement and temperature fields. In addition, 1280 surface elements are used to model heat exchange with either the surrounding air or with the clamping jaws.

5.2.2 Boundary conditions

For the thermo-mechanically coupled boundary value problem, mechanical and thermal boundary as well as initial conditions must be defined and shall be discussed in the following paragraphs.

Mechanical boundary conditions The boundary conditions of Dirichlet and Neumann type can be transferred from the experiments with few assumptions. Rigid body motions of the specimen observed during the experiment are neglected since they can be excluded by means of the chosen objective function, which compares relative displacements, see Section 2.6.2. Hence, the displacement of the nodes on the green (left) surface in Figure 5.3 is clamped in $y-$direction, and the measured experimental force is applied onto the nodes on the blue (right) surface. For the latter, a linear constraint is used so that all nodes on the blue (right) surface must undergo the same displacement in y-direction. A fourth of the experimental force is then applied to one of the nodes, since only a fourth of the specimen's cross-section is considered. The exact prescribed force, as well as the time range used for the identification of elastic, plastic and thermal model parameters varies slightly for each experiment and is therefore given in the respective sections as this work proceeds. Regarding the required symmetry conditions, nodes within the yz-plane at $x = 0$ are clamped in x-direction and nodes within the xy-plane at $z = d/2 \approx 0.6$ mm (depends on measured thickness d of specimen) are clamped in z-direction.

It is worth mentioning that, although it seems tempting to reduce the model even further in y-direction and to apply the measured displacements directly on the new boundary,

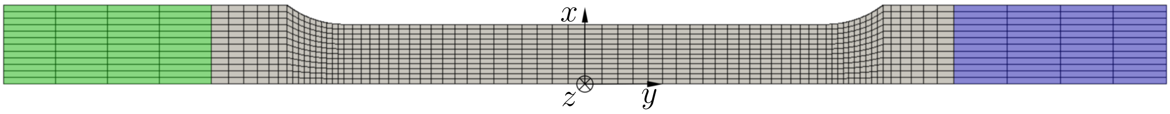

Figure 5.3: Top view of the model – Nodes on the green (left) surface are clamped and nodes on the the blue (right) surface are loaded with the measured force. Symmetry conditions are applied.

this is usually connected with further assumptions, e.g. that the displacement in axial and lateral direction is not a function of the coordinate z. The accuracy of this assumption probably strongly depends on the thickness of the specimen. More importantly however, it is not always possible to measure the displacement on the edge of the specimen with common DIC systems. In the case that experimental displacements are used as Dirichlet boundary conditions, the measured values have to be interpolated on the node positions. If no data is available at the edges, the information for these nodes must therefore be extrapolated which can lead to substantial errors if not treated carefully.

Thermal boundary and initial conditions In contrast to the mechanical boundary conditions, the thermal conditions are usually unknown. Heat is exchanged with the environment, to be more precise, with the surrounding air and the clamping jaws. For this reason, every outward surface is represented by means of a surface element which accounts for such a surface flux, whereby a constant temperature of the surrounding medium θ^{M} and a constant coefficient α_{con} are assumed, see Equation (4.13). In addition, an initial temperature has to be assigned to each node of the mesh.

The temperatures of the surface elements representing the clamping jaws and the surrounding air are set to the measured values shown in Table 3.2. Since the temperature of the clamping jaws does not rise throughout the experiments considered, we assume a very high conduction coefficient of $\alpha_{\mathrm{con}}^{\mathrm{clamp}} > 10^8$ W/[m^2 K], leading to isothermal boundary conditions in the vicinity of the jaws. Concerning the convection coefficient towards air, literature, e.g. [30], suggests a value between 2 and 25 W/[m^2 K]. Alternatively, a convection coefficient for an infinitely long wall of the same heights as the specimen can be computed analytically. Such an estimation yields a convection coefficient between 0 and 3 W/[m^2 K], depending on the temperature difference between wall (specimen) and air. In summary, the literature as well as an analytical estimation of the convection coefficient towards air do not provide an exact value for the required convection coefficient, but suggest that the sought value must be considerably smaller than the conduction coefficient for the clamping jaws, $\alpha_{\mathrm{con}}^{\mathrm{air}} \ll \alpha_{\mathrm{con}}^{\mathrm{clamp}}$. Taking into account that the heat conduction of aluminium itself is rather high, it is therefore assumed that heat conduction through the clamping jaws is the main mechanism for heat exchange with the environment. The loss of heat through convection is hence neglected by setting $\alpha_{\mathrm{con}}^{\mathrm{air}} = 0$. The two model parameters defining the surface elements are prescribed to the aforementioned values for all identifications unless explicitly stated otherwise.

Regarding the initial temperature value of each node, the exact temperature distribution along the hole specimen is unknown since only a part of the specimen was detected by the thermography system. As described in Section 3.4 however, mechanical load was only applied to the specimen after an initial steady temperature state was reached. Thus, the same conditions are considered within the simulation, rendering the choice of the exact initial temperature values trivial.

Finally, to enforce the aforementioned symmetry in temperature distribution, the heat flux over the symmetry planes is set to zero.

5.3 Identifiability of thermal model parameters

Since, to the author's best knowledge, the algorithmic structure presented in Section 2.5 has so far never been used to identify thermal model parameters on the basis of real (as opposed to numerically) experimental data of a simple tension test, the following questions arise.

- Does the proposed framework allow an identification in general?
- Does the use of relative displacements compensate rigid body motion as is expected?
- Is a (locally) unique fit of the three classic thermal model parameters possible on the basis of a real simple tension test?

Hence, the general identifiability of the classic thermal model parameters, i.e. α_{exp}, κ_{therm} and c_0, is empirically shown within this section as a proof of concept that these parameters can be identified on the basis of a simple tension test. More precisely speaking, data from experiment no. 1 (monotonous loading only, see Table 3.1) and model 1 are used as the basis of an identification following the successive scheme as described above. Furthermore, the identification of the elastic model parameters is used to show the difference between using displacements and relative displacements in the objective function, cf. Equations (2.8) and (2.10). It is worth mentioning that, for this first and general proof of concept, model 1 is reduced to the standard model formulation by setting the scaling parameter $\beta = 1$, see Section 4.1.

5.3.1 Step 1 - Identification of elastic parameters

Choosing the parameter set from Table 5.1 as initial guess, the identification is performed twice to underline the effect of relative displacements within the objective function. Hence, one identification directly uses displacements within the objective function while the second identification draws on relative displacements within the error measure which intrinsically eliminates the influence of unwanted rigid body motions. Neither temperatures nor reaction forces, but only displacements in $x-$ and $y-$direction are used within either objective function. The weighting factors are manually set to $W_x^{\mathrm{u}} = 1$ and $W_y^{\mathrm{u}} = 1$ and the experimental reaction force of up to two seconds is prescribed as load to ensure that the elastic parameters are identified on the basis of purely elastic experimental data, see Figure 5.4. Table 5.2 holds the results of these identifications, showing that the improved formulation yields results close to the values found in literature, e.g. [31], whereas the commonly used objective function based directly on displacements leads to a solution which lets the material appear softer. This example thereby highlights the necessity to take rigid body motion during the experiment into account as well as the capability of relatives displacements to do so. The experimental data is not matched exactly, but some error remains which is expressed by the remaining contribution of each considered FE-node to the objective function. However, this error is

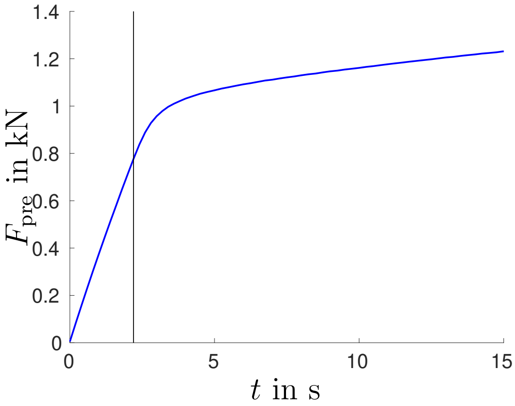

Figure 5.4: Prescribed force F_{pre} over time for identification based on experiment no. 1. Vertical, black line indicates end time $t_{\mathrm{end}}^{\mathrm{el}} = 2.0$ s for identification of elastic parameters.

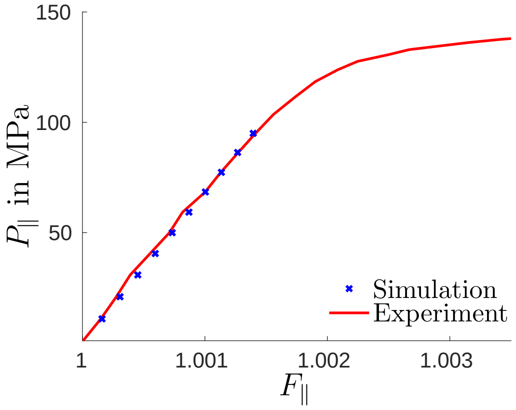

Figure 5.5: Local stress-strain relation for optimal elastic parameter set using model 1 and experiment no. 1, evaluated at the midpoint of the specimen.

Table 5.1: Initial guess for elastic model parameters.

Model parameter	E in MPa	ν
Value	60000	0.30

Table 5.2: Identified elastic model parameters for AW6016 using model 1 and experiment no. 1.

Objective function	E in MPa	ν
Displacements	58317	0.10
Relative displacements	67913	0.35
Literature	69000	0.33

rather homogeneously distributed over all nodes and all time steps, see Figures 5.6 and 5.5, suggesting that model 1 represents the real material behaviour adequately during elastic deformations.

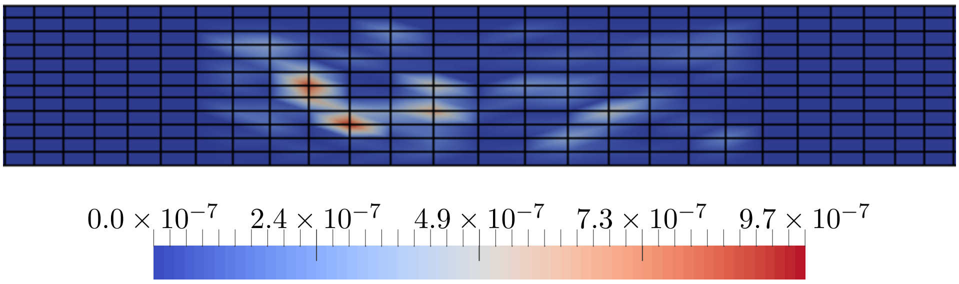

Figure 5.6: Remaining nodal contribution to the mechanical (displacement) part of the objective function at time $t = 2.0$ s using model 1 and experiment no. 1.

5.3.2 Step 2 - Identification of plastic parameters

With the elastic parameters at hand, those plastic parameters can be identified which have an influence on the one-dimensional stress state of the simulation. To do so, experimental data is required which is well past the point of initial yielding. For the present case, displacement data up to the time of $t = 140$ s is employed, see Figure 5.7. The loading stages at which simulation results and experimental data are compared can be seen in Figure 5.8. The weighting factors are chosen to be $W_x^{\mathrm{u}} = 5$ and $W_y^{\mathrm{u}} = 1$. Again, no use is made of the temperature data. Starting at the parameter set displayed

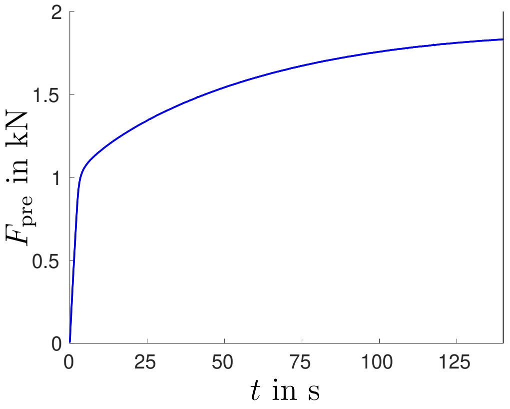

Figure 5.7: Prescribed force F_{pre} over time for identification based on experiment no. 1. Vertical, black line indicates end time $t_{\mathrm{end}}^{\mathrm{pl}} = t_{\mathrm{end}}^{\mathrm{therm}} = 140$ s for identification of plastic and thermal parameters.

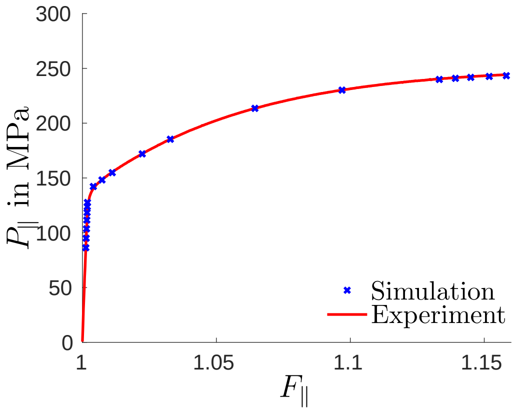

Figure 5.8: Local stress-strain relation for optimal plastic parameter set using model 1 and experiment no. 1, evaluated at the midpoint of the specimen.

Table 5.3: Initial and obtained values for plastic model parameters on the basis of model 1 and experiment no. 1.

Model parameter	M_{y0} in MPa	$M_{y\infty}$ in MPa	H_{lin} in MPa	H_{exp}	F
Initial guess	140.00	290.00	100.00	15.00	0.50
Optimal value	129.71	253.12	173.30	14.11	0.38

in Table 5.3, the identification leads to the result shown in the same table. The remaining squared error in displacements is quasi homogeneously distributed in each time step as can exemplarily be seen in Figure 5.9. Thus, model 1 is appropriate for the representation of the mechanical behaviour of the aluminium alloy during elastic as well as plastic loading stages, at least for the one-dimensional stress state considered.

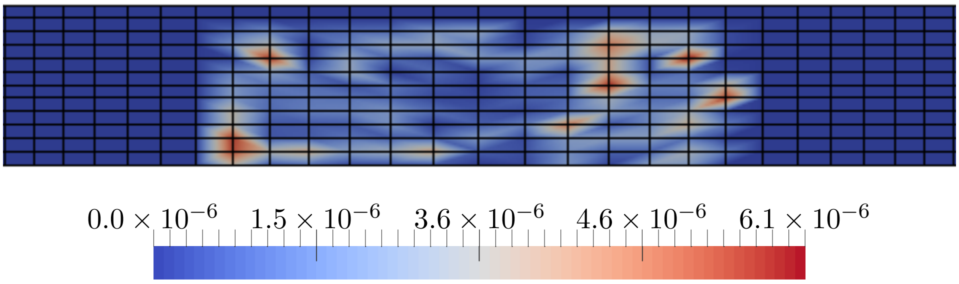

Figure 5.9: Remaining nodal contribution to the mechanical (displacement) part of the objective function at time $t = 140$ s using model 1 and experiment no. 1.

5.3.3 Step 3 - Identification of thermal parameters

Using the previously obtained values for the mechanical parameters, the caloric quantities can be identified on the basis of the measured temperature field alone. Again, data up to the time of $t = 140$ s is used and the points of comparison in time are distributed with a higher density around important effects, e.g. elastic cooling, see Figure 5.11.

It was already established in Section 4.2 that no model intrinsic dependency between the three thermal model parameters of a standard model α_{exp}, κ_{therm} and c_0 is expected. Nevertheless, incompleteness of data could still lead to a non-unique result, so that in this first proof of concept the identifiability of the three aforementioned, classic thermal model parameters is further investigated by means of a grid search approach, see Section 2.8.4. For the sake of convenience, the units of the different parameters are mentioned in Table 5.4 in order to skip these units in the subsequent tables. The value of the objective function at the end of the optimisation process is denoted by f^{θ} which is identical to the remaining, unweighted squared error between simulated and experimental changes in the temperature field. Table 5.5 shows the different starting sets and Table 5.6 holds the obtained model parameters for each initial guess, as well as the remaining value of the objective function f^θ. It can be seen that all of the chosen initial guesses lead to the same minimum. Although this is not equivalent to a mathematical proof that no better solution for the optimisation problem at hand exists, it is nevertheless a strong indicator for the identifiability of the classic thermal model parameters on the basis of a simple tension test.

Table 5.4: Units of the different parameters.

Parameter	Unit
α_{exp}	10^{-6}/K
κ_{therm}	mW/[mm K]
c_0	mJ/[mm^3 K]
f^θ	K^2

Table 5.5: Different starting points $\boldsymbol{k}_0^i$ for the identification of thermal model parameters on the basis of model 1 and experiment no. 1.

Initial set	α_{exp}	κ_{therm}	c_0
$\boldsymbol{k}_0^1$	23.00	200.00	2.43
$\boldsymbol{k}_0^2$	46.0	200.00	2.43
$\boldsymbol{k}_0^3$	23.0	400.00	2.43
$\boldsymbol{k}_0^4$	23.0	200.00	4.86
$\boldsymbol{k}_0^5$	23.0	400.00	1.22
$\boldsymbol{k}_0^6$	12.0	400.00	1.22
$\boldsymbol{k}_0^7$	12.0	100.00	1.22

Table 5.6: Results $\boldsymbol{k}_{\text{opt}}^i$ for the identification of thermal model parameters alongside the remaining squared error in temperature using model 1 and experiment no. 1.

Optimal set	α_{exp}	κ_{therm}	c_0	f^θ
$\boldsymbol{k}_{\text{opt}}^1$	25.40	91.19	3.10	9.61
$\boldsymbol{k}_{\text{opt}}^2$	25.40	91.19	3.10	9.61
$\boldsymbol{k}_{\text{opt}}^3$	25.40	91.19	3.10	9.61
$\boldsymbol{k}_{\text{opt}}^4$	25.40	91.19	3.10	9.61
$\boldsymbol{k}_{\text{opt}}^5$	25.40	91.19	3.10	9.61
$\boldsymbol{k}_{\text{opt}}^6$	25.40	91.19	3.10	9.61
$\boldsymbol{k}_{\text{opt}}^7$	25.40	91.19	3.10	9.61

Taking a closer look at the optimal material response, a good fit of simulation results to experimental data is again obtained as indicated by Figures 5.10 and 5.11. More precisely speaking, Figure 5.10 shows that the remaining error in temperature change does not cluster around any specific point in space and is rather homogeneously distributed. Moreover, Figure 5.11 demonstrates for a single material point (midpoint of specimen) that the remaining error in temperature is also uniform in time. The obtained model parameters therefore lead to a very good representation of the experimental data at hand for both displacement and temperature field, passing the verification as introduced in Section 2.9.1. It is worth mentioning at this point that $\boldsymbol{k}_0^1$ represents the literature values for the parameters of AW6016, see [31], which can be used to describe certain purely

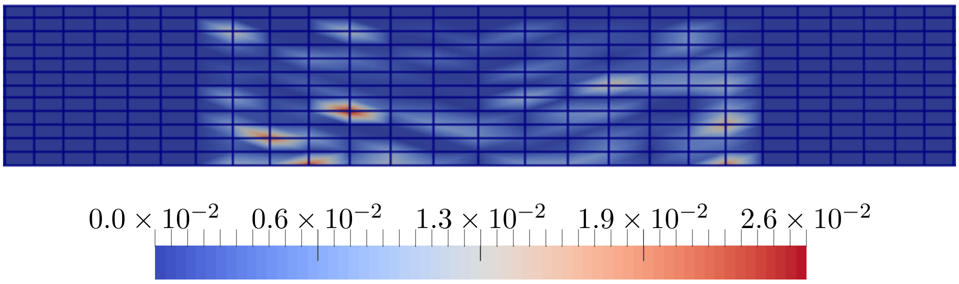

Figure 5.10: Remaining nodal contribution to the thermal (temperature) part of the objective function at time $t = 140$ s using model 1 and experiment no. 1.

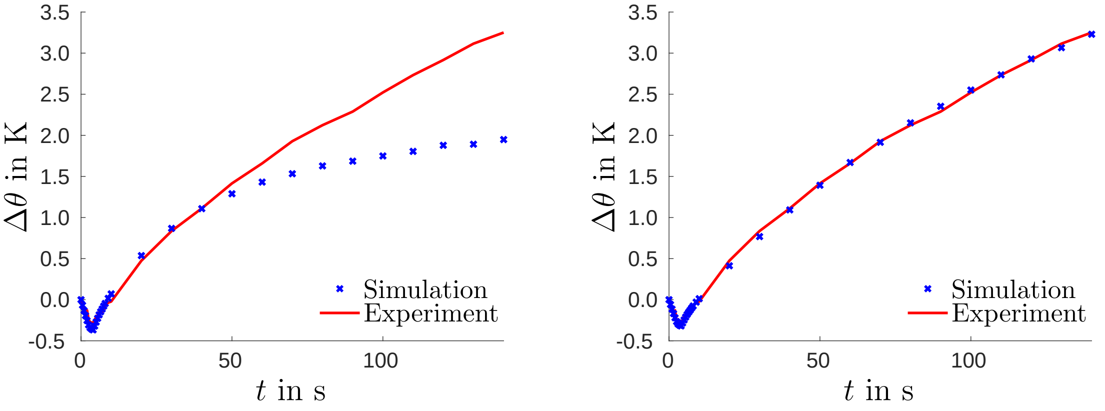

(a) Results based on initial guess $\boldsymbol{k}_0^1$, i.e. literature values.

(b) Results obtained with optimal parameter set.

Figure 5.11: Local temperature-time relation evaluated at the midpoint of the specimen using model 1 and experiment no. 1.

thermal boundary value problems, e.g. a simple heat conductor. Comparing the literature values against the obtained parameter set, a significant difference is revealed which indicates that model 1, together with the parameter set obtained within this section is not able to represent a simple heat conductor and a simple tension test with self-heating equally well. In conclusion, model 1 and the associated optimal parameter set of this section can be verified, but not be validated. One reason for the failed validation most probably lies within the model formulation itself, i.e. the predicted dissipation which represents the main heat source for the boundary problem at hand. Models with different dissipation will lead to different optimal model parameters as was explained in Section 4.2.1 and as is further investigated in the following section.

5.4 Model dependency

With the general identifiability of the classic thermal model parameters on the basis of a simple tension test being ensured, this section concentrates on the effect different model formulations have on the result of such an identification. The aim of this section is to answer the questions

- How do the different model formulations presented in Chapter 4 affect the optimal values of the model parameters?
- Is a (locally) unique fit of the thermal model parameters possible if β is included as an additional unknown?
- What kind of experimental data is required to ensure identifiability of all four thermal model parameters?

Hence, the two constitutive models are compared in the context of a parameter identification as a proof of concept that even seemingly small changes to the model formulation may have a significant impact on the optimal parameter values. The identifications are performed twice for each model, using data from experiment no. 1 (monotonous loading) and no. 2 (loading-unloading-cooling), see Table 3.1, to analyse identifiability. It is worth mentioning that experiment no. 1 will henceforth be referred to as "without cooling" and experiment no. 2 as "with cooling". To ensure comparability of the models, the linear hardening part of model 1 is omitted, rendering its mechanical response nearly identical to that of model 2, see Remark 4.4. The parameter identification process, again, follows the successive scheme presented above, identifying first the elastic, then the plastic and finally the thermal model parameters.

5.4.1 Experiment without cooling

Data of the experiment without cooling, i.e. experiment no. 1, is used for the following identification which is split into three parts. Results for model 1 and model 2 are presented side by side for each step of the process.

5.4.1.1 Elastic model parameters

The experimental reaction force of up to two seconds is prescribed as load to ensure that the elastic parameters are identified on the basis of purely elastic experimental data, see Figure 5.12. Only the error in displacements is considered for this part and the missing weighting factors are set to $W_x^{\mathrm{u}} = 1$ and $W_y^{\mathrm{u}} = 1$. The initial guess as well as the resulting model parameters of model 1 and model 2 are displayed in Table 5.7. The optimal elastic model parameters for model 1 and model 2 are identical, since both models share the same purely elastic material behaviour. Regarding the quality of the fit, Figure 5.14 exemplarily shows that the remaining error $f = f^{\mathrm{u}}$ is distributed

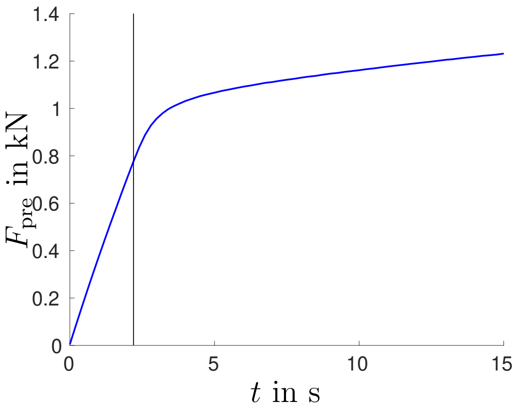

Figure 5.12: Prescribed force F_{pre} over time. Black, vertical line indicates end time $t_{\text{end}}^{\text{el}} = 2.0$ s for identification of elastic parameters on the basis of the experiment without cooling.

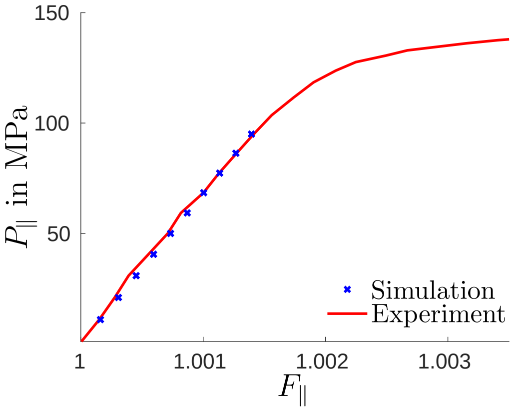

Figure 5.13: Local stress-strain relation of experiment without cooling and of simulation with optimal elastic parameter set, evaluated at the midpoint of the specimen. Elastic response is identical for model 1 and model 2.

Table 5.7: Initial and obtained values for elastic model parameters on the basis of the experiment without cooling.

Model parameter	E in MPa	ν
Initial guess	60000	0.30
Optimal value - Model 1	67913	0.35
Optimal value - Model 2	67913	0.35

rather homogeneously over the area which was considered for the identification. The distribution of the remaining deviation between experimental data and simulation results over time of a single, representative node can be seen in Figure 5.13. The two Figures suggest a good fit of either model to the elastic material behaviour.

5.4.1.2 Plastic model parameters

With the elastic model parameters at hand, the plastic model parameters are identified in a second step by using experimental data up to the end of the experiment without cooling, i.e. up to 140 s. The prescribed load path is displayed in Figure 5.15. Only the error in displacements is considered and the weighting factors are set to $W_x^{\text{u}} = 5$ and $W_y^{\text{u}} = 1$. The identification process is started with the initial guesses from Table 5.8 yielding the optimal model parameters displayed in the same Table. Remaining deviations to the experimental data are sufficiently small, as Figures 5.16 and 5.17 indicate. Thus, the fit of the two models to the plastic material behaviour appears to be acceptably accurate.

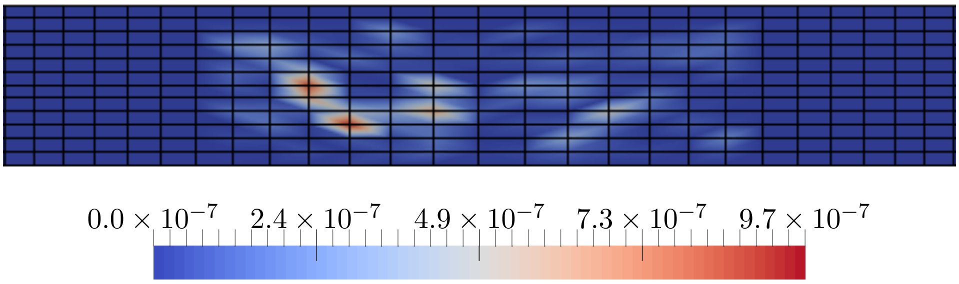

Figure 5.14: Remaining nodal contribution to the mechanical (displacement) part of the objective function f^{u} at time $t = 2.0$ s using data from the experiment without cooling. The remaining error is the identical for model 1 and model 2 since the elastic response is identical.

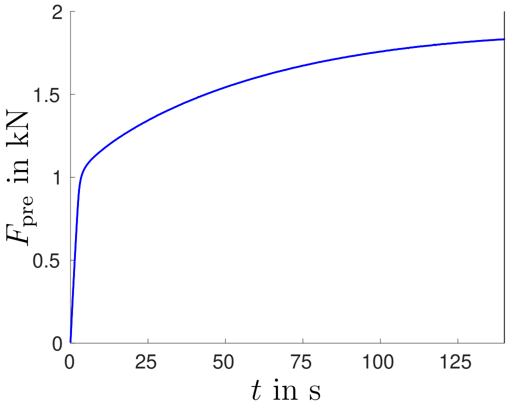

Figure 5.15: Prescribed force F_{pre} over time. Vertical, black line indicates end time $t_{\mathrm{end}}^{\mathrm{pl}} = 140.0$ s for identification of plastic parameters on the basis of the experiment without cooling.

Table 5.8: Initial and obtained values for plastic model parameters on the basis of the experiment without cooling.

Model parameter	M_{y_0} in MPa	M_{y_∞} in MPa	H_{exp}	F
Initial guess	140.00	290.00	15.00	0.50
Optimal value - Model 1	131.13	297.97	10.62	0.37
Optimal value - Model 2	130.38	295.60	10.92	0.37

Independent of the fit, a closer look at the obtained optimal plastic model parameters in Table 5.8 and the material response in Figure 5.17 shows that the two models predict an almost identical mechanical material response for the almost same set of model parameters. Thus, the assumption made in Remark 4.4, stating that the mechanical

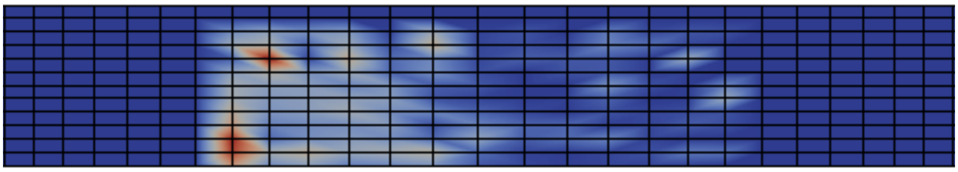

(a) Model 1.

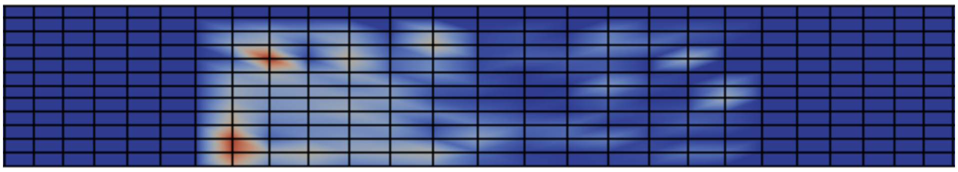

(b) Model 2.

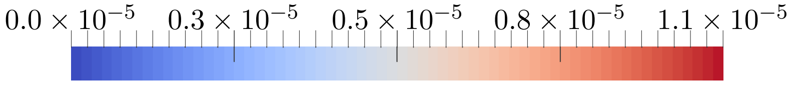

Figure 5.16: Remaining nodal contribution to the mechanical (displacement) part of the objective function f^{u} at time $t = 140.0$ s using data from the experiment without cooling.

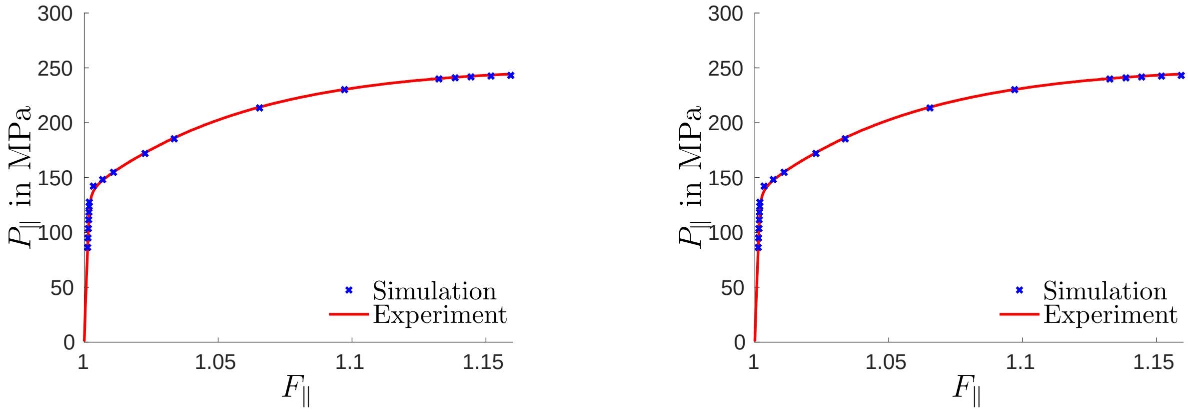

(a) Model 1. (b) Model 2.

Figure 5.17: Local stress-strain relation of experiment without cooling and of simulation with optimal plastic parameter set, evaluated at the midpoint of the specimen.

parts of the two models are comparable for large deformation, appears to be valid for the boundary value problem considered.

5.4.1.3 Thermal model parameters

Finally, the thermal model parameters of each model can be fitted to the temperature data of the experiment without cooling using data up to the time $t = 140$ s. The identification is started from several initial guesses, see Table 5.9, to investigate the uniqueness of the solution within a certain area of the parameter space, since a general statement about the correlation of the four thermal model parameters in Section 4.2 was not possible. Bounds for parameter β in model 2 are set in accordance with Equation (4.25) to $0 \leq \beta \leq 6.92$. Comparing the optimised material response of each model, the predicted temperature evolution is almost identical for all optimised model parameter sets, and remaining errors per node are rather small for both models, as is indicated in Figures 5.18 and 5.19. However, a closer look at the obtained parameter values for each model reveals significant differences.

Table 5.9: Initial values for thermal model parameters for model 1 and model 2 and literature values.

Initial set	α_{exp} in 10^{-6}/K	κ_{therm} in mW/mm K	c_0 in mJ/mm^3 K	β
$\boldsymbol{k}_{\text{A}}$	23.00	200.00	2.43	1.00
$\boldsymbol{k}_{\text{B}}$	23.00	200.00	2.43	0.10
$\boldsymbol{k}_{\text{C}}$	23.00	200.00	2.43	0.50
$\boldsymbol{k}_{\text{D}}$	12.00	400.00	1.22	0.50
Literature value	23.00	200.00	2.43	-

Model 1 The optimal model parameter sets of model 1 differ significantly while leading to the same remaining error value, as can be seen in Table 5.10. Thus, the inverse problem at hand has several solutions close to each other, and the assumption arises that a whole valley of solutions exists for the specific inverse problem at hand. Either way, a dependency between scaling parameter β and the remaining thermal model parameters becomes evident for this combination of model and experimental data. Although a general statement was not possible in Section 4.2, the specific thermal boundary conditions for the BVP at hand eventually allow an interpretation of the correlation between β, α_{exp}, κ_{therm} and c_0. It was already shown in Section 5.3 that the identification of thermal model parameters on the basis of an experiment without cooling, i.e. with monotonic loading, yields a unique (at least locally) result if a standard formulation of model 1 is used. The main difference between such a standard formulation and the non-standard formulation used within this section is parameter β. Whereas the dissipation of a standard model only depends on the mechanical model parameters, the dissipation rate density can still be scaled for the non-standard model without affecting the mechanical response, as was

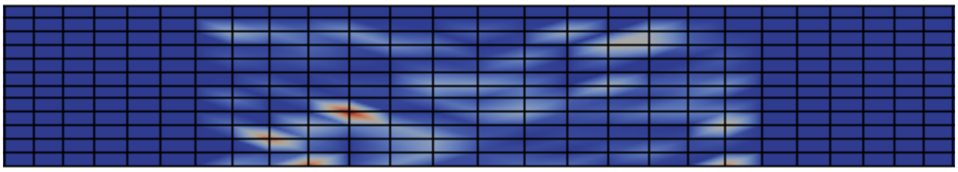

(a) Model 1. Distribution is almost identical for all optimal parameter sets.

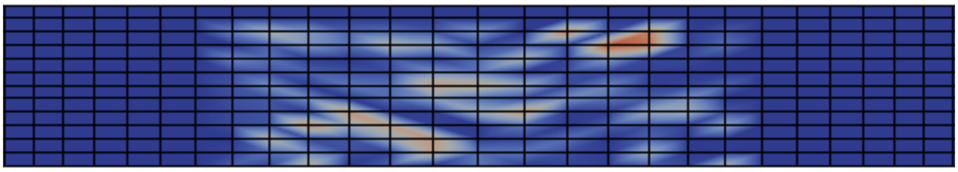

(b) Model 2.

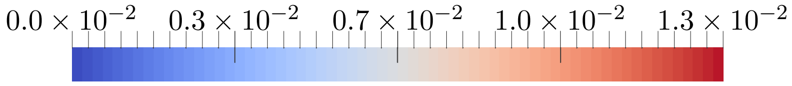

Figure 5.18: Remaining nodal contribution to the thermal (temperature) part of the objective function f^θ at time $t = 140.0$ s using data of the experiment without cooling.

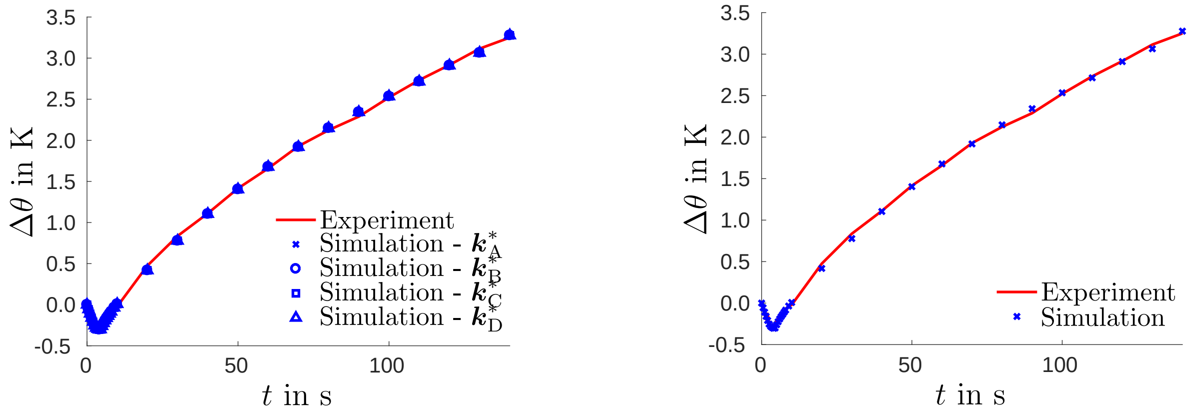

(a) Model 1.

(b) Model 2.

Figure 5.19: Local temperature-time relation of experiment without cooling and of simulations with optimal thermal parameter sets, evaluated at the midpoint of the specimen.

Table 5.10: Obtained values for thermal model parameters and remaining error contribution to the objective function f^θ for model 1 on the basis of the experiment without cooling.

Optimal set	α_{exp} in 10^{-6}/K	κ_{therm} in mW/mm K	c_0 in mJ/mm^3 K	β	f^θ
$\boldsymbol{k}^*_{\mathrm{A}}$	28.74	99.32	3.68	1.13	8.76
$\boldsymbol{k}^*_{\mathrm{B}}$	37.06	128.15	4.68	1.46	8.76
$\boldsymbol{k}^*_{\mathrm{C}}$	30.57	105.65	3.90	1.21	8.76
$\boldsymbol{k}^*_{\mathrm{D}}$	18.97	65.49	2.46	0.75	8.76

explained in Section 4.1. That is to say that β affects the dissipation of all time steps for model 1 alike by simply shifting the quantity of dissipated energy, as can be seen in Figure 5.20. This constant difference in available heat is simply compensated by an adaptation of the other thermal model parameters, all of which are featured linearly in one of the active addends within the balance of energy (4.20) for model 1. The following example is considered: If twice as much energy is transformed to heat at each time step, the heat capacity must be twice as high to ensure that the same (optimal) temperature is reached. The thermal conduction must be twice as high in order to transport twice as much heat towards both ends of the specimen where it can leave the specimen (due to the specific thermal boundary conditions at hand). By considering the balance of energy in Equation (4.20), it follows that the heat expansion coefficient, which is featured in the addend responsible for the Gough-Joule effect, must also be twice as high for such a case. This example illustrates that the dependency of parameters mainly occurs due to the specific BVP at hand, where the predicted dissipation of model 1 is constant for all plastic time steps. Thus, an experimental part with a different rate of dissipation should stabilise the identification process, but the influence of the rather short elastic part of the experiment at hand is apparently not enough. Accordingly, the ratio of $\alpha_{\mathrm{exp}}/\beta$, $\kappa_{\mathrm{therm}}/\beta$ and c_0/β should be constant if the amount of dissipated energy scales linearly in β. This is the case for model 1 and the results underline the explanation above.

Apart from the dependency of the parameters, it is not possible to retrieve a thermal model parameter set for model 1 which is close to the literature values, see Table 5.9. The four thermal model parameters of model 1 are therefore neither identifiable on the basis of a simple tension test nor do they pass a simple validation, i.e. they cannot be used to predict different boundary value problems equally well, e.g. plastic heating and a simple heat conductor.

Model 2 All obtained solutions for model 2 are numerically identical, see Table 5.11, suggesting that a (locally) unique optimum has been found and that no dependency between the thermal parameters exists for this combination of model and experiment. This appears to be reasonable due to the difference to model 1 regarding how β affects

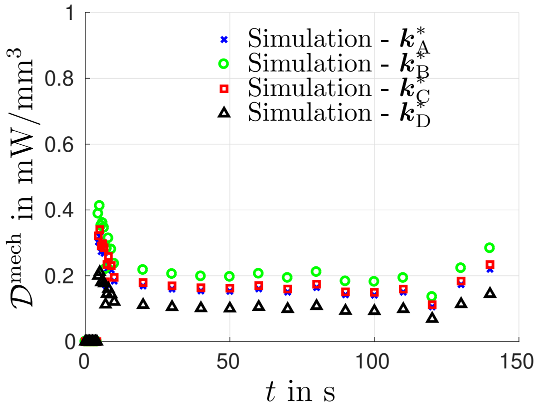

(a) Model 1.

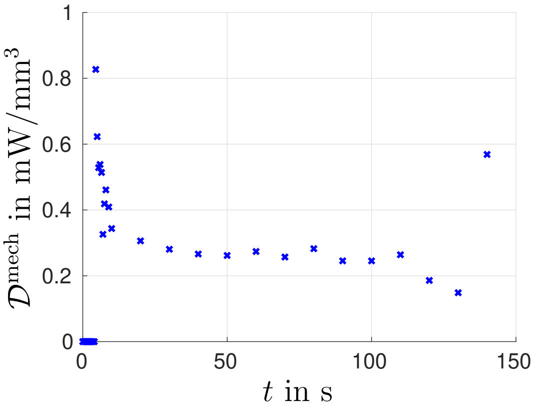

(b) Model 2.

Figure 5.20: Predicted local dissipation contribution during simulations of the experiment without cooling with optimal thermal parameter sets evaluated at midpoint of the specimen and at output time steps (subset of all time steps). Amount of dissipated energy density depends on applied load, i.e. the difference of applied force between two load steps. Due to the noise in the prescribed, experimental reaction force, some time steps have a larger or smaller increase in force than an ideal, smooth load path would generate. This leads to jumps in the dissipation rate density, which would otherwise represent a more smooth function for the case at hand.

the dissipation. The resulting format of the dissipation, see Equations (4.21) and (4.22), shows that β leads to a constant shift of dissipation for model 1, but scales the dissipation load state dependent for model 2. Thus, if only a particular functional relation between strain and dissipation is favourable regarding the plastic heating of the specimen, only one optimum exists.

The values of the optimal set, however, do also not resemble the literature values in Table 5.9 and it can be concluded that an experiment with monotonous loading alone may hold enough information for a unique and verifiable fit of the four thermal model parameters of model 2, but that the obtained model parameters are not valid, i.e. they cannot be used to predict different boundary value problems equally well.

Table 5.11: Obtained values for thermal model parameters and remaining error contribution to the objective function f^θ for model 2 on the basis of the experiment without cooling.

Optimal set	α_{exp} in 10^{-6}/K	κ_{therm} in mW/mm K	c_0 in mJ/mm^3 K	β	f^θ
$\boldsymbol{k}^*_{\mathrm{A}}$	53.74	166.53	6.31	2.29	8.63
$\boldsymbol{k}^*_{\mathrm{B}}$	53.74	166.53	6.31	2.29	8.63
$\boldsymbol{k}^*_{\mathrm{C}}$	53.74	166.53	6.31	2.29	8.63
$\boldsymbol{k}^*_{\mathrm{D}}$	53.74	166.53	6.31	2.29	8.63

5.4.2 Experiment with cooling

Data of the experiment which includes a stage of cooling down to ambient temperature is used for the following identification. Results for model 1 and model 2 are presented side by side for each step of the identification process.

5.4.2.1 Elastic model parameters

The experimental reaction force of up to two seconds is prescribed as load to ensure that the elastic parameters are identified on the basis of purely elastic experimental data, see Figure 5.21. Only the error in displacements $f = f^{\mathrm{u}}$ is considered for this part and the weighting factors are set to $W_x^{\mathrm{u}} = 1$ and $W_y^{\mathrm{u}} = 1$. Initial guess as well as the resulting model parameters of model 1 and model 2 are displayed in Table 5.12. The optimal elastic model parameters for model 1 and model 2 are again identical, since both models share the same purely elastic material behaviour. Figure 5.23 shows that the remaining

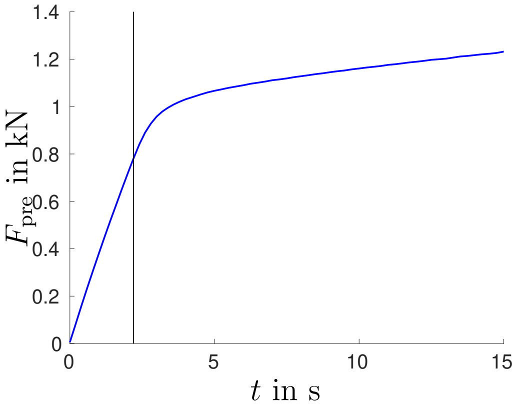

Figure 5.21: Prescribed force F_{pre} over time. Vertical, black line indicates end time $t_{\mathrm{end}}^{\mathrm{el}} = 2.0$ s for identification of elastic parameters on the basis of the experiment with cooling.

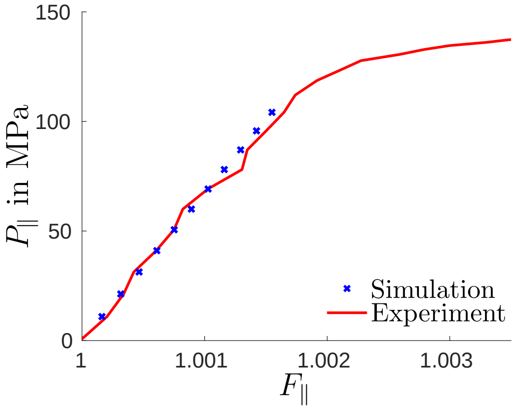

Figure 5.22: Local stress-strain relation of experiment with cooling and of simulation with optimal elastic parameter set, evaluated at the midpoint of the specimen. Elastic response is identical for model 1 and model 2.

Table 5.12: Initial and obtained values for elastic model parameters on the basis of the experiment with cooling.

Model parameter	E in MPa	ν
Initial guess	60000	0.30
Optimal value – model 1	67026	0.36
Optimal value – model 2	67026	0.36

error $f = f^{\mathrm{u}}$ is distributed rather homogeneously over the area which was considered for the identification, similar to the identification on the basis of the experiment without cooling. The distribution of the remaining error over time of a single, representative node can be seen in Figure 5.22. Both figures suggest a good fit of either model to the elastic material behaviour of the experiment with cooling.

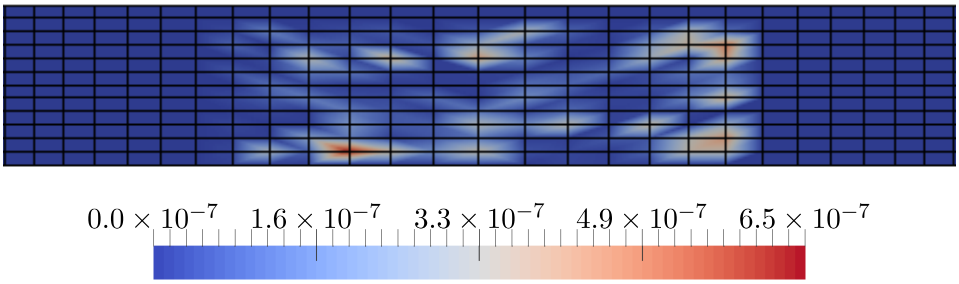

Figure 5.23: Remaining nodal contribution to the mechanical (displacement) part of the objective function f^{u} at time $t = 2.0$ s using data of the experiment with cooling. The remaining error is the same for model 1 and model 2 since the elastic response is identical.

5.4.2.2 Plastic model parameters

The plastic parameters are identified on the basis of experimental data up to 144 s, taking into account the unloading of the specimen. Figure 5.24 shows the prescribed load path of the experimental reaction force. Only the error in displacements is considered and the weighting factors are set to $W_x^{\mathrm{u}} = 5$ and $W_y^{\mathrm{u}} = 1$. Starting from the parameter sets identified on the basis of the experiment without cooling, the identification yields the optimised parameters depicted in Table 5.13. Remaining deviations from the

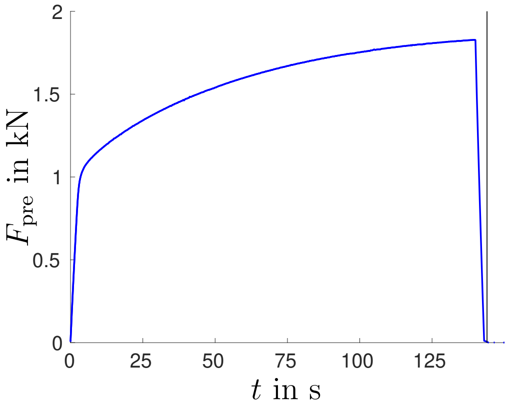

Figure 5.24: Prescribed force F_{pre} over time. Vertical, black line indicates end time $t_{\mathrm{end}}^{\mathrm{pl}} = 144.0$ s for identification of plastic parameters on the basis of the experiment with cooling.

Table 5.13: Initial and obtained values for plastic model parameters on the basis of the experiment with cooling.

Model parameter	M_{y_0} in MPa	M_{y_∞} in MPa	H_{exp}	F
Initial guess	131.13	297.97	10.62	0.37
Optimal value - Model 1	129.27	293.38	10.82	0.37
Optimal value - Model 2	129.28	293.36	10.97	0.37

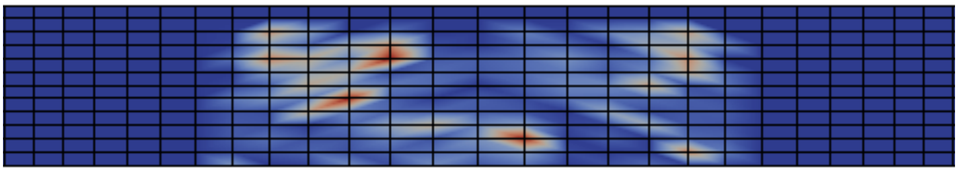

(a) Model 1.

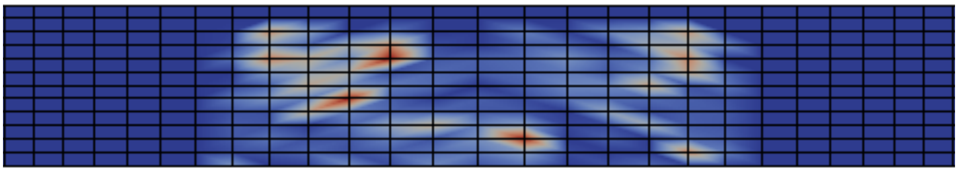

(b) Model 2.

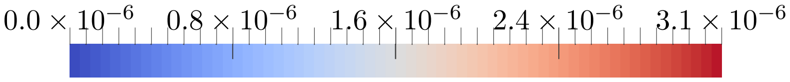

Figure 5.25: Remaining nodal contribution to the mechanical (displacement) part of the objective function f^{u} at time $t = 140.0$ s using data of the experiment with cooling.

experimental data are sufficiently small as Figures 5.25 and 5.26 indicate. Thus, both models have an almost identical and accurate fit to the elasto-plastic material behaviour, underlining once again the similarities of the two chosen model formulations with respect to the mechanical part. Figure 5.26 furthermore shows that both models also fit the unloading stage of the experiment rather well, thereby suggesting that the material did not experience a significant degradation of elastic material properties during the experiment. Such a degradation would otherwise be an indicator for damage effects,

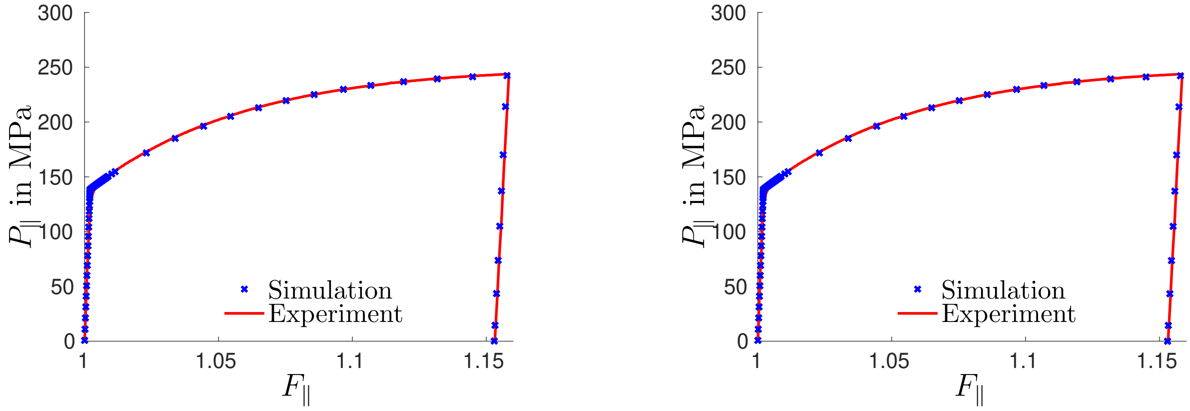

(a) Model 1.

(b) Model 2.

Figure 5.26: Local stress-strain relation of the experiment with cooling and of simulation with optimal plastic parameter set, evaluated at the midpoint of the specimen.

and the fact that none are observed support the decision to neglect damage effects in the constitutive models at hand (at least to a certain degree).

5.4.2.3 Thermal model parameters

Finally, the thermal model parameters of each model are fitted to the temperature data of the experiment with cooling by using data including the cooling-down phase up to time $t = 400$ s. The initial guesses from Table 5.9 are used again to see whether the dependency between the four thermal model parameters of model 1 shown in Section 5.4.1.3 vanishes for the enhanced set of experimental data which includes the cooling of the specimen. The rough grid search approach furthermore shows whether it is possible to retrieve a parameter set that is sufficiently close to literature values, thereby indicating a valid parameter set. Bounds for the parameter β in model 2 are set in accordance with Equation (4.25) to $0 \leq \beta \leq 6.93$.

Model 1 All of the performed identifications converge towards the same optimum, see Table 5.14. Thus, the additional information of the cooling process stabilises the identification process for this model, removing the dependency described in Section 5.4.1.3 which occurred due to an incompleteness of data. The resulting, optimal material response of model 1, however, still exhibits large remaining errors, see Figure 5.27. Even though the remaining deviation from experimental data is distributed rather homogeneously in space, the comparison of experimental data and the optimal thermal material response over time in Figure 5.29 reveals a substantial mismatch. It therefore appears impossible to predict the heating as well as the cooling of a specimen adequately with the associated plasticity model and a single set of model parameters within the range of temperature changes considered.

Table 5.14: Obtained values for thermal model parameters and remaining error contribution to the objective function f^θ for model 1 on the basis of the experiment with cooling.

Optimal set	α_{exp} in 10^{-6}/K	κ_{therm} in mW/mm K	c_0 in mJ/mm^3 K	β	f^θ
$\boldsymbol{k}^*_{\text{A}}$	421.56	2653.29	$\ll 1$	18.92	211.63
$\boldsymbol{k}^*_{\text{B}}$	421.40	2652.13	$\ll 1$	18.91	211.63
$\boldsymbol{k}^*_{\text{C}}$	421.35	2651.07	$\ll 1$	18.90	211.63
$\boldsymbol{k}^*_{\text{D}}$	421.47	2652.10	$\ll 1$	18.91	211.63

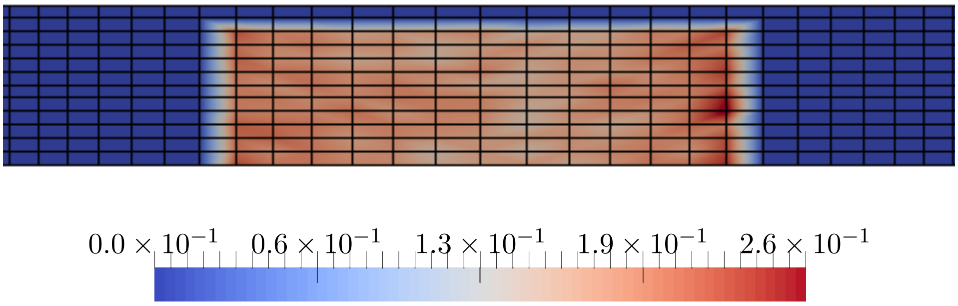

Figure 5.27: Remaining nodal contribution to the thermal (temperature) part of the objective function f^θ at time $t = 140.0$ s using data of the experiment with cooling and constitutive model 1.

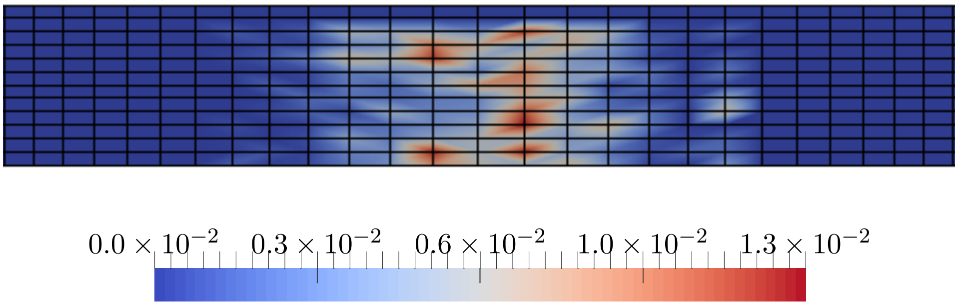

Figure 5.28: Remaining nodal contribution to the thermal (temperature) part of the objective function f^θ at time $t = 140.0$ s using data of the experiment with cooling and constitutive model 2.

Model 2 All initial guesses lead to the same optimal set of thermal model parameters, indicating that a (locally) unique optimum is obtained for the case at hand. The remaining error per node, as exemplarily depicted in Figure 5.28, is again rather low and statistically distributed. A closer look at the temperature evolution over time of

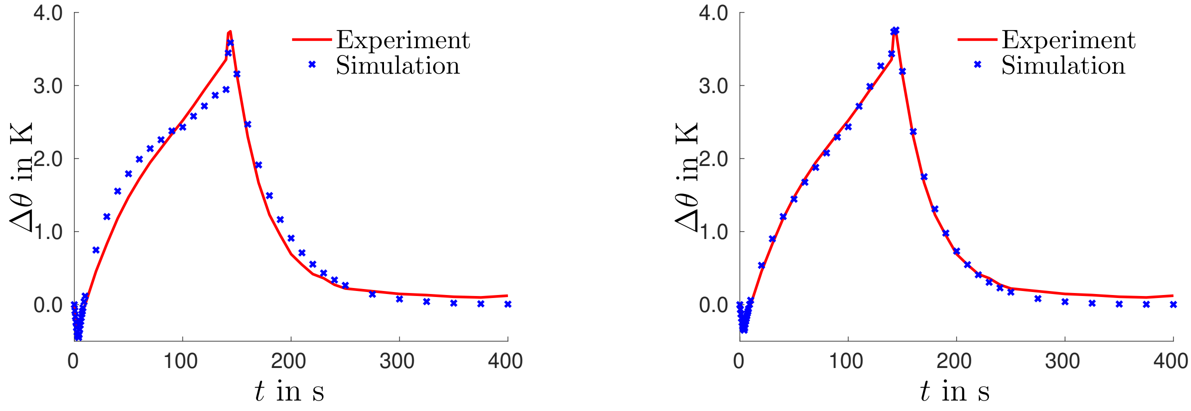

(a) Model 1. (b) Model 2.

Figure 5.29: Local temperature-time relation of experiment with cooling and of simulations with optimal thermal parameter set, evaluated at the midpoint of the specimen.

Table 5.15: Obtained values for thermal model parameters and remaining error contribution to the objective function f^θ for model 2 on the basis of the experiment with cooling.

Optimal set	α_{exp} in 10^{-6}/K	κ_{therm} in mW/mm K	c_0 in mJ/mm^3 K	β	f^θ
$\boldsymbol{k}_{\text{A}}^*$	19.83	189.89	2.21	0.81	26.73
$\boldsymbol{k}_{\text{B}}^*$	19.83	189.89	2.21	0.81	26.73
$\boldsymbol{k}_{\text{C}}^*$	19.83	189.89	2.21	0.81	26.73
$\boldsymbol{k}_{\text{D}}^*$	19.83	189.89	2.21	0.81	26.73

a representative, single node in Figure 5.29 reveals a very precise fit of computed to experimental data. Thus, model 2 appears to be capable of predicting plastic heating and thermal cooling effects similarly well with a single set of model parameters. Moreover, this optimal set is very close to the literature values in Table 5.9 with a relative deviation of

$$\frac{\alpha_{\text{exp}}^{\text{lit}} - \alpha_{\text{exp}}^{\text{opt}}}{\alpha_{\text{exp}}^{\text{lit}}} = 13.78\%\,, \tag{5.1}$$

$$\frac{\kappa_{\text{therm}}^{\text{lit}} - \kappa_{\text{therm}}^{\text{opt}}}{\kappa_{\text{therm}}^{\text{lit}}} = 5.06\%\,, \tag{5.2}$$

$$\frac{c_0^{\text{lit}} - c_0^{\text{opt}}}{c_0^{\text{lit}}} = 9.05\% \tag{5.3}$$

which is not too uncommon for model parameters. The elastic parameters E and ν, for example, exhibit a relative deviation of 5% and 9% with respect to literature values for aluminium. The obtained thermal model parameters for model 2 could therefore probably also be used to predict different boundary value problems such as a rigid heat conductor. Accordingly, an experiment with loading-unloading-cooling holds sufficient information for a unique fit, and model 2 furthermore yields optimal parameters which appear to pass a first and very simple validation attempt. Of course, for the parameter set to be truly validated, comparisons against further and possibly more complex boundary value problems should be made. This, however, is out of scope and not the aim of the thesis at hand which is mainly concerned with general identifiability of parameters.

It may appear odd that a similar set has not already been found for the monotonous loading case in Section 5.4.1 since both parameter sets lead to an apparently equally good fit of the heating phase. A comparison of the remaining error as described by the objective function value f^θ would give a closer insight to the quality of the fit, but such a direct comparison is not valid since the number of time steps is not equal. Thus, the error function is evaluated once again, comparing data from the experiment including cooling with the computed data of two simulations which both end at 140 s, just prior to unloading. One simulation uses the optimal thermal parameters obtained in Section 5.4.1.3 resulting in a remaining error of $f^\theta = 5.16$. The second simulation uses the optimal thermal parameters from this section leading to a remaining error of $f^\theta = 12.85$. It shows that the parameter set of this section may be able to describe heating and cooling alike. At the trade-off, however, that a slightly less perfect fit may be obtained than might be possible if only one phenomenon was considered at a time. The trade-off itself is very small and the fit nevertheless still very precise as the previously mentioned figures show, so that an accurate identification of the thermal parameters is possible with model 2 in combination with an experiment with cooling.

5.4.3 General identifiability of the heat equation

The heat equation, which is based on the balance of energy, is the main equation on which the identification of thermal model parameters is based due to the split of the identification process into an elastic, plastic and thermal part. Depending on the boundary value problem considered, it can take slightly different forms, e.g.

$$c_0\,\dot{\theta} = -\,\nabla_{\boldsymbol{X}} \cdot \boldsymbol{Q}\,(\bullet\,;\;\kappa_{\text{therm}}) \qquad \wedge \qquad \boldsymbol{n} \cdot \boldsymbol{q} = -\,\alpha_{\text{con}}\,\left[\theta^{\text{M}} - \theta\right] \tag{5.4}$$

for a rigid body with transient change in temperatures and subject to convection at its boundary. Due to the specific definition of the heat flux, which is linear in the model parameter κ_{therm}, the model parameters of all addends can be factorised. Equation (5.4) can therefore be rewritten as

$$c_0\,\dot{\theta} = -\,\kappa_{\text{therm}}\,\nabla_{\boldsymbol{X}} \cdot \bar{\boldsymbol{Q}} \qquad \wedge \qquad \kappa_{\text{therm}}\,\boldsymbol{n} \cdot \bar{\boldsymbol{q}} = -\,\alpha_{\text{con}}\,\left[\theta^{\text{M}} - \theta\right] \tag{5.5}$$

$$\Leftrightarrow \quad \dot{\theta} = -\,\frac{\kappa_{\text{therm}}}{c_0}\,\nabla_{\boldsymbol{X}} \cdot \bar{\boldsymbol{Q}} \qquad \wedge \qquad \frac{\kappa_{\text{therm}}}{c_0}\,\boldsymbol{n} \cdot \boldsymbol{q} = -\,\frac{\alpha_{\text{con}}}{c_0}\,\left[\theta^{\text{M}} - \theta\right]\,, \tag{5.6}$$

showing that only a subset of all parameters can be uniquely identified. This is true as long as the main set of equations consists only of addends with different model parameters which can be factorised. Hence, adding different features to the experiment, e.g. the effect of plastic heat sources $\mathcal{D}^{\mathrm{mech}}(\bullet\,;\ \beta)$ where the new unknown model parameter β can be factorised as is the case for classic models with associated evolution equations ($\mathcal{D}^{\mathrm{mech}} = \beta\,\bar{\mathcal{D}}^{\mathrm{mech}}$, see Equation (4.21)), changes nothing at the intrinsic overparametrisation of the heat equation. This overparametrisation is only resolved if at least one thermal model parameter is known a priori, or if the model parameter cannot be factorised in at least one addend as is the case for model 2, see Equation (4.22).
It is worth mentioning that the identifiability of a set of parameters is not only related to this model specific property but also to the experiment. If one or more parameters are not addressed strong enough (or not at all) by the experimental data, the value of the respective parameters can take arbitrary values, thereby leading to infinitely many non-isolated minima. This is, for example, the case for the identification performed with model 1 and the experiment without cooling in Section 5.4.1.3. The intrinsic overparametrisation is resolved due to the a priori estimation of the heat conduction coefficients α_{con}. Nevertheless, a dependency of model parameters is detected since the data of an experiment without cooling appears to insufficiently address the part of the heat equation related to the heat conduction coefficients.

5.5 Identifiability of thermal boundary coefficients

In the previous sections the identifiability of the three classic and one additional thermal model parameter has been analysed, based on experimental data of a simple tension test. However, two further model parameters have so far been ignored, i.e. the heat conduction and heat convection coefficient which define the thermal boundary conditions. It was already mentioned in Section 5.2.2 that the value for these boundary coefficients must be generally considered unknown since common testing devices usually cannot guarantee isothermal or adiabatic bounds. Assumptions regarding these heat transfer coefficients can be made for certain cases, see Section 5.2.2, but they are unknown in general. This leads to the questions of identifiability and sensitivity of the thermal boundary coefficients alongside the actual thermal model parameters. To be more precise, related fundamental questions are

- Is a (locally) unique fit of thermal model parameters and boundary coefficients possible on the basis of full field temperature measurements?
- How sensitive are the resulting parameter values with respect to the (measured) boundary temperatures required for Newton's law of cooling?

In order to answer these questions, the results of several parameter identifications are shown within this section, whereas the main focus lies on the identifiability of heat conduction and heat convection coefficients alongside the unknown thermal model parameters. At first, however, the optimal mechanical parameters for the underlying problem, as well as a reference solution for the optimal thermal model parameters are introduced. The actual identifiability of the whole set of unknown model parameters is shown afterwards by using a grid search approach. This is followed by a sensitivity analysis of the optimal parameter values with respect to the external, prescribed temperatures. Finally, the possibility to optimise only a subset of the thermal model parameters is explored and the result is compared against the fully optimised parameter set. It is worth mentioning that data from experiment no. 3 (loading-unloading-cooling, see Table 3.1) is used for the following identifications. Furthermore, only model 2 is considered, due to its ability to represent the material at hand, see Section 5.4.

5.5.1 Mechanical model parameters

The mechanical parameters are identified in two steps, identifying first the elastic model parameters (Young's Modulus E and Poisson's ratio ν) and subsequently the plastic model parameters (initial Yield limit M_{y_0}, non-linear hardening parameters M_{y_∞} and H_{exp} as well as the one independent yield surface parameter F. The obtained parameter values are summarised in Table 5.16. Furthermore, Figure 5.30 shows the resulting fit between simulation and experiment.

Table 5.16: Optimal values for mechanical model parameters using model 2 and experiment no. 3.

Model parameter	E in MPa	ν	M_{y_0} in MPa	M_{y_∞} in MPa	H_{exp}	F
Optimal value	68396.66	0.34	128.92	292.73	10.87	0.35

5.5.2 Reference solution with prescribed boundary coefficients

Before optimising the thermal boundary coefficients along with the thermal model parameters, a reference solution with prescribed convection and conduction coefficient is generated. The obtained parameters are subsequently compared to the solution based on the full optimisation in Section 5.5.3.

As was shown in Section 5.4 a locally unique fit of the thermal model parameters (i.e. thermal expansion α_{exp}, heat conduction κ_{therm}, heat capacity c_0 and the parameter scaling latent heat, respectively dissipation β) is possible for the specific combination of model, material and experiment at hand and yields thermal model parameters close to literature values. In the aforementioned section, it was assumed that the boundary coefficients can be prescribed as $\alpha_{\text{con}}^{\text{air}} = 0$ and $\alpha_{\text{con}}^{\text{cl}} = 10^8$ W/[m^2 K] since the heat exchange through the clamping jaws appears to dominate. Prescribing the same values for the heat transfer coefficients, the optimised thermal model parameters of the reference

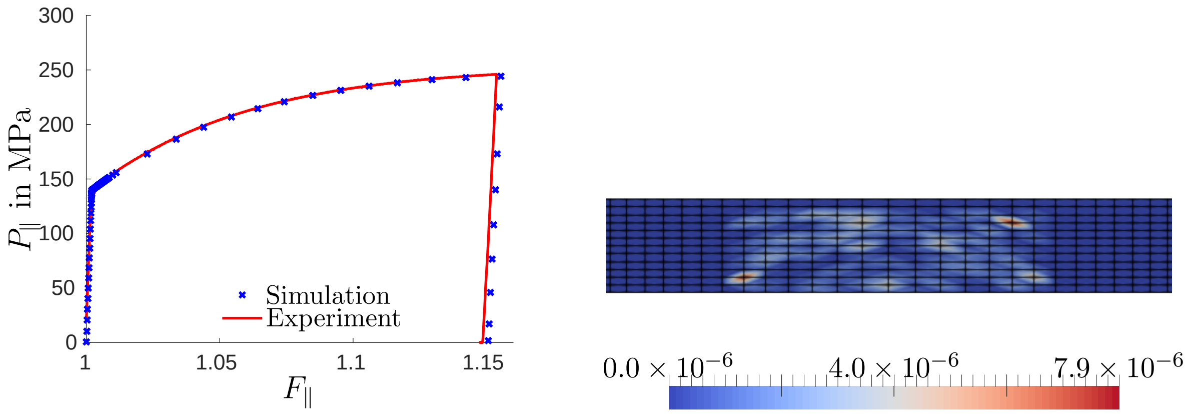

(a) Stress-strain relation of experiment no. 3 and simulation evaluated at midpoint of the specimen.

(b) Remaining nodal contribution to the objective function f^{u} (squared error in relative displacements) at time $t = 140$ s.

Figure 5.30: Optimised mechanical model parameters lead to a very good agreement between simulation based on model 2 and experiment no. 3 with respect to displacement and reaction force data.

solution for the experimental data at hand can be found in Table 5.17. Figure 5.32 shows the fit of the temperature-time relation for a single, representative FE node of the specimen. The overall fit of the material response can later be compared against the material response of the fully optimised parameter set, which would be expected to be even better regarding the remaining error. It is worth noting that the assumptions regarding the heat transfer coefficients are only possible due to the high conductivity of the aluminium alloy under consideration and cannot be transferred to other materials in general.

Table 5.17: Obtained reference values for the thermal model parameters and remaining error contribution to the objective function f^{θ}, based on experiment no. 3. Prescribed values are marked in grey.

Material parameter	α_{exp} 10^{-6}/K	κ_{therm} mW/mm K	c_0 mJ/mm^3 K	β	$\alpha_{\text{con}}^{\text{air}}$ W/m^2 K	$\alpha_{\text{con}}^{\text{cl}}$ W/m^2 K	f^{θ}
Optimal value	20.04	175.17	2.35	0.81	0.00	10^8	20.04

5.5.3 Identification of thermal model parameters and boundary coefficients

It was already mentioned in Section 5.2.2 that the thermal boundary coefficients are generally unknown, so that the set of sought parameters includes the classic thermal model parameters, the model parameter governing dissipation, respectively latent heat, as well as the convection and the conduction coefficients, i.e. $\alpha_{\text{con}}^{\text{air}}$ and $\alpha_{\text{con}}^{\text{cl}}$. The identification is started from ten different initial guesses, see Table 5.18, to ensure that the experimental data holds the required information to find a locally unique parameter set which minimises the objective function. Table 5.19 shows the obtained values which are identical for all ten cases, leading to the remaining error distribution shown in Figure 5.31. While this may not prove (local) uniqueness in a mathematical sense, it nevertheless suggests that no further minima are to be expected within the vicinity of the obtained solution. Thus, the unknown parameters also appear to be independent in the sense that no direct relation (neither linear nor non-linear) connects two or more parameters which would lead to an infinite number of solutions.

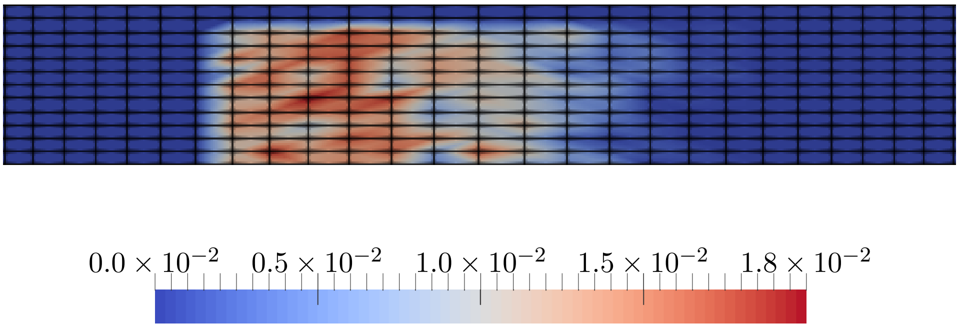

Figure 5.31: Remaining nodal contribution to the objective function f^{θ} (squared error in temperature rise) at time $t = 140$ s using data from experiment no. 3 and the optimised parameter set for model 2, including the boundary coefficients.

5.5.3.1 Comparison with reference solution

So far, it has been shown that the identification of boundary coefficients alongside the thermal model parameters is possible, in principle, on the basis of full field temperature measurements. Comparing the obtained values of such an identification process with the results from the reference solution, which incorporated reasonable values for the boundary coefficients prescribed, shows some significant differences that are worth mentioning.

Subjecting the boundary coefficients to the optimisation process allows the remaining squared error value at the end of the optimisation f^{θ} to drop by approximately 25% from 20.04 to 14.97, see Tables 5.17 and 5.19. The optimal values for the three thermal model parameters α_{exp}, c_0 and β are almost identical and for both cases close to available literature values. Regarding the convection coefficient κ_{therm}, the obtained value lies within the expected range of 2 to 25 $\text{W}/[\text{m}^2\ \text{K}]$ for free convection, see e.g. [30]. There is no expected value for the conduction coefficient, but it is roughly 20 times

Table 5.18: Initial guess for thermal model parameters.

Initial set	α_exp 10^{-6}/K	κ_therm mW/mm K	c_0 mJ/mm^3 K	β	$\alpha_\mathrm{con}^\mathrm{air}$ W/m^2 K	$\alpha_\mathrm{con}^\mathrm{cl}$ W/m^2 K
$\boldsymbol{k}_\mathrm{A}$	19.83	189.89	2.21	0.81	0.10	$4 \cdot 10^5$
$\boldsymbol{k}_\mathrm{B}$	23.00	200.00	2.43	1.00	0.10	$4 \cdot 10^5$
$\boldsymbol{k}_\mathrm{C}$	46.00	200.00	2.43	1.00	0.10	$4 \cdot 10^5$
$\boldsymbol{k}_\mathrm{D}$	23.00	400.00	2.43	1.00	0.10	$4 \cdot 10^5$
$\boldsymbol{k}_\mathrm{E}$	23.00	200.00	4.86	1.00	0.10	$4 \cdot 10^5$
$\boldsymbol{k}_\mathrm{F}$	23.00	200.00	2.43	0.10	0.10	$4 \cdot 10^5$
$\boldsymbol{k}_\mathrm{G}$	23.00	200.00	2.43	1.00	1.00	$4 \cdot 10^5$
$\boldsymbol{k}_\mathrm{H}$	23.00	200.00	2.43	1.00	0.10	$8 \cdot 10^5$
$\boldsymbol{k}_\mathrm{I}$	12.00	400.00	1.22	0.50	0.05	$2 \cdot 10^5$
$\boldsymbol{k}_\mathrm{J}$	46.00	100.00	4.86	1.00	1.00	$8 \cdot 10^5$

Table 5.19: Obtained values for the thermal model parameters and remaining error contribution to the objective function f^θ.

Optimal set	α_exp 10^{-6}/K	κ_therm mW/mm K	c_0 mJ/mm^3 K	β	$\alpha_\mathrm{con}^\mathrm{air}$ W/m^2 K	$\alpha_\mathrm{con}^\mathrm{cl}$ W/m^2 K	f^θ
$\boldsymbol{k}^*_\mathrm{A}$	20.21	133.45	2.22	0.79	14.72	236.30	14.97
$\boldsymbol{k}^*_\mathrm{B}$	20.21	133.41	2.22	0.79	14.73	236.04	14.97
$\boldsymbol{k}^*_\mathrm{C}$	20.21	133.40	2.21	0.79	14.73	236.10	14.97
$\boldsymbol{k}^*_\mathrm{D}$	20.20	133.46	2.22	0.79	14.71	236.44	14.97
$\boldsymbol{k}^*_\mathrm{E}$	20.21	133.43	2.22	0.79	14.72	236.44	14.97
$\boldsymbol{k}^*_\mathrm{F}$	20.20	133.32	2.21	0.79	14.75	234.92	14.97
$\boldsymbol{k}^*_\mathrm{G}$	20.21	133.35	2.22	0.79	14.74	236.11	14.97
$\boldsymbol{k}^*_\mathrm{H}$	20.21	133.41	2.22	0.79	14.73	236.27	14.97
$\boldsymbol{k}^*_\mathrm{I}$	20.20	133.37	2.22	0.79	14.73	236.46	14.97
$\boldsymbol{k}^*_\mathrm{J}$	20.21	133.39	2.22	0.79	14.73	236.41	14.97

higher than the convection coefficient, underlining the assumption made in Section 5.5.2 that heat exchange through the clamping jaws dominates the heat exchange with the environment. The change in boundary coefficients clearly leads to a major difference between the two solutions which lies in the optimal value of the thermal conductivity κ_therm. Comparing the material response on the basis of the two parameter sets in Figure 5.32 shows that both solutions nevertheless fit the experimental temperature almost equally well. The most noticeable difference lies in the fit of the end temperature which does not return to the initial temperature (for a node at the centre of the specimen), but remains at a slightly higher value. This effect is based on the different temperatures of air and clamping jaws, combined with the plastic deformation of the specimen during mechanical loading. The difference in room- to clamping jaw temperature leads to a

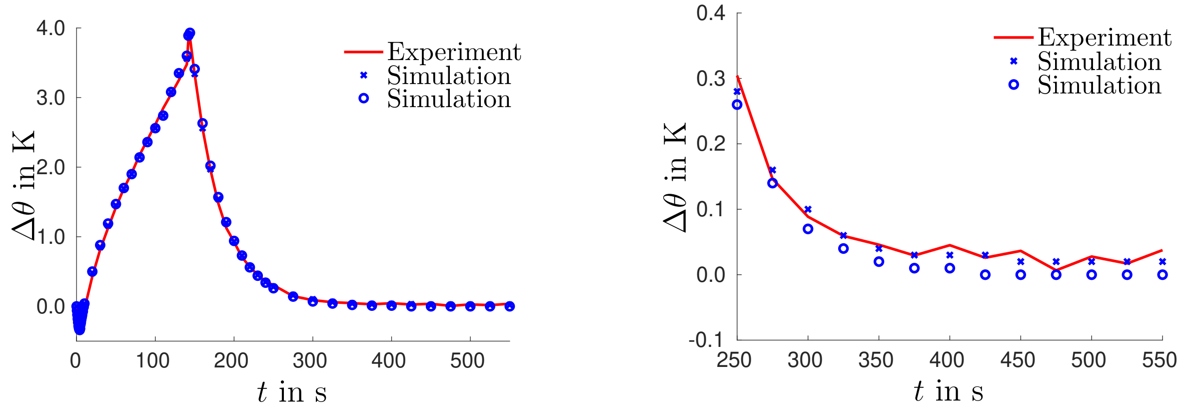

(a) Data over the whole time range.

(b) Data at the end of the cooling down phase.

Figure 5.32: Local temperature-time relation of experiment no. 3 and simulations using optimal parameter sets, evaluated at midpoint of the specimen. Identification with prescribed boundary coefficients (o) from Section 5.5.2 and identification including boundary coefficients (x).

higher steady state temperature at the centre point for an elongated specimen and can be reproduced by a simulation, only in case heat exchange with the surrounding air is considered. Thus, the temperature rise returns to zero for the parameter set with the prescribed boundary coefficients, since those boundary coefficients were chosen to represent isothermal conditions at the clamping jaws and adiabatic behaviour towards air. In contrast thereto, the optimised convection coefficient enables a reasonable amount of heat to be exchanged with the air leading to the aforementioned effect of a slightly higher remaining steady state temperature towards the centre of the specimen.

The model is therefore able to represent this behaviour by adapting the boundary coefficients but requires a significant change in the thermal conductivity, in order to maintain the overall good match. As discussed above, the effect of the remaining steady state temperature depends on the temperature difference between air and clamping device. Those values are prescribed in the simulation and rely on a measurement that is, like all measurements, subject to measurement errors. Thus, the question of sensitivities towards measured boundary temperatures arises, as is addressed in the following.

5.5.3.2 Sensitivity investigations

Thermal model parameters and boundary coefficients are identified again, but with modified boundary temperatures in the simulation. Prescribed values as well as resulting optimal model parameters are summarised in Tables 5.20 and 5.21. The precise temperature value of either air or clamping jaws does not matter as much as the actual difference, because results are almost identical as long as the prescribed temperature difference is also identical. Thus, the values from Table 5.20 are visualised in Figure 5.33, showing the relative change of optimal values with respect to the prescribed temperature difference between air and clamping jaws. Figures 5.33a and 5.33b show that

Table 5.20: Obtained values for the thermal model parameters and remaining error contribution to the objective function f^θ with modified air temperature. Prescribed values marked in grey.

$\Delta\theta$ K	θ^{air} K	θ^{cl} K	α_{exp} 10^{-6}/K	κ_{therm} mW/mm K	c_0 mJ/mm^3 K	β	$\alpha^{\mathrm{air}}_{\mathrm{con}}$ W/m^2 K	$\alpha^{\mathrm{cl}}_{\mathrm{con}}$ W/m^2 K	f^θ
0.00	296.70	296.70	20.01	154.32	2.19	0.79	11.99	183.16	16.87
0.10	296.80	296.70	20.11	144.84	2.20	0.79	13.35	182.76	16.52
0.30	297.00	296.70	20.19	136.80	2.21	0.79	14.41	197.83	15.88
0.50	297.20	296.70	20.23	133.11	2.22	0.79	14.85	217.62	15.35
0.60	297.30	296.70	20.21	133.43	2.22	0.79	14.75	227.67	15.14
0.70	297.40	296.70	20.21	133.45	2.22	0.79	14.72	236.30	14.97
0.80	297.50	296.70	20.20	133.63	2.21	0.79	14.66	244.89	14.84
0.90	297.60	296.70	20.15	137.06	2.21	0.78	14.13	250.65	14.74
1.10	297.80	296.70	20.03	146.58	2.20	0.78	12.63	264.28	14.65
1.30	298.00	296.70	19.88	159.85	2.19	0.78	10.54	278.13	14.65
1.80	298.50	296.70	19.66	183.17	2.17	0.77	6.99	300.49	14.71
2.30	299.00	296.70	19.55	194.77	2.16	0.77	5.08	311.27	14.76

Table 5.21: Obtained values for the thermal model parameters and remaining error contribution to the objective function f^θ with modified clamping temperature. Prescribed values marked in grey.

$\Delta\theta$ K	θ^{air} K	θ^{cl} K	α_{exp} 10^{-6}/K	κ_{therm} mW/mm K	c_0 mJ/mm^3 K	β	$\alpha^{\mathrm{air}}_{\mathrm{con}}$ W/m^2 K	$\alpha^{\mathrm{cl}}_{\mathrm{con}}$ W/m^2 K	f^θ
0.10	297.40	297.30	20.07	144.83	2.20	0.79	13.35	182.78	16.52
0.30	297.40	297.10	20.17	136.91	2.21	0.79	14.40	197.50	15.88
0.50	297.40	296.90	20.21	133.48	2.22	0.79	14.79	217.69	15.35
0.60	297.40	296.80	20.21	133.59	2.22	0.79	14.73	227.86	15.14
0.70	297.40	296.70	20.21	133.45	2.22	0.79	14.72	236.30	14.97
0.80	297.40	296.60	20.20	133.43	2.21	0.79	14.70	244.26	14.84
0.90	297.40	296.50	20.16	137.06	2.21	0.78	14.13	250.65	14.74
1.10	297.40	296.30	20.06	146.53	2.20	0.78	12.64	264.03	14.65

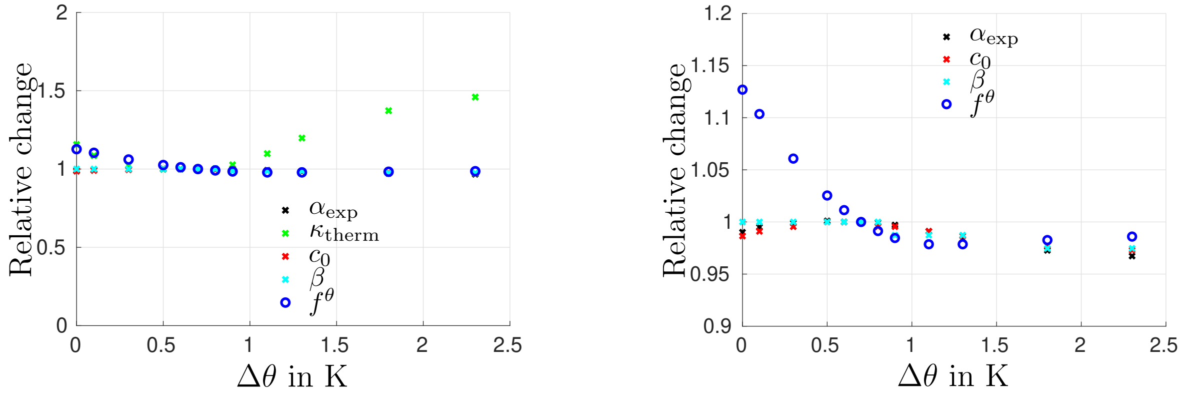

(a) Sensitivity of thermal model parameters and remaining squared error.

(b) Zoom to parameters with low sensitivity.

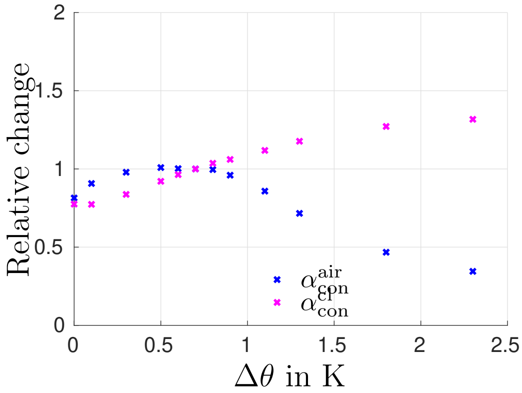

(c) Sensitivity of thermal boundary coefficients.

Figure 5.33: Relative change of model parameter with respect to prescribed temperature difference of air and clamping jaws ($\theta^{\mathrm{air}} - \theta^{\mathrm{cl}}$). Reference are the values corresponding to the measured temperature difference of 0.7 K.

reasonable measurement errors in the prescribed external temperature difference have very little effect on the optimal value for the thermal expansion coefficient α_{exp}, the heat capacity c_0 and the scaling parameter β, which only change up to 4% for the case at hand. In contrast thereto, the optimal values of the remaining model parameter κ_{therm} as well as the unknown boundary coefficients react very sensitively to a change of the prescribed temperature difference and may differ up to 60%. Furthermore, the overall trend indicates the intrinsic correlation of the three latter parameters, all of which define a different type of heat conductivity. A drastic change in one (conductivity) parameter necessitates the other two parameters to change accordingly, in order to maintain the overall temperature fit. It is worth mentioning that, although the correlation between the parameters κ_{therm}, $\alpha^{\mathrm{air}}_{\mathrm{con}}$ and $\alpha^{\mathrm{cl}}_{\mathrm{con}}$ may be high, it is not a perfect correlation in the sense of dependency (linear or non-linear), which would have led to multiple equally suitable solutions in Section 5.5.3.

Thus, an identification of thermal boundary coefficients for low temperature rises appears possible but requires a precise measurement of temperatures at the surfaces of the specimen. Alternatively, an experimental setup which guarantees an identical temperature of air and clamping jaws would circumvent the problem of this kind of sensitivity, since the identification is not as sensitive to the overall temperature level as it is to a difference in prescribed temperatures at the boundaries.

5.5.4 Identification with reduced set of unknowns

So far, it has been shown that the whole set of unknown model parameters is identifiable on the basis of an experiment with only a low rise in temperature and a cooling down phase. The experiment therefore holds enough information for a (locally) unique fit for the specific model at hand. The obtained result can furthermore be verified but a simple validation attempt, i.e. comparing the optimal parameters against literature values, shows that the obtained model parameters can not be used for the prediction of different boundary value problems such as a simple heat conductor. Whether or not the optimal parameter set will pass a validation highly depends on the constitutive model that is chosen, but it was also mentioned in Section 2.9.2 that adding further experimental data might increase the validity of the obtained parameters. More precisely speaking, there may be applications where the classic thermal model parameters can either be pre-identified by using specialised experiments or simply be taken from literature. For those cases, the identification process reduces to the optimisation of the scaling parameter β and of the thermal boundary coefficients. Table 5.22 shows the result of such an identification for the aluminium alloy at hand. It can be seen that the remaining error value increases by 17% when compared to the solution with prescribed boundary coefficients and increases by 58% when compared to the solution with the optimised boundary coefficients. However, the obtained values are still within reasonable bounds. Moreover, this immense (relative) increase in remaining error can be put into perspective if the actual material response of the three parameter sets (Tables 5.17, 5.19 and 5.22) is compared with the experimental data. Figure 5.34 reveals an almost insignificant absolute difference between the material response of the three parameter sets mentioned before. This is due to the specific material model chosen which allows the adjustment of the remaining thermal model parameter β to obtain a slightly less optimal, but nevertheless still respectable, fit to the experimental data. Depending on the overall model formulation, it is therefore possible to either optimise the thermal model parameters along with the thermal boundary coefficients or to prescribe some parameter values (which were identified by means of other boundary value problems, e.g. simple heat conductor) while still maintaining a satisfyingly precise fit.

Thus, adding additional experimental information still leads to a verifiable set of model parameters (for the specific model at hand), with the improvement that the set can now be used to describe at least a small choice of different boundary value problems, such as loading-unloading-cooling of a dogbone specimen and a simple heat conductor. A validation, however, would require further data which was not used for the optimisation process and it stands to reason that the rather simple model used within this thesis will have its limits.

Table 5.22: Obtained values for the model parameters and remaining error contribution to the objective function f^θ using available literature values. Prescribed values are marked in grey.

Material parameter	α_{exp} 10^{-6}/K	κ_{therm} mW/mm K	c_0 mJ/mm^3 K	β	$\alpha_{\text{con}}^{\text{air}}$ W/m^2 K	$\alpha_{\text{con}}^{\text{cl}}$ W/m^2 K	f^θ
Optimal value	23.00	200.00	2.43	0.93	2.18	976.00	23.59

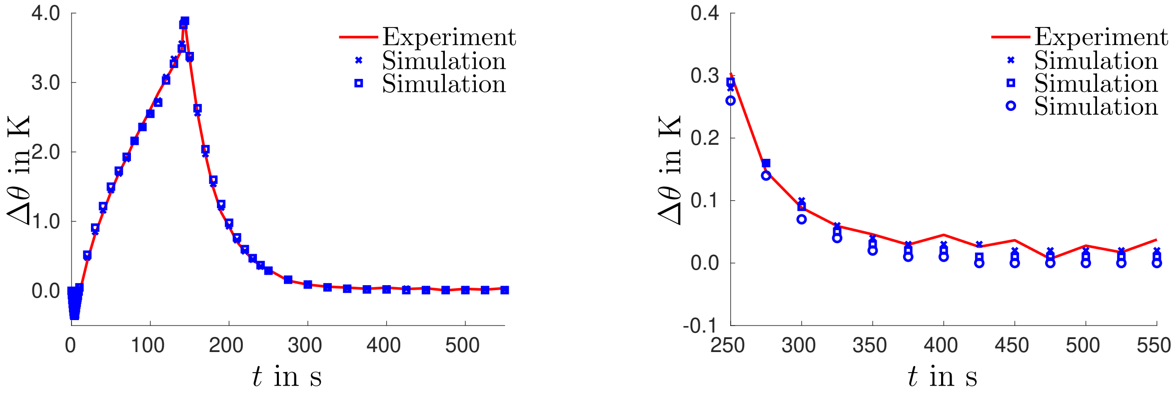

(a) Data over the whole time range. (b) Data at the end of the cooling-down phase.

Figure 5.34: Local temperature-time relation of experiment no. 3 and simulations using optimal parameter sets, evaluated at midpoint of the specimen. Identification with prescribed boundary coefficients (o) from Section 5.5.2, identification with whole set of optimised model parameters (x) from Section 5.5.3, and identification with prescribed thermal model parameters (□).

6 Concluding remarks

This thesis provides information on the treatment of inverse parameter identification problems regarding thermo-mechanically coupled constitutive models which are based on real full field measurements. A general framework and the necessary theoretical background is provided, so that a reader new to the field of parameter identification can apply the scheme or extend it as necessary. This includes not only the numerical implementation, but also the the performance of suitable experiments to avoid mistakes, intending to provide an overall easy access to the topic of identification for thermo-mechanically coupled constitutive models. Furthermore, the identifiability of thermal parameters on the basis of a simple tension test is analysed for two different models, supplying information on the required experimental data for a (locally) unique fit and on the sensitivity towards measured temperatures at the boundary.

A summary for each chapter and a discussion of results can be found below, explicitly answering the research questions posed in the introduction and in Sections 5.3 - 5.5. This is followed by a short outlook.

6.1 Summary

The first aspect - providing a theoretical background for the solution of the inverse problem of parameter identification - can be found in Chapter 2. A broad overview is given, ranging from the general definition of the inverse problem to the analysis of identifiability and validity of the results. Aspects new to the field of parameter identification are the algorithmic structure suited for the treatment of real experimental temperature data as well as the definition of relative displacements which intrinsically compensate rigid body motion of the specimen. Further details on the concept of optical displacement and temperature measurement may not be entirely new, but are important to know, especially if unfamiliar with the field of parameter identification. For example, the concept of identifiability is presented, explaining advantages and disadvantages of some measures for identifiability. Furthermore, the impact of different model formulations on the remaining error, the difference between model and material parameters, as well as the associated necessity for verification and validation is discussed, complementing the theoretical aspects of parameter identification.

The second aspect - analysing the applicability of the proposed framework in general and the identifiability of the parameters for the specific case at hand - is covered by Chapters 3 to 5. In Chapter 3, the experimental data of three simple tension tests is shown, including the general experimental setup and an analysis of the obtained data with respect to required features of a constitutive model. Based on that analysis, two constitutive models are presented in Chapter 4 which are derived from common standard model formulations using either associated or non-associated evolution equations. An additional term is added to the postulated free energy expression, introducing an additional model parameter which does not influence the mechanical material response but which allows a scaling of the predicted dissipation while maintaining a thermodynamically sound framework. The two models themselves feature an almost identical mechanical material response and only differ in the expression for the predicted dissipation. For each model, the dissipation follows directly from the postulated potentials and is a function of the current load state, requiring no further assumptions, e.g. regarding the relation towards cold work. Based on the constitutive equations, a first examination regarding the identifiability of model parameters is performed, determining which parameters can and which cannot be identified on the basis of a simple tension test. The actual identifiability analysis for the thermal parameters is performed in Chapter 5, combining the framework, the experimental data and the constitutive models from the previous chapters in a successive identification scheme. Identifiability of all thermal parameters is shown by means of a grid search approach. If identifications starting from several well distributed initial guesses all converge towards the same optimum, it is assumed that the solution is unique within a certain (trust) area. Based on this, it directly follows that the unknown parameters are independent and not connected via some linear or non-linear relation which would otherwise lead to a valley of solutions. The analysis is done in three parts, gradually extending the set of unknown thermal model parameters. At first, only the three classic thermal model parameters of a standard model κ_{therm}, $\alpha^{\text{air}}_{\text{con}}$ and $\alpha^{\text{cl}}_{\text{con}}$ are considered and the following questions are answered.

- **Does the proposed framework allow an identification in general?** The analysis of the obtained parameter sets show that the results are reasonable and fit the mechanical as well as thermal material response of the model to the provided experimental data. The framework, i.e. the pre-processing of temperature data and the successive identification approach, therefore appears to be sound and can be applied to different and more complex identifications. It is worth mentioning, however, that the successive split of the identification should only be used as long as the temperature can be assumed to have no significant influence on the mechanical part of the constitutive model.

- **Does the use of relative displacements compensate rigid body motion as is expected?** As shown in Section 5.3.1, the use of relative displacements leads to a set of elastic material parameters sufficiently close to literature values, whereas the use of unmodified displacements let the material appear significantly softer.

Relative displacement therefore present an adequate and easy to apply possibility to compensate rigid body motions.

- **Is a (locally) unique fit of the three classic thermal model parameters possible on the basis of simple tension test?** The results suggest that a locally unique fit of thermal parameters for the standard version of the model with associated evolution equations is possible on the basis of a simple tension test with monotonous loading since the grid search approach leads to only one optimal set. It is worth mentioning that identifiability has nothing to do with verifiability or even validity of the result as is commented on at the end of this section.

In a second step, the scaling parameter β is added to the set of unknown thermal model parameters. Furthermore, the identifications are performed by using the two extended models as well as two different experiments to analyse the impact of the model formulation on the identifiability and the required experimental data, answering the three questions below.

- **How do the different model formulations presented in Chapter 4 affect the optimal values of the model parameters?** Although the two models predict a similar mechanical material response, the predicted dissipation differs significantly. The thermal model parameters must therefore also be different for each model in order to match the given temperature distribution and temperature evolution, since the dissipated energy is the main source for the temperature rise during the experiment. This underlines the high model dependency of the inverse problem of parameter identification and that it is, in general, impossible to say a priori which model represents a certain material more accurately. If not already known, it therefore appears advisable to compare different model formulations and to at least find the limits of applicability by verification and validation attempts, before making a choice for predictive simulations.
- **Is a (locally) unique fit of the thermal model parameters possible, if β is included as an additional unknown?** For the two specific models at hand, a (locally) unique fit is possible, confirming that no model-intrinsic dependency connects the extended set of thermal model parameters. Thus, the enhancement of the standard model formulation makes sense from an identifiability point of view, allowing the use of models featuring a greater adaptability.
- **What kind of experimental data is required to ensure identifiability of all four thermal model parameters?** It was already mentioned that the result of an identification is highly model dependent, as is the answer to this question. An experiment with monotonous loading, a standard experiment in literature, holds sufficient information to ensure the identifiability of the thermal model parameters of the model with non-associated evolution equations (model 2), but leads to a

valley of solutions for the model with associated evolution equations (model 1). This is due to the model-intrinsic dissipation which is constant for model 1 (i.e. for the specific load case considered), and load state dependant for model 2. Hence, a scaling of dissipated power in model 1 is compensated by a likewise scaling of the remaining thermal parameters, all of which appear as a factor in one of the addends of the balance of energy. The scaling ratio of the dissipation of model 2, on the other hand, changes with each load step and can therefore only represent a certain temperature rise with one optimal parameter set. Consequently, enhancing the experimental data by using an experiment with an additional unloading and cooling phase allows a (locally) unique fit of both models. The results furthermore show that identifiability is not the same as verifiability or even validity of the result, since, for model 1, neither a valid nor a verifiable result could be obtained. For model 2, the experiment with monotonous loading already allows the identification of a unique and verifiable parameter set, but adding the additional experimental information leads to a set which also passes a first and simple validation attempt.

After having established the identifiability of the (potential) thermal material parameters, the identifiability of the (boundary value problem dependant) thermal boundary coefficients, required for Newton's law of cooling, is analysed by using the grid search approach and by answering the questions below.

- **Is a (locally) unique fit of thermal model parameters and boundary coefficients possible on the basis of full field temperature measurements?** The model with the non-associated evolution equation is used for this analysis due to its overall capability to represent the material for the boundary value problem at hand. Using an experiment with loading-unloading-cooling, the grid search approach yields only one set of optimal parameters, suggesting that the fit of thermal model parameters and boundary coefficients is (locally) unique.

- **How sensitive are the resulting parameter values with respect to the (measured) boundary temperatures required for Newton's law of cooling?** Comparing the obtained parameters with a reference solution based on reasonable, prescribed values for the boundary coefficients already indicates a high correlation between heat conduction and the two boundary coefficients, i.e. κ_{therm}, $\alpha^{\text{air}}_{\text{con}}$ and $\alpha^{\text{cl}}_{\text{con}}$, respectively. Not only does an analysis using several prescribed temperature differences for the surrounding air and clamping jaws underline the correlation of the three conduction-like model parameters, it furthermore shows the sensitivity of the optimal values with respect to small changes in the prescribed temperature difference of the surrounding media. To be more precise, a different prescribed external temperature difference naturally leads to different optimal values for the heat conduction and heat convection coefficient. These two parameters are very sensitive to the aforementioned changes and, moreover, cause an equally severe sensitivity in the thermal conduction coefficient due to the high correlation between the three parameters. Thus, the optimal value of the thermal conduction coefficient changes drastically with the prescribed temperature difference and is therefore extremely dependent on measurement errors. The obtained parameter sets can again be verified with respect to the data which was used for the identification in the first place, but the parameters fail a simple validation attempt. If, however, thermal material parameters are identified a priori by means of specialised experiments or taken from literature, the optimisation of the remaining model parameters yields different parameter values and the obtained fit to experimental temperature data may worsen (by almost 60% for the case at hand), but the actual absolute error may remain within reasonable limits (depending on the adaptability of the model).

Apart from the information on model dependency, identifiability and sensitivity of thermal model parameters, the results shown within this thesis provide further insight to the verification and validation of results. Especially the identification shown in Section 5.5.4, which uses additional data, answers the following question regarding the validation process in general.

- **How can a valid set of material parameters be identified?** Although it is not the aim of this work to provide material parameters which can be used for predictive simulations, a verification and (a simple) validation of the obtained parameter sets is always performed. Thus, it can be seen that the validity of the result does not only depend on the specific model, but also on the experimental data available. The general ability of the model to represent important material characteristics is of course vital and defines the limits of applicability in general. However, a model which is non perfect - in the sense that it would emulate the true material behaviour in all aspects (which is highly unlikely for a phenomenological model) - will actually only be able to predict the material response of a finite number of boundary value problems with limited precision. Such a model can nevertheless be suitable within a certain range of strain, strain rate and temperature, and the validity of the obtained parameter set can be increased with additional experimental data, even if the fit with less data already is (locally) unique. Due to the imperfection of the model, this will usually worsen the verification result as represented by the remaining objective function value, and a combination of model and experimental data must be found which passes both, verification and validation. How a suitable model must be defined entirely depends on the application at hand and what kind of experimental data leads to the best compromise between verification and validation cannot be said in general.

6.2 Outlook

So far, only experiments with a low rise in temperature have been used for the identification of thermal model parameters, but it is now possible to apply the underlying identification framework to materials which undergo a higher temperature rise during loading, e.g. in order to see whether this reduces the sensitivity towards external temperatures rendering the whole process closer to practical applications. However, this may involve more complex material behaviour, respectively models, such as viscous response and damage effects which contribute to dissipation and therefore to plastic heating. Modelling these effects will probably introduce further sources of discrepancy between actual and predicted dissipation, so that an identification, i.e. optimisation, for such a pairing of material and model is non-trivial and highly model dependent. Tests with steel have already shown a significantly higher rise in temperature if compared to aluminium, see Figure 6.1 and a first step could be the incorporation of damage into the thermo-mechanically coupled model to analyse the influence of damage associated dissipation contributions. Further research could concentrate on the fit of thermo-mechanically coupled models to boundary value problems with a more complex stress distribution, e.g. by using cruciform specimens, see Figure 6.2.

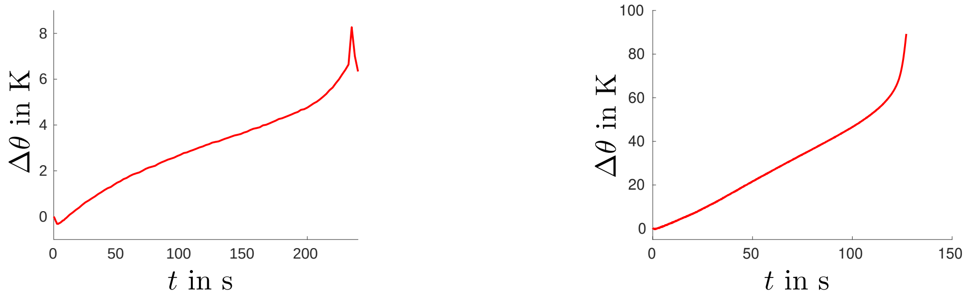

(a) Experiment with aluminium alloy AW6016. (b) Experiment with steel alloy EN1.4301.

Figure 6.1: Experimental temperature-time relation at the central node of a dogbone shaped specimen for monotonous loading until rupture of a simple tension test. Damage induced dissipation may contribute significantly even prior to macroscopic failure.

(a) Displacement field (top) and temperature field (bottom). (b) Biaxial testing machine for cruciform specimen.

Figure 6.2: Cruciform specimen can be used to analyse anisotropic material response.

A Influence of weights on correlation

The importance to consider the applied weights of the objective function within the correlation measure is discussed in this chapter.

Consider a homogeneous, simple tension test which provides axial and lateral strain information. The experiment is used to identify the parameters of a linear elastic material model $\boldsymbol{k} = [E,\, \nu]$, i.e. Young's modulus E and Poisson's ratio ν. The well known constitutive relations for uniaxial stress states read

$$\varepsilon_{11} = \frac{\sigma_{11}}{E} \tag{A.1}$$

$$\varepsilon_{22} = -\frac{\nu}{E}\,\sigma_{11} \tag{A.2}$$

and show that Young's modulus can be identified by means of axial and Poisson's ratio by means of lateral strain information. The identification is performed by using the objective function

$$\begin{aligned} f &= \sum_{t=1}^{n_{\mathrm{ts}}=2} \sum_{n=1}^{n_{\mathrm{d}}=2} W_n \left[r_n\right]_t^2 \\ &= W_1\ [\varepsilon_{11} - \varepsilon_{11}^{\exp}]_{t=1} + W_1\ [\varepsilon_{11} - \varepsilon_{11}^{\exp}]_{t=2} \\ &\quad + W_2\ [\varepsilon_{22} - \varepsilon_{22}^{\exp}]_{t=1} + W_2\ [\varepsilon_{22} - \varepsilon_{22}^{\exp}]_{t=2} \end{aligned} \tag{A.3}$$

which takes into account axial and lateral information of two time steps. Hence, if the response sensitivities (equal to the unweighted residual sensitivities $\mathbf{J}^{\mathrm{r}}$, see Section 2.6.4)

$$\frac{\mathrm{d}\varepsilon_{11}}{\mathrm{d}E} = -\,\frac{1}{E^2}\,\sigma_{11} \tag{A.4}$$

$$\frac{\mathrm{d}\varepsilon_{11}}{\mathrm{d}\nu} = 0 \tag{A.5}$$

$$\frac{\mathrm{d}\varepsilon_{22}}{\mathrm{d}E} = \frac{\nu}{E^2}\,\sigma_{11} \tag{A.6}$$

$$\frac{\mathrm{d}\varepsilon_{22}}{\mathrm{d}\nu} = -\,\sigma_{11} \tag{A.7}$$

$$\Rightarrow$$

$$\mathbf{J}_1^{\mathrm{r}} = \begin{bmatrix} -\frac{1}{E^2}\,\sigma_{11}\Big|_{t=1} \\ -\frac{1}{E^2}\,\sigma_{11}\Big|_{t=2} \\ \frac{\nu}{E^2}\,\sigma_{11}\Big|_{t=1} \\ \frac{\nu}{E^2}\,\sigma_{11}\Big|_{t=2} \end{bmatrix} \tag{A.8}$$

$$\mathbf{J}_2^{\mathrm{r}} = \begin{bmatrix} 0 \\ 0 \\ -\sigma_{11}\big|_{t=1} \\ -\sigma_{11}\big|_{t=2} \end{bmatrix} \tag{A.9}$$

are used for the computation of the correlation matrix

$$\overline{C^{\mathrm{S}}}_{ij} = \frac{\mathbf{J}_i^{\mathrm{r}} \cdot \mathbf{J}_j^{\mathrm{r}}}{\|\mathbf{J}_i^{\mathrm{r}}\|\,\|\mathbf{J}_j^{\mathrm{r}}\|} \qquad \Rightarrow \qquad \overline{\boldsymbol{C}^{\mathrm{S}}} = \begin{bmatrix} 1 & \bullet \\ \bullet & 1 \end{bmatrix} \qquad \text{with} \quad \|\bullet\| < 1 \tag{A.10}$$

it indicates the identifiability of both parameters, independent of the chosen weights. However, if the factor weighting the lateral strains is set to zero $W_2 = 0$, Poisson's ratio becomes unidentifiable which is only reflected in the correlation based on the weighted residual sensitivities

$$C_{ij}^{\mathrm{S}} = \frac{\mathbf{J}_i^{\mathrm{Wr}} \cdot \mathbf{J}_j^{\mathrm{Wr}}}{\|\mathbf{J}_i^{\mathrm{Wr}}\|\,\|\mathbf{J}_j^{\mathrm{Wr}}\|} \qquad \Rightarrow \qquad \boldsymbol{C}^{\mathrm{S}} = \begin{bmatrix} 1 & \text{n.d.} \\ \text{n.d.} & \text{n.d.} \end{bmatrix} \tag{A.11}$$

with

$$\mathbf{J}_1^{\mathrm{Wr}} = \begin{bmatrix} -\,W_1\,\frac{\sigma_{11}}{E^2}\Big|_{t=1} \\ -\,W_1\,\frac{\sigma_{11}}{E^2}\Big|_{t=2} \\ W_1\,\frac{\nu}{E^2}\,\sigma_{11}\Big|_{t=1} \\ W_1\,\frac{\nu}{E^2}\,\sigma_{11}\Big|_{t=2} \end{bmatrix} \quad , \quad \mathbf{J}_2^{\mathrm{Wr}} = \begin{bmatrix} 0 \\ 0 \\ 0 \\ 0 \end{bmatrix} \tag{A.12}$$

as defined in Section 2.6.4.

B Construction of the covariance matrix

This chapter contains additional information on the construction of the covariance matrix for the material parameters. It is a condensed summary of information found in [37], [13] and [67] applied to the problem of parameter identification at hand. Although it is the aim of this chapter to provide a basic understanding of the underlying assumptions which lead to the specific form of the covariance matrix shown in Equation (2.36), a basic knowledge in the field of statistics is required and the aforementioned publications are strongly recommanded, especially [13] Sections 3.3, 3.5-3.8 and 6.2.

Regarding the covariance matrix of the material parameters $\boldsymbol{P}^{\boldsymbol{k}}$, a direct construction

$$P_{ij}^{\boldsymbol{k}} = E\left(\left[k_i - E\left(k_i\right)\right]\left[k_j - E\left(k_j\right)\right]\right) \tag{B.1}$$

would require direct measurements of the parameters as well as an expected or mean value $E\left(k_i\right)$, which is intrinsically not possible/available. Instead, some material response $(\bullet)$ is measured which depends on and therefore provides indirect information about the material parameters. Hence, the linear transformation of variables as shown in [13] Section 3.8 can be applied to the weighted residual $\mathbf{r}^{\mathrm{W}}\left(\boldsymbol{k}\right)$ (containing n_{tot} entries) as a function of the random variable $\boldsymbol{k}$ (containing the n_{p} parameters). It is worth noting that it is important to use the weighted and not the unweighted residual or even simply the material response, since the weights can have a significant influence on the correlation of parameters, see [14] or Appendix A. Following the steps in [13], the weighted residual is linearised around the optimal parameter set $\boldsymbol{k}^*$ by

$$\mathrm{Lin}\left(\mathbf{r}^{\mathrm{W}}\right) = \mathbf{r}_{\mathrm{lin}}^{\mathrm{W}} = \mathbf{r}^{\mathrm{W}}\big|_{\boldsymbol{k}^*} + \underline{\underline{T}} \cdot \left[\boldsymbol{k} - \boldsymbol{k}^*\right] = \underline{\underline{T}} \cdot \boldsymbol{k} + \mathbf{a} \tag{B.2}$$

with the matrix of weighted residual sensitivities

$$\underline{\underline{T}} = \frac{\mathrm{d}\mathbf{r}^{\mathrm{W}}}{\mathrm{d}\boldsymbol{k}} = \begin{bmatrix} \mathbf{J}_1^{\mathrm{Wr}} & \mathbf{J}_2^{\mathrm{Wr}} & \dots & \mathbf{J}_{n_{\mathrm{p}}}^{\mathrm{Wr}} \end{bmatrix} \tag{B.3}$$

containing the vectors of weighted residual sensitivities as defined in Equation (2.33). Thus, the expected values of $\mathbf{r}_{\mathrm{lin}}^{\mathrm{W}}$ and $\boldsymbol{k}$ are related by

$$E\left(\mathbf{r}_{\mathrm{lin}}^{\mathrm{W}}\right) = \hat{\mathbf{r}}_{\mathrm{lin}}^{\mathrm{W}} = \underline{\underline{T}} \cdot \hat{\boldsymbol{k}} + \mathbf{a}\,. \tag{B.4}$$

This relation can now be used in the definition of the covariance matrix of the weighted residual

$$\begin{aligned} P^{\mathrm{Wr}}_{ij} &= E\left(\left[r^{\mathrm{W}}_i - E\left(r^{\mathrm{W}}_i\right)\right]\left[r^{\mathrm{W}}_j - E\left(r^{\mathrm{W}}_j\right)\right]\right) \\ &= E\left(\left[T_{im}\,k_m + a_i - T_{im}\,\hat{k}_m - a_i\right]\left[T_{jn}\,k_n + a_j - T_{jn}\,\hat{k}_n - a_j\right]\right) \\ &= E\left(\left[T_{im}\,k_m - T_{im}\,\hat{k}_m\right]\left[T_{jn}\,k_n - T_{jn}\,\hat{k}_n\right]\right) \\ &= T_{im} E\left(\left[k_m - \hat{k}_m\right]\left[k_n - \hat{k}_n\right]\right) T^{\mathrm{t}}_{nj} \\ &= T_{im}\,P^{\boldsymbol{k}}_{mn}\,T^{\mathrm{t}}_{nj} \end{aligned} \tag{B.5}$$

which, as can now be seen, is connected with the desired covariance matrix of the material parameters $\boldsymbol{P^k}$. Solving for the latter yields

$$P^{\boldsymbol{k}}_{ij} = T^{-1}_{im}\,P^{\mathrm{Wr}}_{mn}\,T^{-\mathrm{t}}_{nj}\,. \tag{B.6}$$

In order to end up with the definition of the covariance matrix as given in Equation (2.36), some further assumption must be made

- the mean of the residuals vanishes $E\left(r^{\mathrm{W}}_i\right) = \hat{r}^{\mathrm{W}}_i = 0$ (i.e. the model is sufficiently accurate)
- the residuals are uncorrelated, i.e. a change in one residual r^{W}_i has nothing to do with r^{W}_j, so that $P^{\mathrm{Wr}}_{ij} = 0 \ \ \forall\, i \neq j$
- the residuals share a common variance σ^2

see [37]. Especially the last two assumptions lead to the following, simplified structure of the covariance matrix of the weighted residuals

$$P^{\mathrm{Wr}}_{ij} = \sigma^2\,\delta_{ij} \tag{B.7}$$

with δ_{ij} being the entries of the $n_{\mathrm{tot}} \times n_{\mathrm{tot}}$ identity matrix. Thus, Equation (B.7) can be used in (B.6) to end up with the format of the covariance matrix for the material parameters as introduced in Equation (2.36), i.e.

$$\begin{aligned} P^{\boldsymbol{k}}_{ij} &= \sigma^2\,T^{-1}_{im}\,\delta_{mn}\,T^{-\mathrm{t}}_{nj} \\ &= \sigma^2\,T^{-1}_{im}\,T^{-\mathrm{t}}_{mj} \\ &= \sigma^2\,\left[{\boldsymbol{H}^{\mathrm{f}}_{\mathrm{lin}}}^{-1}\right]_{ij} \end{aligned} \tag{B.8}$$

with

$$\underline{\underline{T}}^{-1} \cdot \underline{\underline{T}}^{-\mathrm{t}} = \left[\underline{\underline{T}}^{\mathrm{t}} \cdot \underline{\underline{T}}\right]^{-1} = {\boldsymbol{H}^{\mathrm{f}}_{\mathrm{lin}}}^{-1}\,. \tag{B.9}$$

All that remains to be defined is the variance of the residuals σ^2. It was already assumed that all residuals share a common variance

$$\sigma^2 = \sigma^2\left(r_i^{\mathrm{W}}\right) = \sigma^2\left(r_j^{\mathrm{W}}\right) = \sigma^2\left(\bar{r}^{\mathrm{W}}\right) \tag{B.10}$$

which must therefore be identical to the variance of the average residual $\bar{r}^{\mathrm{W}}$. Following the reasoning in [13] Section 6.2, the variance of the average residual

$$\sigma^2\left(\bar{r}^{\mathrm{W}}\right) = \frac{1}{n_{\mathrm{tot}}} \sum_{i=1}^{n_{\mathrm{tot}}} \sigma^2\left(r_i^{\mathrm{W}}\right) \tag{B.11}$$

can be approximated by the empirical variance

$$\begin{aligned} s^2 &= \frac{1}{n_{\mathrm{dof}}} \sum_{i=1}^{n_{\mathrm{tot}}} \left[r_i^{\mathrm{W}} - \hat{r}_i^{\mathrm{W}}\right]^2 \\ &\approx \sigma^2 \end{aligned} \tag{B.12}$$

using the difference of the observed value to the expected value. At this point the first assumption reduces the empirical variance to the expression introduced in Equation (2.38)

$$\begin{aligned} s^2 &= \frac{1}{n_{\mathrm{dof}}} \sum_{i=1}^{n_{\mathrm{tot}}} \left[r_i^{\mathrm{W}}\right]^2 \\ &= \frac{\mathbf{r}^{\mathrm{W}} \cdot \mathbf{r}^{\mathrm{W}}}{n_{\mathrm{dof}}} \\ &\approx \sigma^2 \,. \end{aligned} \tag{B.13}$$

Finally, it should be mentioned that the definition of the (statistical) degrees of freedom n_{dof} is meant to guarantee certain properties of the empirical variance which is then called an unbiased approximation of the variance, see [13] Section 6.2. However, two different definitions can be found in literature

- $n_{\mathrm{dof}} = n_{\mathrm{tot}} - 1$, e.g. in [26] or [13] Section 6.2
- $n_{\mathrm{dof}} = n_{\mathrm{tot}} - n_{\mathrm{p}}$, with the number of parameters n_{p}, e.g. in [37] or [67] Section 5.7

Although different at first sight, both definitions asymptotically approach $n_{\mathrm{dof}} = n_{\mathrm{tot}}$ for large n_{tot}, i.e. a large amount of data.

C Examples for the identifiability based on Hessian

Possibilities and limits of the Hessian as a measure for identifiability are shown in this chapter by means of three exemplarily chosen model functions with two model parameters. At first a function with an isolated minimum is analysed showing that especially the approximated Hessian can also be singular at isolated minima. This is followed by two functions with either an intrinsic non-linear or linear parameter relation. Both functions suggest that the parameter dependencies can be identified a priori at arbitrary points by using the approximated Hessian. The chapter closes with a proof that the approximated Hessian must indeed be singular at arbitrary points in case a subset of model parameters is dependant.

No parameter relation Consider the model function

$$y = [2\,a]^3\; x + [b-1]^2\; x^2 \tag{C.1}$$

with the unknown but independent model parameters a and b. Assume that the three data points

$$\begin{aligned} (x_1,\, y_1) &= (1,\, 9)\\ (x_2,\, y_2) &= (2,\, 9)\\ (x_3,\, y_3) &= (3,\, 9) \end{aligned} \tag{C.2}$$

are available for the identification so that the objective function

$$f = \sum_{i=1}^{3} r_i^2 \tag{C.3}$$

can be defined by using the residuals

$$r_i = y\,(x_i) - y_i = \left[[2\,a]^3\; x_i + [b-1]^2\; x_i^2\right] - 9\,. \tag{C.4}$$

The Hessian of this function then reads

$$\begin{aligned} \boldsymbol{H}^{\mathrm{f}} &= \sum_{i=1}^{3} 2 \left[\bar{\boldsymbol{H}}^{\mathrm{f}}{}_{\mathrm{lin}}\right]_i + 2\, r_i\, \boldsymbol{H}^{\mathrm{r}}_i \\ &= \boldsymbol{H}^{\mathrm{f}}_{\mathrm{lin}} + \sum_{i=1}^{3} 2\, r_i\, \boldsymbol{H}^{\mathrm{r}}_i\,, \end{aligned} \tag{C.5}$$

with

$$\left[\bar{\boldsymbol{H}}^{\mathrm{f}}{}_{\mathrm{lin}}\right]_i = 8 \begin{bmatrix} 9\,[2\,a]^4\,x_i^2 & 3\,[2\,a]^2\,[b-1]\,x_i^3 \\ 3\,[2\,a]^2\,[b-1]\,x_i^3 & [b-1]^2\,x_i^4 \end{bmatrix} \tag{C.6}$$

and

$$\boldsymbol{H}^{\mathrm{r}}_i = \begin{bmatrix} 48\,a\,x_i & 0 \\ 0 & 2\,x_i^2 \end{bmatrix} \tag{C.7}$$

see Section 2.6.4. If restricted to $0 \leq a \leq 3$ and $0 \leq b \leq 3$, the function has one isolated minimum at ($a = 0.78$, $b = 1.00$), one isolated maximum at ($a = 0.00$, $b = 1.00$) and a saddle point at ($a = 0.00$, $b = 2.13$), see Figure C.1. However, the Hessian $\boldsymbol{H}^{\mathrm{f}}$ is clearly singular for $a = 0$ and the approximated Hessian $\boldsymbol{H}^{\mathrm{f}}_{\mathrm{lin}}$ is also singular for $b = 1$, see (C.5), (C.6) and (C.7). Hence, simply applying the identifiability test at the minimum by using the approximated Hessian (as is usually done) would falsely indicate a parameter dependency. This simple example underlines that the second derivative test is usually considered inconclusive if the Hessian is positive semi-definite and assigning a general interpretation to this case may generally be deceptive.

Non-linear parameter relation Consider the model function

$$y = [2\,a]^3\,x^2 + [b-1]^2\,x^2 = \left[[2\,a]^3 + [b-1]^2\right]\,x^2 = c\,x^2 \tag{C.8}$$

with the unknown and dependent model parameters a and b which are related by the function

$$c = [2\,a]^3 + [b-1]^2\,. \tag{C.9}$$

Again, the same three data points and the objective function

$$(x_1,\,y_1) = (1,\,9) \qquad (x_2,\,y_2) = (2,\,9) \qquad (x_3,\,y_3) = (3,\,9) \tag{C.10}$$

$$f = \sum_{i=1}^{3} r_i^2 \tag{C.11}$$

are available for the identification by using the residuals

$$r_i = y\,(x_i) - y_i = \left[\left[[2\,a]^3 + [b-1]^2\right]\,x_i^2\right] - 9\,. \tag{C.12}$$

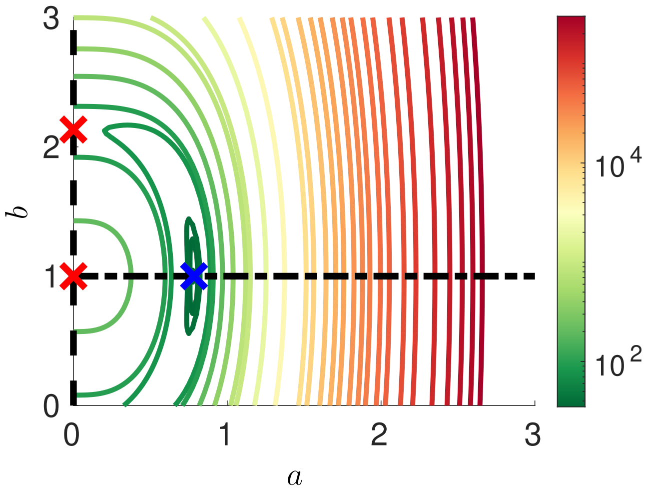

Figure C.1: Contour plot of the objective function (C.3). Minimum is marked by X, maximum and saddle point by X. The Hessian is singular along the line (– –), the approximated Hessian is furthermore singular along the line (-·-).

The Hessian of this function reads

$$\begin{aligned} \boldsymbol{H}^{\mathrm{f}} &= \sum_{i=1}^{3} 2\left[\bar{\boldsymbol{H}}^{\mathrm{f}}{}_{\mathrm{lin}}\right]_i + 2\,r_i\,\boldsymbol{H}^{\mathrm{r}}_i \\ &= \boldsymbol{H}^{\mathrm{f}}_{\mathrm{lin}} + \sum_{i=1}^{3} 2\,r_i\,\boldsymbol{H}^{\mathrm{r}}_i\,, \end{aligned} \tag{C.13}$$

with

$$\begin{aligned} \left[\bar{\boldsymbol{H}}^{\mathrm{f}}{}_{\mathrm{lin}}\right]_i &= 8\begin{bmatrix} 9\,[2\,a]^4\;x_i^4 & 3\,[2\,a]^2\;[b-1]\;x_i^4 \\ 3\,[2\,a]^2\;[b-1]\;x_i^4 & [b-1]^2\;x_i^4 \end{bmatrix} \\ &= 8\,x_i^4\begin{bmatrix} 9\,[2\,a]^4 & 3\,[2\,a]^2\;[b-1] \\ 3\,[2\,a]^2\;[b-1] & [b-1]^2 \end{bmatrix} \end{aligned} \tag{C.14}$$

and

$$\boldsymbol{H}^{\mathrm{r}}_i = \begin{bmatrix} 48\,a\,x_i & 0 \\ 0 & 2\,x_i^2 \end{bmatrix}. \tag{C.15}$$

If restricted to $0 \leq a \leq 3$ and $0 \leq b \leq 3$, the function has infinitely many solution points along the iso-line $c = 1.29$ and one isolated maximum at $(a = 0.00,\, b = 1.00)$, see Figure C.2. As expected, the Hessian $\boldsymbol{H}^{\mathrm{f}}$ is singular for all a and b which fulfil $c = [2\,a]^3 + [b-1]^2 = 1.29$. The approximated Hessian $\boldsymbol{H}^{\mathrm{f}}_{\mathrm{lin}}$, however, is singular for arbitrary combinations of a and b, see (C.13) and (C.14). The proof at the end of this chapter shows that this must always be the case for functions with intrinsic model

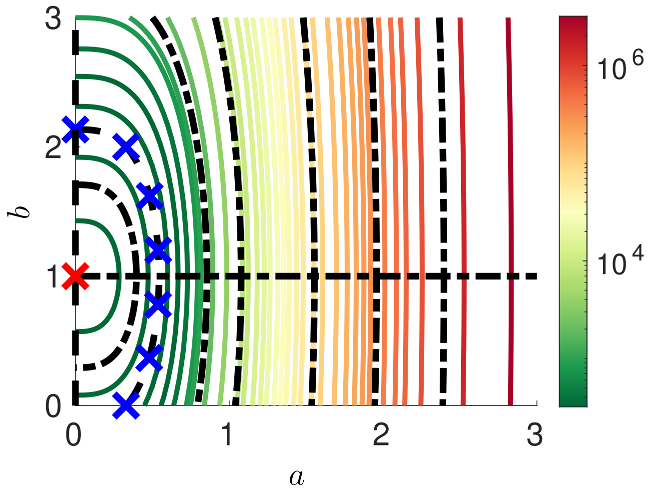

Figure C.2: Contour plot of the objective function (C.11). Minimum is marked by X, maximum by X. The Hessian is singular along the lines (−−), the approximated Hessian is furthermore singular on the whole domain as indicated by the lines (-·-).

dependencies and not just for the specific function at hand. Evaluating the Hessian at the point $a^* = 0.53$ and $b^* = 1.25$ which lies on the iso-line $c^* = 1.29$ yields the Hessian

$$\boldsymbol{H}^{\mathrm{f}} = 1000 \begin{bmatrix} 9.23 & 0.67 \\ 0.67 & 0.049 \end{bmatrix} \tag{C.16}$$

with the Eigenvalues and Eigenvectors

$$\lambda_1 = 0 \qquad \boldsymbol{\Phi}_1 = \begin{bmatrix} 1.00 \\ -13.73 \end{bmatrix}, \tag{C.17}$$

$$\lambda_2 = 9279.57 \qquad \boldsymbol{\Phi}_2 = \begin{bmatrix} 13.73 \\ 1.00 \end{bmatrix}. \tag{C.18}$$

Computing the linearised relation between the two parameters at that point

$$b = \sqrt{c^* - [2\,a]^2} + 1 \tag{C.19}$$

$$\begin{aligned} \Rightarrow \quad \mathrm{Lin}\,(b) &= b^* + \frac{\mathrm{d}b}{\mathrm{d}a}\,[a - a^*] \\ &= b^* - 13.73\,[a - a^*] \end{aligned} \tag{C.20}$$

$$\Rightarrow \quad [b - b^*] = -\,13.73\,[a - a^*] \tag{C.21}$$

shows that the Eigenvector associated with the zero Eigenvalue reveals the linearised relation between the two parameters.

Linear parameter relation Consider the model function

$$y = [2\,a + [b-1]]^2\; x^2 = c^2\, x^2 \tag{C.22}$$

with the unknown and linearly dependent model parameters a and b which are related by the function

$$c = 2\,a + [b - 1] \; . \tag{C.23}$$

The three data points and the objective function

$$(x_1,\, y_1) = (1,\, 9) \qquad (x_2,\, y_2) = (2,\, 9) \qquad (x_3,\, y_3) = (3,\, 9) \tag{C.24}$$

$$f = \sum_{i=1}^{3} r_i^2 \tag{C.25}$$

are used for the identification together with the residuals

$$r_i = y\,(x_i) - y_i = \left[[2\,a + [b-1]]^2\; x^2\right] - 9\,. \tag{C.26}$$

The Hessian of this function reads

$$\begin{aligned} \boldsymbol{H}^{\mathrm{f}} &= \sum_{i=1}^{3} 2\,\left[\bar{\boldsymbol{H}}^{\mathrm{f}}{}_{\mathrm{lin}}\right]_i + 2\,r_i\,\boldsymbol{H}_i^{\mathrm{r}} \\ &= \boldsymbol{H}_{\mathrm{lin}}^{\mathrm{f}} + \sum_{i=1}^{3} 2\,r_i\,\boldsymbol{H}_i^{\mathrm{r}}\,, \end{aligned} \tag{C.27}$$

with

$$\left[\bar{\boldsymbol{H}}^{\mathrm{f}}{}_{\mathrm{lin}}\right]_i = 8\;[2\,a + [b-1]]^2\; x_i^4 \begin{bmatrix} 4 & 2 \\ 2 & 1 \end{bmatrix} \tag{C.28}$$

and

$$\boldsymbol{H}_i^{\mathrm{r}} = 2\,x_i^2 \begin{bmatrix} 4 & 2 \\ 2 & 1 \end{bmatrix} \; . \tag{C.29}$$

If restricted to $0 \le a \le 3$ and $0 \le b \le 3$, the function has infinitely many solution points along the iso-line $c = 1.13$ and infinitely many maxima along the iso-line $c = 0$, see Figure C.3. For this case of linear parameter dependency, however, the Hessian $\boldsymbol{H}^{\mathrm{f}}$ is singular for all a and b, see (C.27), (C.28) and (C.29). Evaluating the Eigenvalues and Eigenvectors of the Hessian at the point $a^* = 0.44$ and $b^* = 1.25$ which lies on the iso-line $c^* = 1.29$ yields

$$\lambda_1 = 0 \qquad \boldsymbol{\Phi}_1 = \begin{bmatrix} 1.00 \\ -2.00 \end{bmatrix}\,, \tag{C.30}$$

$$\lambda_2 = 5040.00 \qquad \boldsymbol{\Phi}_2 = \begin{bmatrix} 2.00 \\ 1.00 \end{bmatrix}\; . \tag{C.31}$$

Again, Eigenvector $\boldsymbol{\Phi}_1$ reveals the (linearised) relation of the two dependant parameters at the chosen point in parameter space.

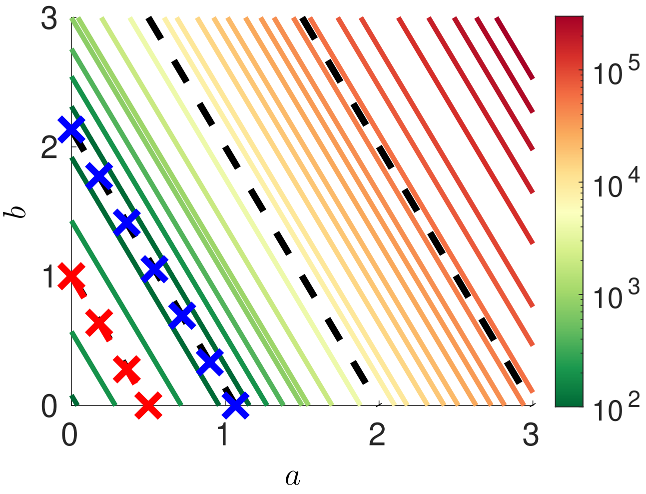

Figure C.3: Contour plot of the objective function (C.25). Minima are marked by X, maximum by X. The Hessian is singular on the whole domain as indicated by the lines (−−).

Singularity of the approximated Hessian The last two examples have revealed that especially the approximated Hessian appears to be singular at arbitrary points in parameter space for model functions with an intrinsic parameter dependency. In order to prove that this is the case in general, the model function

$$y = \hat{y}\left(\tilde{\boldsymbol{k}}, c\left(\bar{\boldsymbol{k}}\right)\right) \tag{C.32}$$

is considered with the vector of all n_k model parameters

$$\boldsymbol{k} = \begin{bmatrix} \tilde{\boldsymbol{k}} \\ \bar{\boldsymbol{k}} \end{bmatrix} \tag{C.33}$$

being split into $n_{\tilde{k}}$ independent model parameters $\tilde{\boldsymbol{k}}$ and $n_{\bar{k}}$ parameters $\bar{\boldsymbol{k}}$ which are related by means of some function c. Remembering that the approximated Hessian is defined as

$$\boldsymbol{H}^{\mathrm{f}}_{\mathrm{lin}} = 2 \sum_{n=1}^{n_{\mathrm{tot}}} W_n \left[\boldsymbol{J}^{\mathrm{r}}_n \otimes \boldsymbol{J}^{\mathrm{r}}_n\right] . \tag{C.34}$$

the derivative of the residual function

$$\boldsymbol{J}^{\mathrm{r}}_n = \left.\frac{\mathrm{d}y}{\mathrm{d}\boldsymbol{k}}\right|_n = \begin{bmatrix} \frac{\mathrm{d}y}{\mathrm{d}\tilde{\boldsymbol{k}}} \\ \frac{\mathrm{d}y}{\mathrm{d}c}\frac{\mathrm{d}c}{\mathrm{d}\bar{\boldsymbol{k}}} \end{bmatrix}_n \tag{C.35}$$

must be evaluated at all n_{tot} observed states and points. It is important to note that the model function y and its derivatives $\frac{\mathrm{d}y}{\mathrm{d}\tilde{\boldsymbol{k}}}$ and $\frac{\mathrm{d}y}{\mathrm{d}c}$ may in general depend on the state n, whereas the function c and its derivatives $\frac{\mathrm{d}c}{\mathrm{d}\bar{\boldsymbol{k}}}$ intrinsically do not depend on the current state. The approximated Hessian can now be written as

$$\boldsymbol{H}^{\mathrm{f}}_{\mathrm{lin}} = 2\sum_{n=1}^{n_{\mathrm{tot}}} W_n \begin{bmatrix} \frac{\mathrm{d}y}{\mathrm{d}\tilde{\boldsymbol{k}}} \otimes \frac{\mathrm{d}y}{\mathrm{d}\tilde{\boldsymbol{k}}} & \frac{\mathrm{d}y}{\mathrm{d}c}\frac{\mathrm{d}y}{\mathrm{d}\tilde{\boldsymbol{k}}} \otimes \frac{\mathrm{d}c}{\mathrm{d}\bar{\boldsymbol{k}}} \\ \frac{\mathrm{d}y}{\mathrm{d}c}\frac{\mathrm{d}c}{\mathrm{d}\bar{\boldsymbol{k}}} \otimes \frac{\mathrm{d}y}{\mathrm{d}\tilde{\boldsymbol{k}}} & \left[\frac{\mathrm{d}y}{\mathrm{d}c}\right]^2 \frac{\mathrm{d}c}{\mathrm{d}\bar{\boldsymbol{k}}} \otimes \frac{\mathrm{d}c}{\mathrm{d}\bar{\boldsymbol{k}}} \end{bmatrix}. \tag{C.36}$$

Comparing the i-th and j-th row of the lower $n_{\bar{k}} \times n_k$ matrix

$$\begin{aligned} \text{i-th row:} \quad & 2\sum_{n=1}^{n_{\mathrm{tot}}} W_n \begin{bmatrix} \frac{\mathrm{d}y}{\mathrm{d}c}\frac{\mathrm{d}c}{\mathrm{d}\bar{\boldsymbol{k}}_i}\frac{\mathrm{d}y}{\mathrm{d}\tilde{\boldsymbol{k}}} & \left[\frac{\mathrm{d}y}{\mathrm{d}c}\right]^2 \frac{\mathrm{d}c}{\mathrm{d}\bar{\boldsymbol{k}}_i}\frac{\mathrm{d}c}{\mathrm{d}\bar{\boldsymbol{k}}} \end{bmatrix} = 2\,\frac{\mathrm{d}c}{\mathrm{d}\bar{\boldsymbol{k}}_i}\sum_{n=1}^{n_{\mathrm{tot}}} W_n \begin{bmatrix} \frac{\mathrm{d}y}{\mathrm{d}c}\frac{\mathrm{d}y}{\mathrm{d}\tilde{\boldsymbol{k}}} & \left[\frac{\mathrm{d}y}{\mathrm{d}c}\right]^2 \frac{\mathrm{d}c}{\mathrm{d}\bar{\boldsymbol{k}}} \end{bmatrix} \\ \text{j-th row:} \quad & 2\sum_{n=1}^{n_{\mathrm{tot}}} W_n \begin{bmatrix} \frac{\mathrm{d}y}{\mathrm{d}c}\frac{\mathrm{d}c}{\mathrm{d}\bar{\boldsymbol{k}}_j}\frac{\mathrm{d}y}{\mathrm{d}\tilde{\boldsymbol{k}}} & \left[\frac{\mathrm{d}y}{\mathrm{d}c}\right]^2 \frac{\mathrm{d}c}{\mathrm{d}\bar{\boldsymbol{k}}_j}\frac{\mathrm{d}c}{\mathrm{d}\bar{\boldsymbol{k}}} \end{bmatrix} = 2\,\frac{\mathrm{d}c}{\mathrm{d}\bar{\boldsymbol{k}}_j}\sum_{n=1}^{n_{\mathrm{tot}}} W_n \begin{bmatrix} \frac{\mathrm{d}y}{\mathrm{d}c}\frac{\mathrm{d}y}{\mathrm{d}\tilde{\boldsymbol{k}}} & \left[\frac{\mathrm{d}y}{\mathrm{d}c}\right]^2 \frac{\mathrm{d}c}{\mathrm{d}\bar{\boldsymbol{k}}} \end{bmatrix} \end{aligned} \tag{C.37}$$

shows that all rows of the $n_{\bar{k}} \times n_k$ submatrix are identical up to a constant factor rendering the whole approximated Hessian singular for all model parameters and independent of the actual experimental, model function or type of dependency.

D Representation of Hill-type flow surface

The Hill-type tensor used in Section 4.1 can be introduced as

$$\mathsf{G} = \phi_{ij}\, \boldsymbol{A}_i \otimes \boldsymbol{A}_j + \varphi_i\, \mathsf{A}_i \tag{D.1}$$

whereby unit-vectors $\boldsymbol{a}_i$ define the structure tensors

$$\boldsymbol{A}_i = \boldsymbol{a}_i \otimes \boldsymbol{a}_i\,, \tag{D.2}$$

$$\mathsf{A}_i = \frac{1}{4}\left[\boldsymbol{A}_i \,\overline{\otimes}\, \boldsymbol{I} + \boldsymbol{A}_i \,\underline{\otimes}\, \boldsymbol{I} + \boldsymbol{I} \,\overline{\otimes}\, \boldsymbol{A}_i + \boldsymbol{I} \,\underline{\otimes}\, \boldsymbol{A}_i\right]\,, \tag{D.3}$$

with I denoting the second order identity tensor and the non-standard dyadic products defined as

$$[\boldsymbol{T}_1 \overline{\otimes} \boldsymbol{T}_2] : \boldsymbol{T}_3 = \boldsymbol{T}_1 \cdot \boldsymbol{T}_3 \cdot \boldsymbol{T}_2^{\mathrm{t}}\,, \text{ respectively} \tag{D.4}$$

$$[\boldsymbol{T}_1 \underline{\otimes} \boldsymbol{T}_2] : \boldsymbol{T}_3 = \boldsymbol{T}_1 \cdot \boldsymbol{T}_3^{\mathrm{t}} \cdot \boldsymbol{T}_2^{\mathrm{t}} \tag{D.5}$$

for second order tensors $\boldsymbol{T}_{1,2,3}$. For the purpose of illustration, the axes of symmetry in the intermediate configuration are assumed to be aligned with the Cartesian axes $\boldsymbol{a}_i = \bar{\boldsymbol{e}}_i$. Constants ϕ_{ij} and φ_i can be expressed by the classic Hill parameters, to be specific

$$\begin{aligned}
\phi_{11} &= F + G - [L - M + N]\,, & \phi_{12} &= \phi_{21} = -F\,, & \varphi_1 &= L - M + N\,,\\
\phi_{22} &= F + H - [L + M - N]\,, & \phi_{13} &= \phi_{31} = -G\,, & \varphi_2 &= L + M - N\,,\\
\phi_{33} &= G + H - [-L + M + N]\,, & \phi_{23} &= \phi_{32} = -H\,, & \varphi_3 &= -L + M + N\,.
\end{aligned} \tag{D.6}$$

The coefficients of G with respect to the aforementioned Cartesian axes can be provided in matrix form as

$$\begin{bmatrix}
\mathsf{G}_{1111} & \mathsf{G}_{1122} & \mathsf{G}_{1133} & \mathsf{G}_{1112} & \mathsf{G}_{1113} & \mathsf{G}_{1123}\\
\mathsf{G}_{2211} & \mathsf{G}_{2222} & \mathsf{G}_{2233} & \mathsf{G}_{2212} & \mathsf{G}_{2213} & \mathsf{G}_{2223}\\
\mathsf{G}_{3311} & \mathsf{G}_{3322} & \mathsf{G}_{3333} & \mathsf{G}_{3312} & \mathsf{G}_{3313} & \mathsf{G}_{3323}\\
\mathsf{G}_{1211} & \mathsf{G}_{1222} & \mathsf{G}_{1233} & \mathsf{G}_{1212} & \mathsf{G}_{1213} & \mathsf{G}_{1223}\\
\mathsf{G}_{1311} & \mathsf{G}_{1322} & \mathsf{G}_{1333} & \mathsf{G}_{1312} & \mathsf{G}_{1313} & \mathsf{G}_{1323}\\
\mathsf{G}_{2311} & \mathsf{G}_{2322} & \mathsf{G}_{2333} & \mathsf{G}_{2312} & \mathsf{G}_{2313} & \mathsf{G}_{2323}
\end{bmatrix}
=
\begin{bmatrix}
F+G & -F & -G & 0 & 0 & 0\\
-F & F+H & -H & 0 & 0 & 0\\
-G & -H & G+H & 0 & 0 & 0\\
0 & 0 & 0 & \frac{1}{2}L & 0 & 0\\
0 & 0 & 0 & 0 & \frac{1}{2}N & 0\\
0 & 0 & 0 & 0 & 0 & \frac{1}{2}M
\end{bmatrix} \tag{D.7}$$

since tensor G has minor and major symmetries.

E Limits for scaling parameter β in model 2

Boundaries for material parameter β are derived in this chapter to ensure that the dissipation of model 2, with non-associated evolution equations, is always larger or equal to zero.

The dissipation of model 2 is given in Equation (4.22) so that the associated dissipation inequality can be written as

$$\mathcal{D}^{\text{mech}} = \lambda_{\text{pm}} \left[b\,h\,\alpha^2 + [1-\beta]\,b\,M_{y_0}\alpha + \beta\,M_{y_0} \right] \geq 0\,. \tag{E.1}$$

For this model, the plastic multiplier will always be non-negative and it will be assumed that the same holds for the mechanical material parameters. Thus, inequality (E.1) is always fulfilled as long as

$$D\,(\alpha) = b\,h\,\alpha^2 + [1-\beta]\,b\,M_{y_0}\alpha + \beta\,M_{y_0} \geq 0\,,\ \text{with}\ \lambda_{\text{pm}} \geq 0\,. \tag{E.2}$$

Recalling that $b \geq 0$, $h \geq 0$ and $M_{y_0} \geq 0$, this function can be identified to be a convex, quadratic function in α with a y-intercept of $D\,(\alpha = 0) = \beta\,M_{y_0}$. It is now sufficient to ensure that

$$D \geq 0 \quad \forall\ \alpha \geq 0 \tag{E.3}$$

since α evolves positive for the model at hand. A first, lower boundary for the parameter β can easily be obtained by considering the y-intercept of the continuous function D. $D\,(\alpha = 0) \geq 0$ has to be fulfilled in order to ensure that the particular point of $\alpha = 0$ complies with (E.3). Hence

$$\beta \geq 0 \tag{E.4}$$

must hold to ensure a positive y-intercept. Further conditions for β can be derived by considering that the dissipation of the model will always be larger or equal to zero if the function

$$\begin{aligned} D\,(\alpha) = b\,h\,\alpha^2 + [1-\beta]\,b\,M_{y_0}\alpha + \beta\,M_{y_0} \ &\geq 0\,, \quad \text{with} \\ \beta\,,\ b\,,\ h\,,\ M_{y_0} \ &\geq 0 \end{aligned} \tag{E.5}$$

lies only in the first quadrant for $\alpha > 0$. There are only two possibilities for a convex, quadratic function with a positive y-intercept fulfilling this condition. Either both roots of the function must be negative, see Figure E.1a, or there are less than two roots, see Figure E.1b. In summation, the dissipation of the model is guaranteed to be larger or equal to zero if β is chosen such that either condition is met.

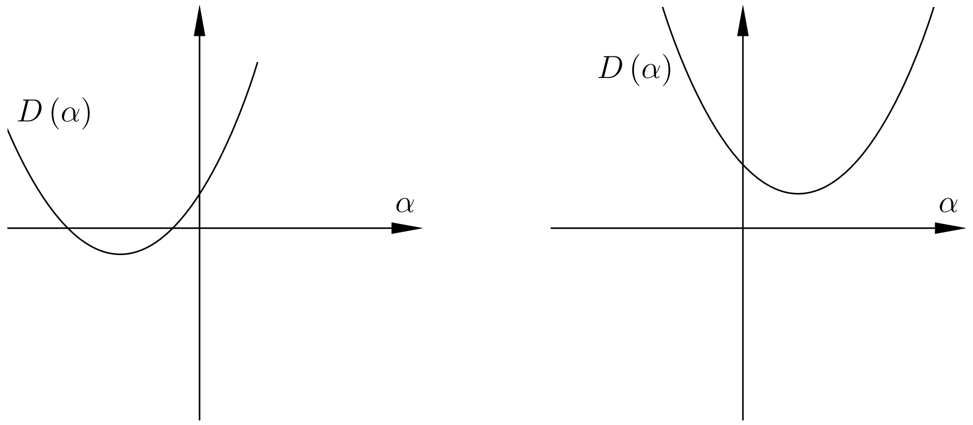

(a) Case 1 - D has only negative roots. (b) Case 2 - D has less than two roots.

Figure E.1: D is a convex, quadratic function in α and required to be in the first quadrant for all $\alpha > 0$ to ensure a dissipation which is larger or equal to zero.

Case 1 – negative roots The two roots $\alpha_{1,2}$ of function D can be computed by

$$\alpha_{1,2} = -\frac{[1-\beta]\,M_{y0}}{2\,h} \pm \sqrt{\frac{[1-\beta]^2\,M_{y0}^2}{4\,h^2} - \beta\,\frac{M_{y0}}{h\,b}}\,. \tag{E.6}$$

It has already been established that $\beta \geq 0$ so that only two different cases must be considered.

1. $\beta \leq 1$ – The first addend is negative for this case. Hence, it suffices to enforce the larger of the two roots

   $$\alpha_1 = -\frac{[1-\beta]\,M_{y0}}{2\,h} + \sqrt{\frac{[1-\beta]^2\,M_{y0}^2}{4\,h^2} - \beta\,\frac{M_{y0}}{h\,b}} \tag{E.7}$$

   to be negative, resulting in the inequality

   $$\begin{aligned} && \alpha_1 = -\frac{[1-\beta]\,M_{y0}}{2\,h} + \sqrt{\frac{[1-\beta]^2\,M_{y0}^2}{4\,h^2} - \beta\,\frac{M_{y0}}{h\,b}} &\leq 0 \\ \Leftrightarrow && \frac{[1-\beta]\,M_{y0}}{2\,h} &\geq \sqrt{\frac{[1-\beta]^2\,M_{y0}^2}{4\,h^2} - \beta\,\frac{M_{y0}}{h\,b}} \\ \Leftrightarrow && \left|\frac{[1-\beta]\,M_{y0}}{2\,h}\right| &\geq \sqrt{\frac{[1-\beta]^2\,M_{y0}^2}{4\,h^2} - \beta\,\frac{M_{y0}}{h\,b}} \qquad \text{with } 0 \leq \beta \leq 1 \\ \Leftrightarrow && \frac{[1-\beta]^2\,M_{y0}^2}{4\,h^2} &\geq \frac{[1-\beta]^2\,M_{y0}^2}{4\,h^2} - \beta\,\frac{M_{y0}}{h\,b} \\ \Leftrightarrow && \beta &\geq 0\,. \end{aligned} \tag{E.8}$$

   This renders one set of bounds for the material parameter β to be $0 \leq \beta \leq 1$.

2. $\beta > 1$ – The first addend is positive for this case and it must again be ensured that the larger of the two roots α_1 is negative. This however will not occur since

$$\alpha_1 = -\frac{[1-\beta]\, M_{y0}}{2\,h} + \sqrt{\frac{[1-\beta]^2\, M_{y0}^2}{4\,h^2} - \beta\,\frac{M_{y0}}{h\,b}} \tag{E.9}$$

is the sum of two positive addends. It is therefore impossible to have only negative roots if $\beta > 1$ and the resulting bounds are again $0 \leq \beta \leq 1$.

The roots of function D are therefore negative if $0 \leq \beta \leq 1$, leading to a dissipation of the model which is larger or equal to zero.

Case 2 – less than two roots The quadratic function D has less than two roots (in $\mathbb{R}$) in the case that the radicand of Equation (E.6)

$$r = \frac{[1-\beta]^2\, M_{y0}^2}{4\,h^2} - \beta\,\frac{M_{y0}}{h\,b} \tag{E.10}$$

is zero (only one root) or negative (no roots). This is the case if β lies between the two roots of r

$$\beta_{\mathrm{u,l}} = \frac{M_{y0}\, b + 2h\left[1 \pm \sqrt{\frac{M_{y0}\, b}{h} + 1}\right]}{M_{y0}\, b} \tag{E.11}$$

since r is a convex, quadratic function in β. Following therefrom, the convex function D has less than two roots in $\mathbb{R}$ so that the dissipation is always larger or equal to zero for

$$\beta_{\mathrm{l}} \leq \beta \leq \beta_{\mathrm{u}}\,. \tag{E.12}$$

Hence, the total set of bounds for the material parameter β which ensures a fulfilment of the second law of thermodynamics reads

$$0 \leq \beta \leq 1 \quad \vee \quad \beta_{\mathrm{l}} \leq \beta \leq \beta_{\mathrm{u}}\,, \text{ with } \beta_{\mathrm{u,l}} = \frac{M_{y0}\, b + 2h\left[1 \pm \sqrt{\frac{M_{y0}\, b}{h} + 1}\right]}{M_{y0}\, b}\,. \tag{E.13}$$

F Comparison of model responses

It was stated in Remark 4.4 that the two model formulations used within this thesis yield the same mechanical stress-strain response but dissipate a different amount of energy. This chapter contains the associated proof, assuming small strains, a neglectable influence of the low rise in temperature and dismissing the linear hardening part of model 1. Part of the derivation can also be found in [6].

At first, an expression for the dissipated energy is derived for the two small-strain-model formulations. Afterwards, the mechanical response of the two formulations is analysed for a specific load case. The desired expressions are derived parallelly for both models to allow a better comparison.

From the energy contributions

$$\text{Model - 1}\qquad \psi^{\mathrm{el}} = \frac{1}{2}\boldsymbol{\varepsilon}^{\mathrm{el}} : \mathbf{\mathsf{E}} : \boldsymbol{\varepsilon}^{\mathrm{el}}\,, \qquad \psi^{\mathrm{pl}} = [\sigma_{y_\infty} - \sigma_{y_0}]\left[\alpha + \frac{1}{H_{\exp}}\exp(-H_{\exp}\,\alpha)\right]\,, \tag{F.1}$$

$$\text{Model - 2}\qquad \psi^{\mathrm{pl}} = \frac{1}{2}\boldsymbol{\varepsilon}^{\mathrm{el}} : \mathbf{\mathsf{E}} : \boldsymbol{\varepsilon}^{\mathrm{el}}\,, \qquad \psi^{\mathrm{pl}} = \frac{1}{2}H\,\alpha^2\,, \tag{F.2}$$

the driving force K of the internal hardening variable α is derived, i.e.

$$\text{Model - 1}\qquad K = -\frac{\partial\psi}{\partial\alpha} = [\sigma_{y_0} - \sigma_{y_\infty}]\,[1 - \exp(-H_{\exp}\,\alpha)]\,, \tag{F.3}$$

$$\text{Model - 2}\qquad K = -\frac{\partial\psi}{\partial\alpha} = -H\,\alpha\,. \tag{F.4}$$

A yield surface

$$\text{Model - 1}\qquad \Phi = \|\boldsymbol{\sigma}^{\mathrm{dev}}\| - [\sigma_{y_0} - K] = \sigma^{\mathrm{eq}} - [\sigma_{y_0} - K]\,, \tag{F.5}$$

$$\text{Model - 2}\qquad \Phi = \|\boldsymbol{\sigma}^{\mathrm{dev}}\| - [\sigma_{y_0} - K] = \sigma^{\mathrm{eq}} - [\sigma_{y_0} - K] \tag{F.6}$$

is defined by using the norm of the deviatoric part of the stress tensor as an equivalent stress measure which is positively homogeneous of degree one. The evolution equations are derived from a plastic potential and are assumed to be associated to the yield surface for model 1 and non-associated for model 2, i.e.

$$\text{Model - 1}\qquad g = \Phi\,, \tag{F.7}$$

$$\text{Model - 2}\qquad g = \Phi + \frac{1}{2}\,\frac{b}{H}\,K^2\,, \tag{F.8}$$

with the material parameters b and H. The evolution equations for the internal variables then read

$$\text{Model - 1} \qquad \dot{\boldsymbol{\varepsilon}}^{\text{pl}} = \lambda_{\text{pm}} \frac{\partial \Phi}{\partial \boldsymbol{\sigma}} , \qquad \dot{\alpha} = \lambda_{\text{pm}} \frac{\partial \Phi}{\partial K} = \lambda_{\text{pm}} , \tag{F.9}$$

$$\text{Model - 2} \qquad \dot{\boldsymbol{\varepsilon}}^{\text{pl}} = \lambda_{\text{pm}} \frac{\partial g}{\partial \boldsymbol{\sigma}} = \lambda_{\text{pm}} \frac{\partial \Phi}{\partial \boldsymbol{\sigma}} , \qquad \dot{\alpha} = \lambda_{\text{pm}} \frac{\partial g}{\partial K} = \lambda_{\text{pm}} \left[1 - b\, \alpha \right] . \tag{F.10}$$

With these equations at hand, the dissipation of each model can be written as

$$\begin{aligned} \text{Model - 1} \quad \mathcal{D}^{\text{mech}} &= \boldsymbol{\sigma} : \dot{\boldsymbol{\varepsilon}}^{\text{pl}} + K\, \dot{\alpha} = \lambda_{\text{pm}} \left[\boldsymbol{\sigma} : \frac{\partial \Phi}{\partial \boldsymbol{\sigma}} + K \right] \\ &= \lambda_{\text{pm}} \left[\| \boldsymbol{\sigma}^{\text{dev}} \| + K \right] , \end{aligned} \tag{F.11}$$

$$\begin{aligned} \text{Model - 2} \quad \mathcal{D}^{\text{mech}} &= \boldsymbol{\sigma} : \dot{\boldsymbol{\varepsilon}}^{\text{pl}} + K\, \dot{\alpha} = \lambda_{\text{pm}} \left[\boldsymbol{\sigma} : \frac{\partial \Phi}{\partial \boldsymbol{\sigma}} + K + b\, H\, \alpha^2 \right] \\ &= \lambda_{\text{pm}} \left[\| \boldsymbol{\sigma}^{\text{dev}} \| + K + b\, H\, \alpha^2 \right] . \end{aligned} \tag{F.12}$$

In the case of elasticity, λ_{pm} vanishes and no energy is dissipated. For plastic loading, however, $\Phi = 0$ must hold. Hence, Equations (F.5) and (F.6) respectively can be used to further transform the expression for the dissipated energy to yield

$$\text{Model - 1} \qquad \mathcal{D}^{\text{mech}} = \lambda_{\text{pm}}\, \sigma_{y_0} , \tag{F.13}$$

$$\text{Model - 2} \qquad \mathcal{D}^{\text{mech}} = \lambda_{\text{pm}} \left[\sigma_{y_0} + b\, H\, \alpha^2 \right] . \tag{F.14}$$

These expressions, however, can only be compared if the evolution of λ_{pm} and $\boldsymbol{\varepsilon}^{\text{pl}}$ is known. In order to reach an analytical solution, the following assumptions are made which are in line with the boundary value problems examined in this thesis. Consider a body with a one-dimensional stress state which is subjected to a linear increasing strain load, i.e.

$$\boldsymbol{\varepsilon} = \boldsymbol{\varepsilon}^{\text{el}} + \boldsymbol{\varepsilon}^{\text{pl}} \qquad \text{with} \qquad \varepsilon_{22} = \varepsilon_{33} \qquad \text{and} \qquad \varepsilon_{11} = c\, t . \tag{F.15}$$

For this special case and for isotropic elastic properties, the strain in lateral and the stress in loading direction can be computed by using

$$\sigma_{11} = \left[2\mu + \lambda \right] \varepsilon_{11}^{\text{el}} + 2\lambda\, \varepsilon_{22}^{\text{el}} \tag{F.16}$$

$$\sigma_{22} = \lambda\, \varepsilon_{11}^{\text{el}} + 2 \left[\mu + \lambda \right] \varepsilon_{22}^{\text{el}} = 0 \tag{F.17}$$

$$\Rightarrow \quad \varepsilon_{22}^{\text{el}} = - \frac{\lambda}{2 \left[\mu + \lambda \right]} \varepsilon_{11}^{\text{el}} = - \nu\, \varepsilon_{11}^{\text{el}} \tag{F.18}$$

$$\Rightarrow \quad \sigma_{11} = \left[\left[2\mu + \lambda \right] - \frac{\lambda^2}{\mu + \lambda} \right] \varepsilon_{11}^{\text{el}} = A\, \varepsilon_{11}^{\text{el}} = A \left[\varepsilon_{11} - \varepsilon_{11}^{\text{pl}} \right] . \tag{F.19}$$

The elastic material parameters are summarised in parameter A for the sake of more clarity. Due to the assumptions made, there is only one unknown, $\varepsilon_{11}^{\text{pl}}$. To compute the missing plastic strain component, the yield surface of each model is considered for a plastic state and the resulting equation solved for the sought unknown. Before doing so, however, the equivalent stress as well as the internal hardening variable must be defined as functions of $\varepsilon_{11}^{\text{pl}}$.

Since a one-dimensional stress state is postulated, the equivalent stress is reduced to

$$\sigma^{\text{eq}} = \sqrt{\frac{2}{3}}\,\sigma_{11} = \sqrt{\frac{2}{3}}\,A\,\left[\varepsilon_{11} - \varepsilon_{11}^{\text{pl}}\right] \tag{F.20}$$

and can be inserted into the yield surface

$$\text{Model - 1} \qquad \varPhi = \sqrt{\frac{2}{3}}\,A\,\left[\varepsilon_{11} - \varepsilon_{11}^{\text{pl}}\right] - \sigma_{y_0} - \left[\sigma_{y_\infty} - \sigma_{y_0}\right]\left[1 - \exp(-H_{\exp}\,\alpha)\right] \tag{F.21}$$

$$\text{Model - 2} \qquad \varPhi = \sqrt{\frac{2}{3}}\,A\,\left[\varepsilon_{11} - \varepsilon_{11}^{\text{pl}}\right] - \sigma_{y_0} - H\,\alpha\,. \tag{F.22}$$

Concerning the internal hardening variable, the evolution equations can be used to define the desired relation. For the specific load case at hand, the evolution of the plastic strains can be specified as

$$\text{Model - 1} \quad \dot{\boldsymbol{\varepsilon}}^{\text{pl}} = \lambda_{\text{pm}}\,\frac{\partial \varPhi}{\partial \boldsymbol{\sigma}} = \lambda_{\text{pm}} \begin{bmatrix} \sqrt{\frac{2}{3}} & 0 & 0 \\ 0 & -\frac{1}{\sqrt{6}} & 0 \\ 0 & 0 & -\frac{1}{\sqrt{6}} \end{bmatrix}, \quad \Rightarrow \quad \dot{\varepsilon}_{11}^{\text{pl}} = \lambda_{\text{pm}}\sqrt{\frac{2}{3}}\,, \tag{F.23}$$

$$\text{Model - 2} \quad \dot{\boldsymbol{\varepsilon}}^{\text{pl}} = \lambda_{\text{pm}}\,\frac{\partial g}{\partial \boldsymbol{\sigma}} = \lambda_{\text{pm}} \begin{bmatrix} \sqrt{\frac{2}{3}} & 0 & 0 \\ 0 & -\frac{1}{\sqrt{6}} & 0 \\ 0 & 0 & -\frac{1}{\sqrt{6}} \end{bmatrix}, \quad \Rightarrow \quad \dot{\varepsilon}_{11}^{\text{pl}} = \lambda_{\text{pm}}\sqrt{\frac{2}{3}}\,. \tag{F.24}$$

Applying Equations (F.9), (F.23) and (F.10), (F.24) respectively allows the integration of each equation by using a separation of variables

$$\text{Model - 1} \qquad \frac{\mathrm{d}\alpha}{\mathrm{d}t} = \lambda_{\text{pm}} \qquad \Leftrightarrow \qquad \alpha = \int \lambda_{\text{pm}}\,\mathrm{d}t\,, \tag{F.25}$$

$$\text{Model - 2} \qquad \frac{\mathrm{d}\alpha}{\mathrm{d}t} = \lambda_{\text{pm}}\,\left[1 - b\,\alpha\right] \qquad \Leftrightarrow \qquad -\frac{1}{b}\,\ln\left(1 - b\,\alpha\right) = \int \lambda_{\text{pm}}\,\mathrm{d}t\,, \tag{F.26}$$

$$\text{Model - 1} \qquad \frac{\mathrm{d}\varepsilon_{11}^{\text{pl}}}{\mathrm{d}t} = \lambda_{\text{pm}}\sqrt{\frac{2}{3}} \qquad \Leftrightarrow \qquad \sqrt{\frac{3}{2}}\,\varepsilon_{11}^{\text{pl}} = \int \lambda_{\text{pm}}\,\mathrm{d}t \tag{F.27}$$

$$\text{Model - 2} \qquad \frac{\mathrm{d}\varepsilon_{11}^{\text{pl}}}{\mathrm{d}t} = \lambda_{\text{pm}}\sqrt{\frac{2}{3}} \qquad \Leftrightarrow \qquad \sqrt{\frac{3}{2}}\,\varepsilon_{11}^{\text{pl}} = \int \lambda_{\text{pm}}\,\mathrm{d}t\,. \tag{F.28}$$

Based on Equations (F.25), (F.27) and (F.26), (F.28) the following relations are obtained

$$\text{Model - 1} \qquad \alpha = \sqrt{\frac{3}{2}}\,\varepsilon_{11}^{\text{pl}}\,, \tag{F.29}$$

$$\text{Model - 2} \qquad -\frac{1}{b}\,\ln\left(1 - b\,\alpha\right) = \sqrt{\frac{3}{2}}\,\varepsilon_{11}^{\text{pl}} \qquad \Leftrightarrow \qquad \alpha = \frac{1}{b}\left[1 - \exp\left(-b\sqrt{\frac{3}{2}}\,\varepsilon_{11}^{\text{pl}}\right)\right]. \tag{F.30}$$

This equation can now be used to finally define the yield function with $\varepsilon_{11}^{\mathrm{pl}}$ as the only unknown

$$\begin{aligned}
\text{Model - 1} \quad \varPhi &= \sqrt{\frac{2}{3}}\,A\,\left[\varepsilon_{11} - \varepsilon_{11}^{\mathrm{pl}}\right] - \sigma_{y0} - \left[\sigma_{y\infty} - \sigma_{y0}\right]\left[1 - \exp\left(-H_{\mathrm{exp}}\sqrt{\frac{3}{2}}\,\varepsilon_{11}^{\mathrm{pl}}\right)\right] && \text{(F.31)}\\
&= \sqrt{\frac{2}{3}}\,A\,\left[\varepsilon_{11} - \varepsilon_{11}^{\mathrm{pl}}\right] - \sigma_{y\infty} + \left[\sigma_{y\infty} - \sigma_{y0}\right]\exp\left(-H_{\mathrm{exp}}\sqrt{\frac{3}{2}}\,\varepsilon_{11}^{\mathrm{pl}}\right)\,,\\
\text{Model - 2} \quad \varPhi &= \sqrt{\frac{2}{3}}\,A\,\left[\varepsilon_{11} - \varepsilon_{11}^{\mathrm{pl}}\right] - \sigma_{y0} - H\,\frac{1}{b}\left[1 - \exp\left(-b\sqrt{\frac{3}{2}}\,\varepsilon_{11}^{\mathrm{pl}}\right)\right] && \text{(F.32)}\\
&= \sqrt{\frac{2}{3}}\,A\,\left[\varepsilon_{11} - \varepsilon_{11}^{\mathrm{pl}}\right] - \sigma_{y0} - \frac{H}{b} + \frac{H}{b}\exp\left(-b\sqrt{\frac{3}{2}}\,\varepsilon_{11}^{\mathrm{pl}}\right)\,.
\end{aligned}$$

In the case of plastic loading $\varPhi = 0$ must hold and allows the computation of $\varepsilon_{11}^{\mathrm{pl}}$. It is, however, not necessary to further specify $\varepsilon_{11}^{\mathrm{pl}}$, since the yield surfaces are identical if the material parameters of the model fulfil the relations

$$\begin{aligned}
b &= H_{\mathrm{exp}} && \text{(F.33)}\\
\frac{H}{b} &= \left[\sigma_{y\infty} - \sigma_{y0}\right]\,. && \text{(F.34)}
\end{aligned}$$

Since the conditional equations $\varPhi$ are identical, the resulting quantities $\varepsilon_{11}^{\mathrm{pl}}$ must also be identical. It has hence been shown that the two models do indeed yield the same stress-strain response, at least for the specific load case assumed for this derivation. Equations (F.23) and (F.24) furthermore show that the plastic multiplier of both models evolves identically and, in consequence, that the dissipation predicted by each model and shown in Equations (F.13) and (F.14) is different.

G Influence of Hill parameters on flow surface under uniaxial stress states

---

The correlation between the parameters of a Hill-type yield surface for a one-dimensional stress state is addressed in this chapter. It was already mentioned in Section 4.2 that four out of the six Hill parameters have no influence on the yield limit for a one-dimensional stress state, and that all other material parameters governing plasticity are simply scaled by one of the two remaining Hill parameters, so that infinitely many combinations of material parameters describe the same uniaxial yielding behaviour. The exact scaling relations for all material parameters are derived by comparing two formulations of the considered yield surface. Furthermore, it is shown that the evolution of plasticity is also identical for the aforementioned parameter relations.

Consider two yield surfaces $\mathit{\Phi}$ and $\tilde{\mathit{\Phi}}$, for the uniaxial stress state shown in Equation (4.30), i.e.

$$\begin{aligned}\mathit{\Phi}_0 = \left[\sqrt{H}\right] \Bigg[\left[\frac{F}{H} + 1\right]^{\frac{1}{2}} [M_{22}] - \Bigg[\frac{M_{y_0}}{\sqrt{H}} + \frac{H_{\mathrm{lin}}}{H}\, \sqrt{H}\,\alpha \\ + \left[\frac{M_{y_\infty}}{\sqrt{H}} - \frac{M_{y_0}}{\sqrt{H}}\right] \left[1 - \exp\!\left(-\frac{H_{\mathrm{exp}}}{\sqrt{H}}\, \sqrt{H}\,\alpha\right)\right]\Bigg]\Bigg],\end{aligned} \tag{G.1}$$

$$\begin{aligned}\tilde{\mathit{\Phi}}_0 = \left[\sqrt{\tilde{H}}\right] \Bigg[\left[\frac{\tilde{F}}{\tilde{H}} + 1\right]^{\frac{1}{2}} [M_{22}] - \Bigg[\frac{\tilde{M}_{y_0}}{\sqrt{\tilde{H}}} + \frac{\tilde{H}_{\mathrm{lin}}}{\tilde{H}}\, \sqrt{\tilde{H}}\,\tilde{\alpha} \\ + \left[\frac{\tilde{M}_{y_\infty}}{\sqrt{\tilde{H}}} - \frac{\tilde{M}_{y_0}}{\sqrt{\tilde{H}}}\right] \left[1 - \exp\!\left(-\frac{\tilde{H}_{\mathrm{exp}}}{\sqrt{\tilde{H}}}\, \sqrt{\tilde{H}}\,\tilde{\alpha}\right)\right]\Bigg]\Bigg].\end{aligned} \tag{G.2}$$

Furthermore, assume a prescribed, fixed stress $M_{22} = \bar{M}$ which leads to plastic yielding. For such a case, $\varPhi_0 = \tilde{\varPhi}_0 = 0$ must hold so that each equation can be transformed to

$$\begin{aligned} &\left[\frac{F}{H} + 1\right]^{\frac{1}{2}} \bar{M} - \left[\frac{M_{y0}}{\sqrt{H}} + \frac{H_{\text{lin}}}{H}\,\sqrt{H}\,\alpha \right.\\ &\left. + \left[\frac{M_{y\infty}}{\sqrt{H}} - \frac{M_{y0}}{\sqrt{H}}\right]\left[1 - \exp\!\left(-\frac{H_{\text{exp}}}{\sqrt{H}}\,\sqrt{H}\,\alpha\right)\right]\right] = 0\,, \end{aligned} \tag{G.3}$$

$$\begin{aligned} &\left[\frac{\tilde{F}}{\tilde{H}} + 1\right]^{\frac{1}{2}} \bar{M} - \left[\frac{\tilde{M}_{y0}}{\sqrt{\tilde{H}}} + \frac{\tilde{H}_{\text{lin}}}{\tilde{H}}\,\sqrt{\tilde{H}}\,\tilde{\alpha} + \right.\\ &\left.\left[\frac{\tilde{M}_{y\infty}}{\sqrt{\tilde{H}}} - \frac{\tilde{M}_{y0}}{\sqrt{\tilde{H}}}\right]\left[1 - \exp\!\left(-\frac{\tilde{H}_{\text{exp}}}{\sqrt{\tilde{H}}}\,\sqrt{\tilde{H}}\,\tilde{\alpha}\right)\right]\right] = 0\,. \end{aligned} \tag{G.4}$$

If a parameter set is chosen for each formulation, for which the relations

$$\frac{F}{H} = \frac{\tilde{F}}{\tilde{H}}\,, \tag{G.5}$$

$$\frac{M_{y0}}{\sqrt{H}} = \frac{\tilde{M}_{y0}}{\sqrt{\tilde{H}}}\,, \tag{G.6}$$

$$\frac{H_{\text{lin}}}{H} = \frac{\tilde{H}_{\text{lin}}}{\tilde{H}}\,, \tag{G.7}$$

$$\frac{M_{y\infty}}{\sqrt{H}} = \frac{\tilde{M}_{y\infty}}{\sqrt{\tilde{H}}}\,, \tag{G.8}$$

$$\frac{H_{\text{exp}}}{\sqrt{H}} = \frac{\tilde{H}_{\text{exp}}}{\sqrt{\tilde{H}}} \tag{G.9}$$

hold, the two yield surfaces are not only identical, but a relation for the internal hardening variables

$$\sqrt{H}\,\alpha = \sqrt{\tilde{H}}\,\tilde{\alpha} \tag{G.10}$$

can directly be computed. To prove that the evolution of plasticity, represented by the plastic velocity gradients

$$\boldsymbol{L}^{\text{pl}} = \lambda_{\text{pm}}\,\frac{\partial \varPhi}{\partial \boldsymbol{M}} \quad \text{and} \quad \tilde{\boldsymbol{L}}^{\text{pl}} = \tilde{\lambda}_{\text{pm}}\,\frac{\partial \tilde{\varPhi}}{\partial \boldsymbol{M}} \tag{G.11}$$

is identical for both yield surfaces, a relation between the plastic multipliers λ_{pm} and $\tilde{\lambda}_{\mathrm{pm}}$ is required. Fortunately, this relation can be found by considering the time derivative of Equation (G.10) and the associated evolution equation for the internal hardening variable, i.e.

$$\begin{aligned} \sqrt{H}\,\dot{\alpha} &= \sqrt{\tilde{H}}\,\dot{\tilde{\alpha}}\,, \\ \Leftrightarrow \quad \sqrt{H}\,\lambda_{\mathrm{pm}}\,\frac{\partial \Phi}{\partial \bar{K}} &= \sqrt{\tilde{H}}\,\tilde{\lambda}_{\mathrm{pm}}\,\frac{\partial \tilde{\Phi}}{\partial \bar{K}}\,, \qquad \text{(G.12)} \\ \Leftrightarrow \quad \sqrt{H}\,\lambda_{\mathrm{pm}} &= \sqrt{\tilde{H}}\,\tilde{\lambda}_{\mathrm{pm}}\,, \\ \Rightarrow \quad \lambda_{\mathrm{pm}} &= \frac{\sqrt{\tilde{H}}}{\sqrt{H}}\,\tilde{\lambda}_{\mathrm{pm}}\,. \qquad \text{(G.13)} \end{aligned}$$

With Equations G.5 (adding one, expanding fraction, using inversion) and G.12 at hand, it can be shown that

$$\begin{aligned} \boldsymbol{L}^{\mathrm{pl}} = \lambda_{\mathrm{pm}}\,\frac{\partial \Phi}{\partial \boldsymbol{M}} &= \frac{\lambda_{\mathrm{pm}}}{\sqrt{F+H}} \begin{bmatrix} -F & 0 & 0 \\ 0 & F+H & 0 \\ 0 & 0 & -H \end{bmatrix} \\ &= \lambda_{\mathrm{pm}}\,\sqrt{F+H} \begin{bmatrix} -\frac{F}{F+H} & 0 & 0 \\ 0 & 1 & 0 \\ 0 & 0 & -\frac{H}{F+H} \end{bmatrix} \\ &= \lambda_{\mathrm{pm}}\,\sqrt{H}\,\sqrt{1+\frac{F}{H}} \begin{bmatrix} -\frac{F}{F+H} & 0 & 0 \\ 0 & 1 & 0 \\ 0 & 0 & -\frac{H}{F+H} \end{bmatrix} \qquad \text{(G.14)} \\ &= \tilde{\lambda}_{\mathrm{pm}}\,\sqrt{\tilde{H}}\,\sqrt{1+\frac{\tilde{F}}{\tilde{H}}} \begin{bmatrix} -\frac{\tilde{F}}{\tilde{F}+\tilde{H}} & 0 & 0 \\ 0 & 1 & 0 \\ 0 & 0 & -\frac{\tilde{H}}{\tilde{F}+\tilde{H}} \end{bmatrix} = \tilde{\lambda}_{\mathrm{pm}}\,\frac{\partial \tilde{\Phi}}{\partial \boldsymbol{M}} = \tilde{\boldsymbol{L}}^{\mathrm{pl}} \end{aligned}$$

holds. Hence, an infinite number of material parameter combinations can describe the same uniaxial plastic behaviour for this material model, such that the form of yield surface and the rate of plastic hardening are identical.

Bibliography

[1] *DIN 1319-1:1995-01, Grundlagen der Meßtechnik, Teil 1: Grundbegriffe.* Beuth-Verlag, Berlin, 1995.

[2] W. P. Adamczyk, T. Kruczek, G. Moskal, and R. A. Białecki. Nondestructive technique of measuring heat conductivity of thermal barrier coatings. *International Journal of Heat and Mass Transfer*, 111:442–450, 2017.

[3] S. Avril, M. Bonnet, A.-S. Bretelle, M. Grédiac, F. Hild, P. Ienny, F. Latourte, D. Lemosse, S. Pagano, E. Pagnacco, et al. Overview of identification methods of mechanical parameters based on full-field measurements. *Experimental Mechanics*, 48(4):381–402, 2008.

[4] M. Bambach, S. Heppner, D. Steinmetz, and F. Roters. Assessing and ensuring parameter identifiability for a physically-based strain hardening model for twinning-induced plasticity. *Mechanics of Materials*, 84:127–139, 2015.

[5] D. Banabic. *Sheet Metal Forming Processes, Constitutive Modelling and Simulation.* Springer, 2010.

[6] A. Bartels, T. Bartel, M. Canadija, and J. Mosler. On the thermomechanical coupling in dissipative materials: a variational approach for generalized standard materials. *Journal of the Mechanics and Physics of Solids*, 82:218–234, 2015.

[7] J. V. Beck and K. J. Arnold. *Parameter estimation in engineering and science.* Wiley, 1977.

[8] J. Beck and A. Osman. Nonlinear inverse problem for the estimation of time-and-space-dependent heat-transfer coefficients. *Journal of Thermophysics and Heat Transfer*, 3(2): 146–152, 1989.

[9] E. Berkovich, A. Golubeva, E. Shadek, and L. Tukh. Use of methods of solving inverse problems of heat conduction to establish the coefficient of heat transfer in jet cooling. *Journal of Engineering Physics*, 34(5):619–624, 1978.

[10] F. Bernhard. *Handbuch der technischen Temperaturmessung.* Springer-Verlag, 2014.

[11] R. Berthelsen, D. Tomath, R. Denzer, and A. Menzel. Finite element simulation of coating-induced heat transfer: application to thermal spraying processes. *Meccanica*, 51(2):291–307, 2016.

[12] M. Box. A new method of constrained optimization and a comparison with other methods. *The Computer Journal*, 8(1):42–52, 1965.

[13] S. Brandt. *Datenanalyse für Naturwissenschaftler und Ingenieure: Mit statistischen Methoden und Java-Programmen.* Springer-Verlag, 2013.

[14] R. Brun, P. Reichert, and H. R. Künsch. Practical identifiability analysis of large environmental simulation models. *Water Resources Research*, 37(4):1015–1030, 2001.

[15] S. Chantasiriwan. Inverse determination of steady-state heat transfer coefficient. *International Communications in Heat and Mass Transfer*, 27(8):1155–1164, 2000.

[16] Y. Chemisky, F. Meraghni, N. Bourgeois, S. Cornell, R. Echchorfi, and E. Patoor. Analysis of the deformation paths and thermomechanical parameter identification of a shape memory alloy using digital image correlation over heterogeneous tests. *International Journal of Mechanical Sciences*, 96:13–24, 2015.

[17] A. Chrysochoos. Thermomechanical analysis of the cyclic behavior of materials. *Procedia IUTAM*, 4:15–26, 2012.

[18] A. Chrysochoos and H. Louche. An infrared image processing to analyse the calorific effects accompanying strain localisation. *International Journal of Engineering Science*, 38 (16):1759–1788, 2000.

[19] F. Chunli, S. Fengrui, and Y. Li. A numerical method on inverse determination of heat transfer coefficient based on thermographic temperature measurement. *Chinese Journal of Chemical Engineering*, 16(6):901–908, 2008.

[20] P. Du, G. Wang, Z. Nie, and Y. Rong. A FEM-based inverse calculation method for determination of heat transfer coefficient in liquid quenching process. In *TMS 2014: 143rd Annual Meeting & Exhibition*, pages 309–315. Springer, 2014.

[21] M. Ekh. Thermo-elastic-viscoplastic modeling of IN792. *Journal of the Mechanical Behavior of Materials*, 12(6):359–388, 2001.

[22] W. S. Farren and G. I. Taylor. The heat developed during plastic extension of metals. *Proceedings of the Royal Society of London. Series A, Containing Papers of a Mathematical and Physical Character*, 107(743):422–451, 1925.

[23] L. Fiala, M. Jerman, P. Reiterman, and R. Černý. Determination of thermal conductivity of silicate matrix for applications in effective media theory. *International Journal of Thermophysics*, 39(2):28, 2018.

[24] A. Fossum. Parameter estimation for an internal variable model using nonlinear optimization and analytical/numerical response sensitivities. *Journal of Engineering Materials and Technology*, pages 337–345, 1997.

[25] A. Freddi, G. Olmi, and L. Cristofolini. *Experimental Stress Analysis for Materials and Structures: Stress Analysis Models for Developing Design Methodologies*, volume 4 of *Springer Series in Solid and Structural Mechanics*. Springer, 2015.

[26] S. Hartmann and R. R. Gilbert. Identifiability of material parameters in solid mechanics. *Archive of Applied Mechanics*, 88(1-2):3–26, 2018.

[27] S. Hartmann, R. R. Gilbert, A. K. Marghzar, C. Leistner, and P. K. Dileep. Material parameter identification of unidirectional fiber-reinforced composites. *Archive of Applied Mechanics*, 91(2):687–712, 2021.

[28] J. Hodowany, G. Ravichandran, A. Rosakis, and P. Rosakis. Partition of plastic work into heat and stored energy in metals. *Experimental Mechanics*, 40(2):113–123, 2000.

[29] A. G. Holzapfel. *Nonlinear Solid Mechanics: A Continuum Approach for Engineering.* John Wiley & Sons, Inc., 2000.

[30] F. P. Incropera, A. S. Lavine, T. L. Bergman, and D. P. DeWitt. *Fundamentals of Heat and Mass Transfer.* Wiley, 2007.

[31] Iron Boar Labs Ltd. Makeitfrom, 2018-09-20. URL `https://www.makeitfrom.com`.

[32] S. G. Johnson. *The NLopt nonlinear-optimization package*, 2014. URL `http://ab-initio.mit.edu/nlopt`.

[33] J. Kajberg and G. Lindkvist. Characterisation of materials subjected to large strains by inverse modelling based on in-plane displacement fields. *International Journal of Solids and Structures*, 41(13):3439–3459, 2004.

[34] B. Kleuter. *Generalized Parameter Identification for Finite Viscoelasticity.* PhD thesis, Technische Universität Kaiserslautern, 2007.

[35] B. Kleuter, A. Menzel, and P. Steinmann. Generalized parameter identification for finite viscoelasticity. *Computer Methods in Applied Mechanics and Engineering*, 196(35-36): 3315–3334, 2007.

[36] P. Knysh and Y. P. Korkolis. Determination of the fraction of plastic work converted into heat in metals. *Mechanics of Materials*, 86:71–80, 2015.

[37] R. Kreißig, U. Benedix, and U.-J. Görke. Statistical aspects of the identification of material parameters for elasto-plastic models. *Archive of Applied Mechanics*, 71(2):123–134, 2001.

[38] T. Kruczek, W. P. Adamczyk, and R. A. Bialecki. In situ measurement of thermal diffusivity in anisotropic media. *International Journal of Thermophysics*, 34(3):467–485, 2013.

[39] D. Lecompte, A. Smits, H. Sol, J. Vantomme, and D. Van Hemelrijck. Mixed numerical–experimental technique for orthotropic parameter identification using biaxial tensile tests on cruciform specimens. *International Journal of Solids and Structures*, 44(5):1643–1656, 2007.

[40] I.-S. Liu. *Continuum Mechanics.* Springer Science & Business Media, 2013.

[41] H. Louche, P. Schlosser, D. Favier, and L. Orgéas. Heat source processing for localized deformation with non-constant thermal conductivity. Application to superelastic tensile tests of NiTi shape memory alloys. *Experimental Mechanics*, 52(9):1313–1328, 2012.

[42] D. Macdougall. Determination of the plastic work converted to heat using radiometry. *Experimental Mechanics*, 40(3):298–306, 2000.

[43] R. Mahnken. Theoretische und numerische Aspekte zur Modellierung und Parameteridentifikation bei metallischen Werkstoffen. *Universität Hannover, Habilitation*, 1996.

[44] R. Mahnken. An inverse finite-element algorithm for parameter identification of thermoelastic damage models. *International Journal for Numerical Methods in Engineering*, 48 (7):1015–1036, 2000.

[45] R. Mahnken and E. Kuhl. Parameter identification of gradient enhanced damage models with the finite element method. *European Journal of Mechanics-A/Solids*, 18(5):819–835,

1999.

[46] R. Mahnken and E. Stein. Parameter identification for finite deformation elasto-plasticity in principal directions. *Computer Methods in Applied Mechanics and Engineering*, 147 (1-2):17–39, 1997.

[47] R. Mahnken, M. Johansson, and K. Runesson. Parameter estimation for a viscoplastic damage model using a gradient-based optimization algorithm. *Engineering Computations*, 15(7):925–955, 1998.

[48] E. Markiewicz, B. Langrand, and D. Notta-Cuvier. A review of characterisation and parameters identification of materials constitutive and damage models: from normalised direct approach to most advanced inverse problem resolution. *International Journal of Impact Engineering*, 110:371–381, 2017.

[49] J. Mason, A. Rosakis, and G. Ravichandran. On the strain and strain rate dependence of the fraction of plastic work converted to heat: an experimental study using high speed infrared detectors and the Kolsky bar. *Mechanics of Materials*, 17(2-3):135–145, 1994.

[50] F. Meraghni, Y. Chemisky, B. Piotrowski, R. Echchorfi, N. Bourgeois, and E. Patoor. Parameter identification of a thermodynamic model for superelastic shape memory alloys using analytical calculation of the sensitivity matrix. *European Journal of Mechanics-A/Solids*, 45:226–237, 2014.

[51] M. Meuwissen, C. Oomens, F. Baaijens, R. Petterson, and J. Janssen. Determination of the elasto-plastic properties of aluminium using a mixed numerical–experimental method. *Journal of Materials Processing Technology*, 75(1-3):204–211, 1998.

[52] J. A. Nelder and R. Mead. A simplex method for function minimization. *The Computer Journal*, 7(4):308–313, 1965.

[53] M. A. M. Page and S. Hartmann. Experimental characterization, material modeling, identification and finite element simulation of the thermo-mechanical behavior of a zinc die-casting alloy. *International Journal of Plasticity*, 101:74–105, 2018.

[54] H. Parisch. *Festkörper-Kontinuumsmechanik: Von den Grundgleichungen zur Lösung mit Finiten Elementen.* Vieweg+Teubner, 2003.

[55] W. Parker, R. Jenkins, C. Butler, and G. Abbott. Flash Method of Determining Thermal Diffusivity, Heat Capacity, and Thermal Conductivity. *Journal of Applied Physics*, 32(9): 1679–1684, 1961.

[56] T. Pottier, F. Toussaint, H. Louche, and P. Vacher. Inelastic heat fraction estimation from two successive mechanical and thermal analyses and full-field measurements. *European Journal of Mechanics-A/Solids*, 38:1–11, 2013.

[57] A. Rieger. *Zur Parameteridentifikation komplexer Materialmodelle auf der Basis realer und virtueller Testdaten.* PhD thesis, Dissertation, Bericht Nr.: I-14, University of Stuttgart, 2005.

[58] M. Ristinmaa, M. Wallin, and N. S. Ottosen. Thermodynamic format and heat generation of isotropic hardening plasticity. *Acta Mechanica*, 194(1-4):103–121, 2007.

[59] D. Rittel. On the conversion of plastic work to heat during high strain rate deformation of glassy polymers. *Mechanics of Materials*, 31(2):131–139, 1999.

[60] P. Rosakis, A. Rosakis, G. Ravichandran, and J. Hodowany. A thermodynamic internal variable model for the partition of plastic work into heat and stored energy in metals. *Journal of the Mechanics and Physics of Solids*, 48(3):581–607, 2000.

[61] L. Rose and A. Menzel. Identification of thermal material parameters for thermo-mechanically coupled material models. *Meccanica*, 56(2):393–416, 2021.

[62] L. Rose and A. Menzel. Optimisation based material parameter identification using full field displacement and temperature measurements. *Mechanics of Materials*, 145:103292, 2020. Erratum - 151 (2020), 103630.

[63] A. Saai, H. Louche, L. Tabourot, and H. Chang. Experimental and numerical study of the thermo-mechanical behavior of Al bi-crystal in tension using full field measurements and micromechanical modeling. *Mechanics of Materials*, 42(3):275–292, 2010.

[64] G. Scheday. *Theorie und Numerik der Parameteridentifikation von Materialmodellen der finiten Elastizität und Inelastizität auf Grundlage optischer Feldmessmethoden*. PhD thesis, Dissertation, Bericht Nr.: I-11, Institut für Mechanik (Bauwesen), Lehrstuhl I, University of Stuttgart, 2003.

[65] P. Schlosser. *Influence of thermal and mechanical aspects on deformation behaviour of NiTi alloys*. PhD thesis, Grenoble University, 2008.

[66] S. Schmaltz and K. Willner. Comparison of different biaxial tests for the inverse identification of sheet steel material parameters. *Strain*, 50(5):389–403, 2014.

[67] M. Schneider. *Datenanalyse für Naturwissenschaftler, Mediziner und Ingenieure*. Springer, 2020.

[68] H. Seibert, T. Scheffer, and S. Diebels. Biaxial testing of elastomers–experimental setup, measurement and experimental optimisation of specimen's shape. *Technische Mechanik*, 34(2):72–89, 2014.

[69] P. Senseny and A. Fossum. On testing requirements for viscoplastic constitutive parameter estimation. *Journal of Engineering Materials and Technology*, 117(2):151–156, 1995.

[70] L. Sprave and A. Menzel. A large strain gradient-enhanced ductile damage model: finite element formulation, experiment and parameter identification. *Acta Mechanica*, 231(12): 5159–5192, 2020.

[71] L. Stainier and M. Ortiz. Study and validation of a variational theory of thermo-mechanical coupling in finite visco-plasticity. *International Journal of Solids and Structures*, 47(5):705–715, 2010.

[72] G. W. Stewart. Collinearity and least squares regression. *Statistical Science*, 2(1):68–84, 1987.

[73] G. I. Taylor and H. Quinney. The latent energy remaining in a metal after cold working. *Proceedings of the Royal Society of London. Series A, Containing Papers of a Mathematical and Physical Character*, 143(849):307–326, 1934.

[74] D. Winter. *Optische Verschiebungsmessung nach dem Objektrasterprinzip mit Hilfe eines flächenorientierten Ansatzes.* PhD thesis, University of Braunschweig, 1993.

[75] Q. Yang, L. Stainier, and M. Ortiz. A variational formulation of the coupled thermo-mechanical boundary-value problem for general dissipative solids. *Journal of the Mechanics and Physics of Solids*, 54(2):401–424, 2006.

[76] S. Zhang, L. Leotoing, D. Guines, and S. Thuillier. Potential of the cross biaxial test for anisotropy characterization based on heterogeneous strain field. *Experimental Mechanics*, 55(5):817–835, 2015.

Publication series of the Institute of Mechanics

published to date:

2010/01 Palnau, V.: Implementierung eines netzfreien Diskretisierungsverfahrens und seine Anwendung auf die Scherbandanalyse.
ISBN 978-3-921823-51-4

2010/02 Klusemann, B.: Application of homogenization methods and crystal plasticity to the modeling of heterogeneous materials of technological interest.
ISBN 978-3-921823-53-8

2011/01 Hortig, C.: Local and non-local thermomechanical modeling and finite-element simulation of high-speed cutting.
ISBN 978-3-921823-54-5

2011/02 Parvizian, F.: Modeling of microstructure evolution in aluminum alloys during hot extrusion.
ISBN 978-3-921823-56-9

2011/03 Noman, M.: Characterization and model identification for the simulation of the forming behavior of ferritic steels.
ISBN: 978-3-921823-55-2

2011/04 Kayser, T.: Characterization of microstructure in aluminum alloys based on electron backscatter diffraction.
ISBN: 978-3-921823-57-6

2011/05 Bargmann, S.: Computational modeling of material behavior on different scales based on continuum mechanics.
ISBN: 978-3-921823-58-3

2013/01 Waffenschmidt, T.: Modelling and simulation of adaptation and degradation in anisotropic biological tissues.
ISBN: 978-3-921823-61-3

2015/01 Ostwald, R.: Modelling and simulation of phase-transformations in elastoplastic polycrystals.
ISBN: 978-3-921823-66-8

2016/01	Subramanian, M.: Phenomenological modelling and simulation of ferroelectric ceramics. ISBN: 978-3-921823-74-3
2016/02	Clausmeyer, T.: Evolution of plastic anisotropy in metals. ISBN: 978-3-921823-76-7
2017/01	Holtermann, R.: Computational multiscale modelling of grinding processes. ISBN: 978-3-921823-86-6
2017/02	Bartels, A.: Modelling of evolving microstructures at different scales. ISBN: 978-3-921823-93-4
2017/03	Dusthakar Kumar Rao, D. K.: Computational modelling of single and polycrystalline ferroelectric materials. ISBN 978-3-921823-94-1
2019/01	Buckmann, K.: Microstructure evolution in functional magnetic materials. ISBN 978-3-947323-09-8
2019/02	Kaiser, T.: Computational modelling of non-simple and anisotropic materials. ISBN 978-3-947323-14-2
2019/03	Heitbreder, T.: Modelling of material interfaces at different length scales. ISBN 978-3-947323-18-0
2020/01	Berthelsen, R.: Computational homogenisation of thermomechanical problems. ISBN 978-3-947323-19-7
2020/02	Sievers, C.: Describing the macroscopic behavior of surfaces based on atomistic models. ISBN 978-3-947323-24-1
2022/01	Rose, L.: Optimisation based parameter identification using optical field measurements. ISBN 978-3-947323-31-9